Faculty of Engineering, Science and Mathematics
School of Engineering Sciences

Computer simulation studies of magnetic nanostructures

A thesis submitted in partial satisfaction
of the requirements for the degree of
Doctor of Philosophy

Richard P. Boardman

Computational Engineering and Design Group
School of Engineering Sciences
University of Southampton
United Kingdom

Supervisors: Dr. Hans Fangohr, Prof. Simon J. Cox

17th May 2005

UNIVERSITY OF SOUTHAMPTON

ABSTRACT

FACULTY OF ENGINEERING, SCIENCE AND MATHEMATICS
SCHOOL OF ENGINEERING SCIENCES

Doctor of Philosophy

COMPUTER SIMULATION STUDIES OF MAGNETIC NANOSTRUCTURES

Richard Paul Boardman

Scientific and economic interest has recently turned to smaller and smaller magnetic structures which can be used in hard disk drives, magnetoresistive random access memory (MRAM), and other novel devices. For nanomagnets the geometric shape of the object becomes more important than other factors such as magnetocrystalline anisotropy — the smaller the object, the more strongly the shape anisotropy affects the hysteresis loop.

We investigate the micromagnetic behaviour of ferromagnetic samples of various geometries using numerical methods. Finite differences and finite elements are used to solve the Landau-Lifshitz-Gilbert and Brown's equations in three dimensions. Simulations of basic geometric primitives such as cylinders and spheres of sub-micron size orders provide hysteresis loops of the average magnetisation, and additionally our computations allow the study of the microscopic configuration of the magnetisation. We show different mechanisms of vortex penetration for these geometries, and investigate part-spherical geometries whose magnetisation pattern demonstrates qualities of other primitives.

Developing this further, we calculate the hysteresis loops for a *droplet* shape — a part-sphere capped with an half-ellipsoid. This resembles the shapes formed by some chemical self-assembly methods, a low-cost and efficient way of creating a commercially viable product. When examining the magnetic microstructure of this geometry we find different types of vortex behaviour, and reveal the dependence of this on the physical characteristics of the droplet.

We also examine the hysteresis loops and magnetic structures of other geometries formed through the self-assembly method such as antidots — honeycomb-like arrays of spherical holes in a thin film. We show magnetisation patterns and comparison between experimental and computed magnetic force microscopy (MFM) measurements.

Contents

List of Tables

List of Figures

Declaration of Authorship

I, Richard Paul Boardman, declare that the thesis entitled *Computer simulation studies of magnetic nanostructures* and the work presented in it are my own. I confirm that:

- this work was done wholly or mainly while in candidature for a research degree at the University;
- where any part of this thesis has previously been submitted for a degree or any other qualification at this University or any other institution, this has been clearly stated;
- where I have consulted the published work of others, this is always clearly attributed;
- where I have quoted from the work of others, the source is always given. With the exception of such quotations, this thesis is entirely my own work;
- I have acknowledged all main sources of help;
- where the thesis is based on work done by myself jointly with others, I have made clear exactly what was done by others and what I have contributed myself;
- parts of this work have been published as:
    - Micromagnetic simulation of ferromagnetic part-spherical particles *Journal of Applied Physics*, 95(11), pp. 7037-7039, June 2004 (with H. Fangohr, A. V. Goncharov, A. A. Zhukov, P. A. J. de Groot and S. J. Cox)
    - Micromagnetic simulation studies of ferromagnetic part-spheres *Journal of Applied Physics*, 97(10), June 2005 (with J. Zimmermann, H. Fangohr, A. A. Zhukov and P. A. J. de Groot; also published in the *Virtual Journal of Nanoscale Science and Technology*, May 2005)
    - Self-assembly routes towards creating superconducting and magnetic arrays *Journal of Low Temperature Physics* 139(1/2), pp. 339-349, April 2005 (with A. A. Zhukov, E. T. Filby, A. V. Goncharov, M. A. Ghanem, P. N. Bartlett, H. Fangohr, V. V. Metlushko, V. Novosad, G. Karapetrov and P. A. J. de Groot)
    - Oscillatory thickness dependence of the coercive field in 3D anti-dot arrays from self-assembly *Journal of Applied Physics*, accepted, August 2004 (with A. A. Zhukov, A. V. Goncharov, P. A. J. de Groot, M. A. Ghanem, I. S. El-Hallag, P. N. Bartlett, H. Fangohr, V. Novosad and G. Karapetrov)

- Oscillatory thickness dependence of the coercive field in magnetic 3D anti-dot arrays *Physical Review Letters, preprint at cond-mat/0406091*, submitted June 2004 (with A. A. Zhukov, M. A. Ghanem, A. V. Goncharov, V. Novosad, G. Karapetrov, H. Fangohr, P. N. Bartlett and P. A. J. de Groot)
- Micromagnetic modelling of ferromagnetic cones *Physical Review B*, submitted July 2005 (with H. Fangohr, M. J. Fairman, J. Zimmermann, S. J. Cox, A. A. Zhukov and P. A. J. de Groot)

Signed: ____

Date: ___________________

Acknowledgements

The author would like to acknowledge helpful discussions with Michael Donahue of the Math, Statistics and Computational Science department within the National Institute of Standards and Technology, to whom I am indebted for affording much assistance with the finer points of the *Object Oriented Micromagnetic Framework*.

Many fruitful conversations with Werner Scholz of Seagate Technologies, Inc. yielded further insight into the workings of *magpar*, for which I am most grateful.

I have had many indispensable meetings, e-mail and telephone conversations with Alexander Zhukov, Alexander Goncharov and Peter de Groot of the School of Physics and Astronomy at the University of Southampton, providing plots of experimental data and guidance with theory — I am much obliged to you all.

My colleagues Jürgen Zimmermann and Giuliano Bordignon deserve many thanks for their industrious verification of the equations and derivations found in both the body of this thesis and the appendices.

My supervisor Hans Fangohr has provided thorough and dependable first-class supervision and assistance where necessary and I am extraordinarily appreciative of this.

I would like to thank my family for their tireless proof-reading of this work and their devoted support, and to them I dedicate this thesis.

最后，我也向我的妻子，丽丽，深表感谢。没有他的爱护与协助，我是无法完成这篇论文的。

Trademarks and copyright information

AMD, *Opteron* and *Athlon* are trademarks of Advanced Micro Devices

RenderMan® and *Pixar* are registered trademarks of Pixar Animation Studios

The *Visualization Toolkit* (VTK) is copyright © 1993-2002 Ken Martin, Will Schroeder, Bill Lorensen

IBM is a trademark of International Business Machines

Intel, *Pentium 4* and *Xeon* are trademarks of Intel Corp.

Philips is a registered trademark of Koninklijke Philips Electronics N.V.

Hitachi is a trademark of Hitachi Global Storage Technologies

Toshiba is a trademark of Toshiba Corporation.

Linux is a trademark of Linus Torvalds

The left-hand side of figure 1.3 is © 2004 Griff Wason. `http://www.griffwason.com`

Nomenclature

α	The Landau and Lifshitz phenomenological damping parameter, see equation (2.36)
$\boldsymbol{\mu}$	A magnetic moment, see equation (2.1)
λ_{ex}	The exchange length of a material in metres (m); computed as a function of A and M. See equation , see equation (2.40)
$\mathbb{J}$	The set of indices for magnetic moments $\boldsymbol{\mu}_i$ that are located inside the volume $V(\mathbf{r}, \Delta r)$, see equation (2.17)
$\mathcal{E}$	The total energy in a system, see equation (2.15)
$\mathcal{E}_{\mathrm{ex}}^{i,j}$	The exchange energy between two neighbouring magnetic moments $\boldsymbol{\mu}_i$ and $\boldsymbol{\mu}_j$, see equation (2.2)
$\mathcal{E}_{\mathrm{an}}$	The anisotropy energy of a system, see equation (2.27)
$\mathcal{E}_{\mathrm{cub}}^{i}$	The cubic anisotropy energy of a magnetic moment $\boldsymbol{\mu}_i$, see equation (2.8)
$\mathcal{E}_{\mathrm{di}}$	The dipolar energy of a system, see equation (2.29)
$\mathcal{E}_{\mathrm{di}}^{i,j}$	The dipolar energy between two magnetic moments $\boldsymbol{\mu}_i$ and $\boldsymbol{\mu}_j$, see equation (2.12)
$\mathcal{E}_{\mathrm{uni}}^{i}$	The uniaxial anisotropy energy of a magnetic moment $\boldsymbol{\mu}_i$, see equation (2.6)
$\mathcal{E}_{\mathrm{Ze}}$	The Zeeman energy of a system, see equation (2.28)
$\mathcal{E}_{\mathrm{Ze}}^{i}$	The Zeeman energy of a magnetic moment $\boldsymbol{\mu}_i$, see equation (2.10)
$\mathcal{J}$	The exchange integral, originating from the wave function for two electrons $\Psi(\mathbf{r}_1, \mathbf{r}_2)$ being antisymmetric, see equation (2.2)
$\mathcal{N}$	Used to represent nearest neighbours in summations, see equation (2.4)
μ_0	The magnetic constant, $4\pi \cdot 10^{-7}\ \mathrm{T} \cdot \mathrm{m} \cdot \mathrm{A}^{-1}$, see equation (2.40)
μ_B	The Bohr magneton, 9.2741×10^{-24} A·m^2, see equation (2.1)
$\mathbf{H}$	The externally-applied magnetic field, see equation (2.10)
$\mathbf{H}_{\mathrm{de}}$	The demagnetising field in a system, see equation (2.30)
$\mathbf{H}_{\mathrm{eff}}$	The effective magnetic field, a function of the total energy $\mathcal{E}$, see equation (2.36)
$\mathbf{L}$	The orbital momentum, see equation (2.1)
$\mathbf{M}$	Magnetisation, see equation (2.36)

$\mathbf{M}(\mathbf{r})$	The locally averaged density of magnetic moments assumed to be a continuous and differentiable function, see equation (2.16)
$\mathbf{n}$	In magnetostatics, the vector normal to the surface of a sample, see equation (2.30)
$\mathbf{P}$	The positional vector for lattice geometries, see equation (6.5)
$\mathbf{r}_{ij}$	The distance between two magnetic moments $\boldsymbol{\mu}_i$ and $\boldsymbol{\mu}_j$ at positions $\mathbf{r}_i$ and $\mathbf{r}_j$, see equation (2.13)
$\mathbf{S}$	The electron spin, see equation (2.1)
A	The exchange coupling constant, see equation (2.25)
a	The distance between nearest neighbours in a crystalline lattice, see equation (2.25)
B_c	The coercive field *i.e.* the applied field where the overall magnetisation of a sample is zero ($B_c = \mu_0 H_c$)
d	The diameter of the circular or spherical part of a magnetic sample, usually measured across the xy plane
g	The generalised Landé factor, $\approx$2, see equation (2.1)
h	In geometry, the height of an object, usually measured along the z axis, see equation (3.0)
H_c	The coercive field *i.e.* the applied field where the overall magnetisation of a sample is zero
K_1	The primary anisotropy constant of a material procured through experiment measurements, expressed as a temperature-dependent energy density, see equation (2.6)
K_2	The secondary anisotropy constant of a material procured through experimental measurements, expressed as a temperature-dependent energy density, see equation (2.6)
$l_{z(e)}$	The physical size of the z component of an ellipsoid in a constructive solid geometry, see equation (5.2)
$l_{z(s)}$	The physical size of the z component of a sphere in a constructive solid geometry, see equation (5.1)
M_r	The remanent magnetisation *i.e.* the magnitude of the magnetisation of a sample when the applied magnetic field is zero
M_s	The saturation point *i.e.* the magnitude of the maximum possible magnetisation of a sample
r	In geometry, the radius of the circular or spherical part of a sample, usually measured across the xy plane
z	The cell site number; $z = 1$, 2 or 4 for simple cubic, body-centred cubic and face-centred cubic respectively, see equation (2.25)

Chapter 1

Introduction

1.1 Historical context

Lodestone, rich in the mineral magnetite (Fe_3O_4), was known for its qualities of attraction thousands of years ago. Historical accounts vary, but they indicate that ancient Egyptian, Greek and Central American civilisations were familiar with it. The Chinese first used a compass as a fortune-telling device and subsequently as a directional indicator somewhere between 400 B.C. and 100 B.C., but surprisingly it was not until later in the first millennium A.D. that a needle compass was used for navigation.

In the thirteenth century Petri Pergrinus (Pierre de Maricourt) outlined the direction to which the needle would point at various positions around a lodestone, and from this ascertained that magnets had two regions, north and south.

The Elizabethan scientist William Gilbert demonstrated that the Earth was a giant magnet (*Gilbert and Mottelay*, 1600, 1991) and that this was responsible for the directional alignment of a compass needle, additionally observing that the attractive effects of amber were, contrary to general belief at that juncture, *not* magnetic: we now know this is a form of electrical attraction. Gilbert prepared and presented Queen Elizabeth I of England with a magnetite model to demonstrate the magnetic behaviour of the Earth (figure 1.1) called a *terrella*, or “little earth”. When the terrella was aligned with the poles of the Earth it would spin on its axis.

Gilbert is also responsible for providing the *north-south* polar analogy between magnets and the Earth’s poles, and disposing of most of the magical legends surrounding magnetism, though he did develop the somewhat esoteric notion that the Earth had an *anima*, or “soul” which was the source of the magnetic field. The anima was effective up to the *orbis virtutis*: the “orb of virtue”.

Gilbert can be credited with establishing magnetism as a scientific field. His work fascinated Galileo Galilei who, influenced by Gilbert’s work (*BBC*, 2004), hypothesised that the Earth orbited the Sun rather than the popular perception of the time which was that the Sun (and everything else) revolved around the Earth.

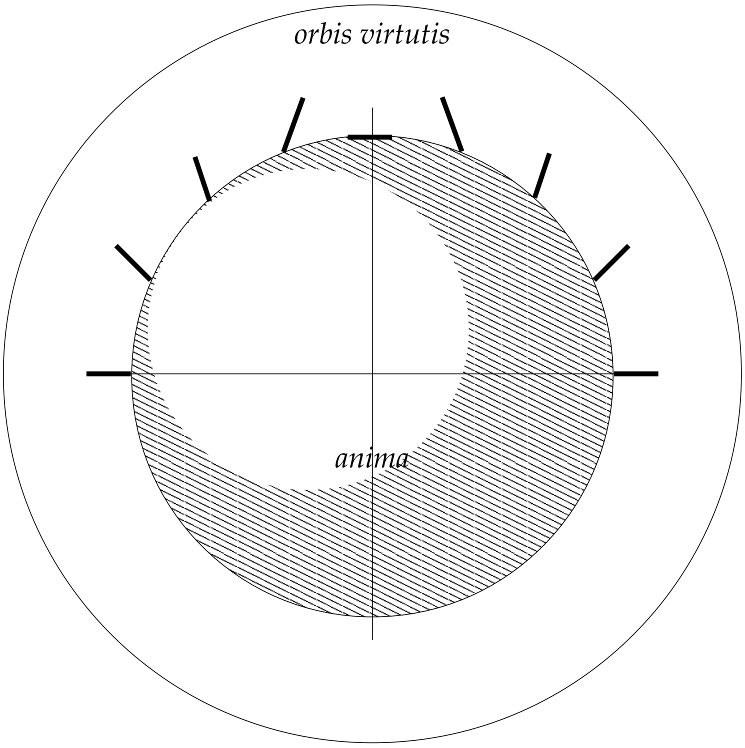

Figure 1.1: William Gilbert's magnetic model of the Earth

In the mid-eighteenth century John Michell proposed that the attractive force between two magnets can be calculated using the inverse square law, *i.e.* that if the two entities are half as far apart, the force between them will be four times greater. Charles Augustin de Coulomb verified this experimentally and indicated that if one were to split a magnet then two new poles would be created (figure 1.2, left).

A professor at the University of Copenhagen, Hans Christian Oersted, observed during a demonstration that the needle of a compass was deflected whenever he turned on an electric current; this was the first recorded instance of the relationship between magnetism and electricity. André Ampère, a French physicist, confirmed this and just one week after the initial observation by Oersted had developed an equation to calculate the magnetic force between electric currents.

Towards the end of the 1830s Michael Faraday propounded the concept of *lines of force*, nowadays known as magnetic field lines, as a way of visualising the magnetic field of an object (figure 1.2, right); these can be seen when dusting iron filings around a traditional bar magnet. Faraday was also responsible for creating the electric generator and motor.

During the 1850s and 1860s James Clerk Maxwell developed mathematical equations derived from mechanical models which described the electricity and magnetism, the relationship between them, and Faraday's lines of force. These equations were published in 1873 and defined classical electromagnetism.

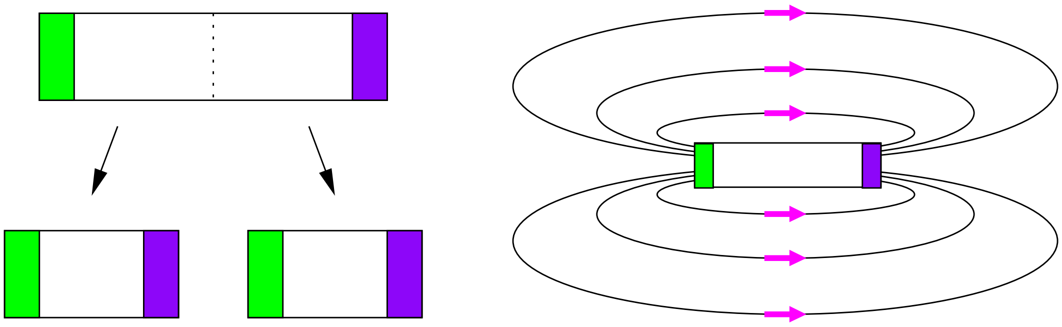

Figure 1.2: Coulomb's theory (left) was that if one were to break a magnet into two parts then two new poles would form at the broken ends. Magnetic field lines or "lines of force" (right) as demonstrated by Michael Faraday.

1.2 Modern magnetism

Augustin Jean Fresnel, best known for his work with light, mentioned in a letter to Ampère that the electric currents responsible for magnetic forces might operate at microscopic lengths.

At the start of the twentieth century another French physicist, Pierre Weiss, developed his theory of magnetism, which began to describe magnetic interactions at the microscopic scale. With the advent of quantum mechanics, magnetic interactions became better understood.

Building on these new principles, magnetic recording systems developed at the end of the nineteenth century were improved and the consequent development of magnetic tape eventually paved the way for the audio tape recorder in the middle of the twentieth century.

Today, magnets are pervasive in daily life:

- Cars contain magnets in starter motors, electric windows, door locking systems, electronic relays and alternators.
- Kitchens have magnetic motors in refrigerators, microwave ovens, washing machines and tumble dryers.
- Entertainment systems such as video recorders, CD and DVD players, audio tape recorders and minidisc players all contain motors. These motors contain magnets.
- Televisions and monitors use magnets to deflect and position the electron beam used to create an image, as well as high-voltage electromagnets to *degauss* the tube. Degaussing eliminates apparent colouring problems with the display tubes in these devices.
- Electric bells in telephones, alarms and doorbells contain magnetic ringers.

- Medical applications include the use of magnetic fluids in eye surgery and drug delivery, as guides in keyhole surgery, prosthetics, cancer therapy and magnetic resonance imaging.

Magnets can also be found on the reverse side of credit cards, in cooling fans, power station generators and audio speakers. One of the fastest-developing areas in magnetism is in the area of data storage in computers, particularly hard disk drives.

1.3 Hard disk drives

Magnetic systems have been used in recent years for the long-term storage of data in computers. The first hard disk came in 1956 from IBM inside their RAMAC (Random Access Method of Accounting and Control) computer, capable of storing 100,000 characters on each of fifty 24-inch disk platters and constructed from iron oxide and aluminium. These disks had a data, or areal, density of around 2 kilobits per square inch.

Seventeen years later IBM released the Winchester hard disk, containing the basic technologies used in modern hard disk drives: a very small read/write head capable of "skiing" around 1/18,000,000 of an inch above the surface of the disk. The Winchester had an areal density of 1.7 megabits per square inch.

Seagate Storage Technology developed the first hard disk for personal computers in 1980. Although this disk had a similar capacity to the RAMAC, the entire assembly fit into a 5.25 inch enclosure (form factor): the same width and double the height of a standard modern CD-ROM drive. Three years later, Rodime introduced a hard disk in a 3.5 inch form factor, and in 1985 Quantum attached this to a hard card which plugged directly into a personal computer's system board.

This form factor evolution continued throughout the late 1980s, until standard 3.5 inch hard drives with integrated electronics appeared. Introduced by Conner in 1988, these had the same physical dimensions as a standard desktop PC hard disk drive today. The same year saw the first 2.5 inch hard drive, now the *de facto* standard for laptop computers, though the 1.8 inch form factor is gaining popularity with slimline and sub-notebook sized laptops.

Currently the smallest hard disk drive with this configuration is the Hitachi Microdrive (figure 1.3), having a one inch form factor and a height of just five millimetres but with a capacity of four gigabytes.

Hard disk drive manufacturers are constantly looking for ways to improve areal density, as this equates to a greater storage capacity. Areal density is widely regarded as the crucial metric driving the hard disk industry. The highest areal density today is more than fifty million times greater than in the late 1950s: the present

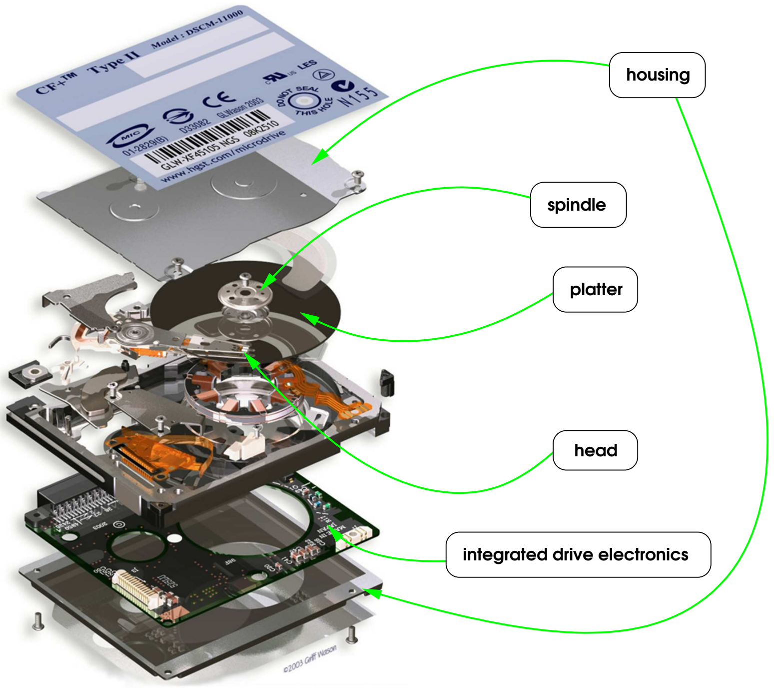

Figure 1.3: An exploded view of the Hitachi Microdrive. The disk platter and read/write head can be seen in the third layer from the top. The long edge of the disk housing is one inch (base image artwork credit: © 2004 Griff Wason).

record is held by Toshiba Corporation at 133 gigabits per square inch and areal density is presently doubling every twelve months.

This trend cannot, however, continue indefinitely. Present methods of hard disk production are approaching physical limits, and the areal density will no longer be able to increase beyond these fundamental limits. To overcome these physical limitations, we can look to the behaviour of magnets at the microscopic scales used in hard disks to find potential solutions.

1.4 Overview of relevant interactions

The direction of magnetic moments at a small scale is governed by four competing energy terms. The *dipolar* energy is the one most people are familiar with, though not necessarily by this name: this is the energy which causes magnets to align north pole to south pole. The *exchange* energy in ferromagnetic materials will attempt to make the magnetic moments in the immediately surrounding space lie parallel to one another. *Anisotropy* energy is low when the moments are aligned along a particular crystal direction, and *Zeeman* energy is smallest when the magnetic moments lie in the same direction as an external magnetic field.

Since the most efficient magnetic alignment, or *configuration*, is the one in which the energy is lowest, these four energy terms will attempt to become as small as possible at the expense of their peers: this results in very rich, complex and aesthetically attractive physics.

The competition of these interactions under different conditions is responsible for the overall behaviour of a magnetic system, and the ability to compute this yields a greater understanding of such systems.

1.5 Computer simulations

Analytical models exist for some magnetic systems, however for these models solutions are only practical for simple cases. Experiments allow observations to be made of real systems, but we are limited to the detail which can be extracted from these measurements.

When computational resources are available, more complicated models can be used which provide a link between experiment and theory. The motivation for using computer simulations is two-fold: firstly, it is possible to interpret experimental results, and secondly new designs can be predicted and subsequently developed, reducing costs.

1.6 Summary

Scientific and economic interest has recently turned to smaller and smaller magnetic structures which can be used in hard disk drives, magnetoresistive random access memory (MRAM), and other novel devices. For nanomagnets — magnets with a size order of 10^{-7} metres and below, more than five hundred times smaller than the width of a human hair — the geometric shape of the object becomes more important; the smaller the object, the more strongly the shape anisotropy affects the hysteresis loop.

This thesis reports on investigations of these magnetic nanostructures.

Chapter 2 briefly summarises the origins of magnetism, the applications of micromagnetism in modern digital data storage — specifically hard disk media and magnetoresistive random access memory — and some of the theories behind micromagnetics pertaining to our simulation work. Additionally, this chapter covers the methods we use in more detail with respect to geometry and computation, and also touches on post-simulation visualisation.

Chapter 3 investigates the properties of basic primitives. We study numerically the magnetisation reversal of a flat cylinder and a sphere, and provide studies of size dependence for these geometries.

Chapter 4 discusses the magnetic reversal behaviour of conical particles, and presents a magnetisation remanence phase diagram as a function of diameter and height.

Chapter 5 considers the simulation of “nanodots”. These tiny part-spherical geometries can be formed through a chemical self-assembly double template method, and numerical studies assist with the interpretation of experimental data.

In Chapter 6, we study the magnetic behaviour of close-packed spherical holes, or antispheres, produced through a self-assembly template method.

Finally in Chapter 7 we summarise our findings and provide an outlook for future research.

Chapter 2

Micromagnetics

2.1 Introduction

After IBM attained an areal recording density of 1Gbit/in^2 (*Tsang et al.*, 1993, 1990) — half a million times greater than RAMAC — the growth of areal density of a consumer hard disk drive has been approaching 100% every twelve months. Following current trends the next decade should witness the advent of an areal density of 1Tbit/in^2 (*Tarnopolsky*, 2004, *Wood*, 2000, *Wood et al.*, 2002).

Since modern hard disk drive technology is converging on fundamental limits (see figures 2.1, 2.2) new approaches must be considered. Micromagnetic simulation is an important method of addressing these limits. Further discussion of the applications of micromagnetic modelling can be seen in section 2.10.

In sections 2.2 to 2.6 we provide an overview of micromagnetics.

In section 2.3 we describe the different interactions and associated energies of a system of magnetic moments $\boldsymbol{\mu}$.

Section 2.4 describes the micromagnetic approach when the discrete, atomistic nature of matter is ignored and the magnetisation is represented as a continuous function of space.

In sections 2.5 and 2.6 the Landau-Lifshitz Gilbert equations and the Stoner-Wohlfarth model are introduced.

Sections 2.7 to 2.10 describe the simulation packages used in this work and associated hardware and software requirements.

Micromagnetism as a field — *i.e.* that which deals specifically with the behaviour of ferromagnetic materials at fine (1×10^{-6} metre) length scales — was introduced in 1963 when William Fuller Brown Jr. published his paper on antiparallel domain wall structure (*Brown*, 1963); however until comparatively recently computational micromagnetics — particularly when three-dimensional problems are considered — has been prohibitively expensive in terms of computational power, but now a modern desktop PC is capable of performing small micromagnetic simulations within a few days.

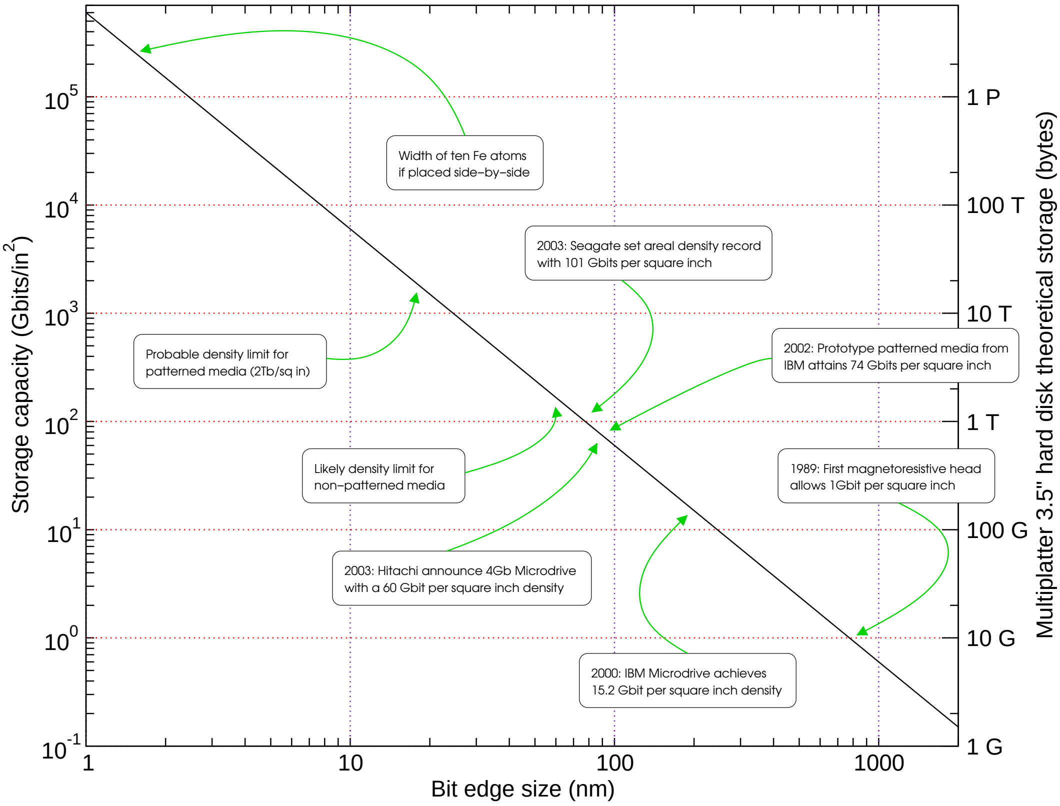

Width of ten Fe atoms if placed side–by–side

2003: Seagate set areal density record with 101 Gbits per square inch

Probable density limit for patterned media (2Tb/sq in)

2002: Prototype patterned media from IBM attains 74 Gbits per square inch

Likely density limit for non–patterned media

1989: First magnetoresistive head allows 1Gbit per square inch

2003: Hitachi announce 4Gb Microdrive with a 60 Gbit per square inch density

2000: IBM Microdrive achieves 15.2 Gbit per square inch density

Figure 2.1: As the area in which a bit can be stored decreases, the overall storage capacity increases in $\mathcal{O}(1/n^2)$ assuming a square bit of edge length n; the scale on the right indicates the capacity of a four-platter double-sided 3.5″ hard disk, ignoring spindle size and actuation overheads.

2.2 From quantum mechanics to micromagnetics

To clarify some of the terminology, concepts and fundamental models which are essential to computational micromagnetics, this section will briefly discuss some of these. More detailed accounts can be found in *Brown* (1963), *O'Handley* (1999), *Aharoni* (2000) and *Blundell* (2001).

The magnetic moment is derived from the angular momentum of electrons in an atom. For free atoms, this is a combination of electron spin and orbital momentum (*O'Handley*, 1999):

$$\boldsymbol{\mu} = -g\mu_B(\mathbf{L}+\mathbf{S}) \tag{2.1}$$

where $\boldsymbol{\mu}$ is the magnetic moment, g is the generalised Landé factor ($\approx$2), μ_B is the Bohr magneton (9.2741×10^{-24} A·m^2), $\mathbf{L}$ is the orbital momentum and $\mathbf{S}$ is the electron spin.

When materials are solids, the spin component $\mathbf{S}$ dominates the magnetic mo-

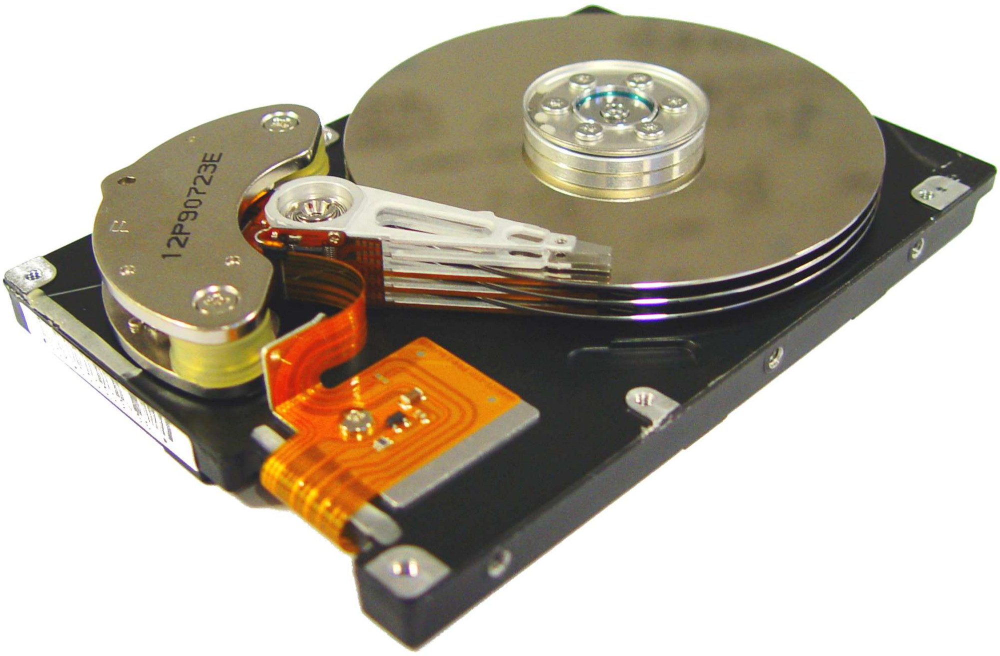

Figure 2.2: A three-platter IDE hard disk drive, manufactured by Fujitsu in 1999

name	symbol	configuration	lattice type	moment ($A\cdot m^2$)
iron	Fe	$3d^6$	bcc	2.22×10^{-23}
cobalt	Co	$3d^8$	hcp	1.72×10^{-23}
nickel	Ni	$3d^7$	fcc	0.61×10^{-23}

Table 2.1: Magnetic moments of important transition metals (*Kittel*, 1996)

ment. The magnetic moment per atom for the important 3d transition metals are shown in table 2.1.

2.3 Interactions between atomic magnetic moments

2.3.1 Exchange energy

The phenomenon whereby individual atomic magnetic moments will attempt to align all other atomic magnetic moments within a material with itself is known as the *exchange* interaction (*Aharoni*, 2000). If the magnetic moments align in a parallel fashion, the material is *ferromagnetic*; if the magnetic moments align antiparallel, the material is *antiferromagnetic*.

The exchange energy between two neighbouring magnetic moments $\boldsymbol{\mu}_i$ and $\boldsymbol{\mu}_j$ is usually described by:

name	symbol	energy between parallel neighbours (J)
iron	Fe	-1.21$\times 10^{-21}$
cobalt	Co	-5.15$\times 10^{-21}$
nickel	Ni	-4.46$\times 10^{-21}$

Table 2.2: Exchange energy between parallel ferromagnetic magnetic moments of important transition metals. Reversing the sign gives the energy between antiparallel moments

$$\mathcal{E}_{\mathrm{ex}}^{i,j} = -\mathcal{J}\mathbf{S}_i \cdot \mathbf{S}_j \tag{2.2}$$

where $\mathbf{S}$ is the unit vector of the direction of the magnetic moment:

$$\mathbf{S} = \frac{\boldsymbol{\mu}}{|\boldsymbol{\mu}|} \tag{2.3}$$

and $\mathcal{J}$ is the *exchange integral* which originates from the wave function overlap of two electrons.

Consequently, the exchange energy for a system of particles, under the assumption that the exchange energy is short-ranging and subsequently only acts on direct neighbours, is:

$$\mathcal{E}_{\mathrm{ex}} = \frac{1}{2}\sum_{i}\sum_{j\in\mathcal{N}_i}\mathcal{E}_{\mathrm{ex}}^{i,j} \tag{2.4}$$

where $\mathcal{N}_i$ represents the nearest neighbours i. The value of $\mathcal{J}$ is derived experimentally and expressed as a function of A (see equation 2.25).

The sign of $\mathcal{J}$ is important — if $\mathcal{J}$ is positive, it indicates the material exhibits ferromagnetic behaviour and the exchange energy is at a minimum when two neighbouring moments are in parallel alignment.

Antiferromagnetic materials have a negative $\mathcal{J}$, and as such have a minimum exchange energy when aligned antiparallel.

If a ferromagnet is heated above a critical point known as the *Curie* temperature (*Curie*, 1895), when the applied field is zero, the average magnetisation also becomes zero.

Typical values of exchange energy between two parallel ferromagnetic magnetic moments for iron, cobalt and nickel are given in table 2.2.

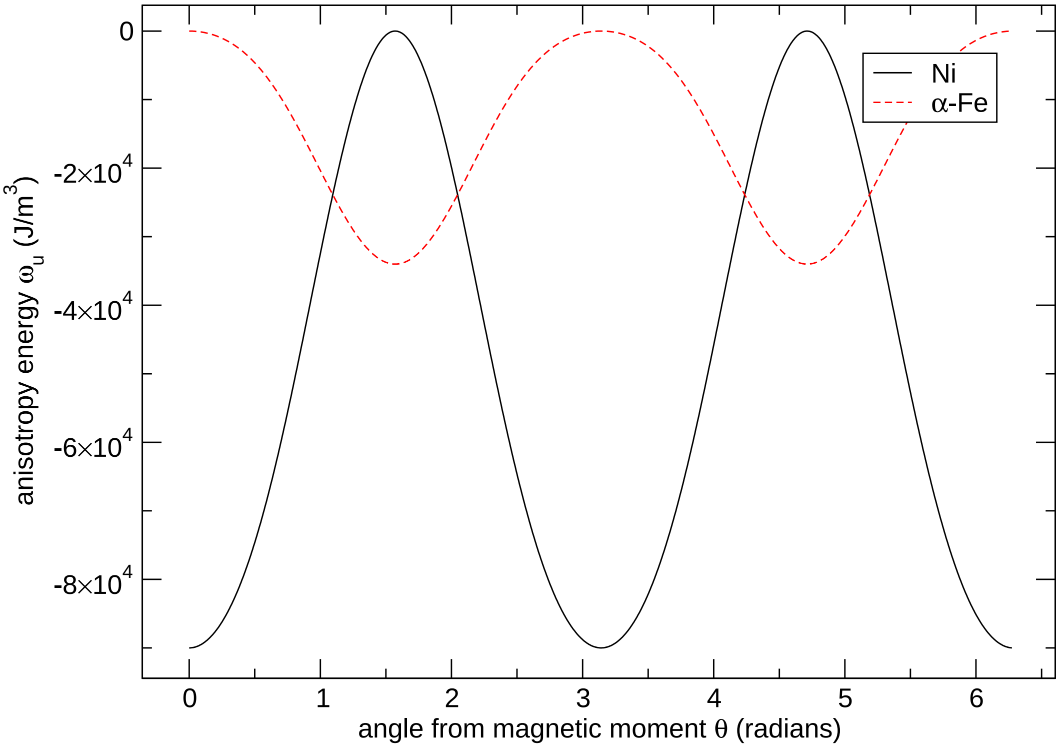

Figure 2.3: Energy density due to uniaxial anisotropy as a function of the angle θ from a magnetic moment $\boldsymbol{\mu}$. The maximum energy has been normalised to zero for clarity.

2.3.2 Anisotropy energy

Anisotropy is a dependence of energy level on some direction. If the magnetic moments in a material have a bias towards one particular direction (the easy axis) then the material is said to have uniaxial anisotropy, like cobalt. If the bias is towards many particular directions, then the material has multiple easy axes and it possesses cubic anisotropy (see figure 2.4). Cubic crystals such as iron and nickel have this property (*Aharoni*, 2000, p86). Uniaxial and cubic anisotropy are forms of magnetocrystalline anisotropy as their properties in this respect arise from the crystalline structure of the material.

The anisotropy energy in transition metal magnets arises from spin-orbit coupling. The typical fourth-order approximation of the parameterisation of uniaxial anisotropy (expressed as an energy density) is (*Aharoni*, 2000):

$$\begin{aligned} \mathcal{E}^i_{\text{uni}} &= -K_1 \cos^2(\theta_i) - K_2 \cos^4(\theta_i) && (2.5) \\ &= K_1 S_z^2 + K_2 S_z^4 && (2.6) \end{aligned}$$

where θ_i is the angle between $\mathbf{S}_i$ and the easy axis (being here the component of $\mathbf{S}$ in the direction of the crystallographic axis, z). K_1 and K_2 are temperature-dependent

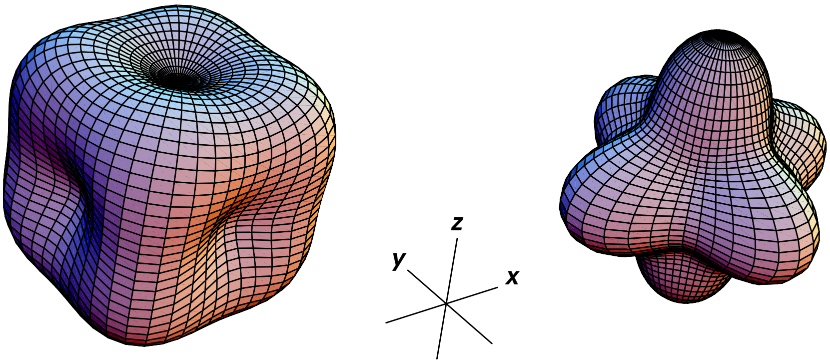

Figure 2.4: Normalised cubic anisotropy energy surfaces $w_c(\theta, \phi)$ for (left) iron and (right) nickel. The different shapes of the surfaces are a reflection of the sign of K_1 (*O'Handley*, 1999) — iron has a positive K_1, nickel a negative K_1 (see appendix C)

energy densities derived from experiment, and can exist with either a positive or negative sign. When $K_1 > 0$ the axis is easy, when $K_1 < 0$ the axis becomes hard (which yields an easy plane).

Since constant terms can be neglected, an equivalent parameterisation is:

$$\mathcal{E}^i_{\text{uni}} = K_1 \sin^2(\theta_i) + K_2 \sin^4(\theta_i) \tag{2.7}$$

The typical parameterisation of cubic anisotropy is not straightforward trigonometrically (*O'Handley*, 1999):

$$\mathcal{E}^i_{\text{cub}} = K_1(S_x^2 S_y^2 + S_y^2 S_z^2 + S_z^2 S_x^2) + K_2(S_x^2 S_y^2 S_z^2) \tag{2.8}$$

A positive sign for K_1 yields easy axes along the body edges (100). Conversely, a negative sign for K_1 indicates that the easy axes exist across the diagonals (111) (*Blundell*, 2001).

The energy for a system of magnetic moments is given by:

$$\mathcal{E}_{\text{an}} = \sum_i \mathcal{E}^i_{\text{an}} \tag{2.9}$$

where $\mathcal{E}_{\text{an}}$ is either $\mathcal{E}_{\text{uni}}$ or $\mathcal{E}_{\text{cub}}$.

It is worth noting that in some materials which are considered isotropic (*i.e.* $K_1 = K_2 = 0$) from a crystalline perspective, such as permalloy, the contribution to the total energy from the anisotropy is zero.

There are other types of anisotropy than magnetocrystalline. *Magnetostriction* is an anisotropy caused by the expansion or contraction of a ferromagnet along the direction of the magnetisation (*Aharoni*, 2000, p87). The so-called *shape* anisotropy (*Paine et al.*, 1955) (also known as "configurational stability" (*Ha et al.*, 2003)) is the direction in which the magnetisation will prefer to lie on account of the physical geometry of the sample. This becomes more and more influential the smaller one's sample becomes. This is one of the properties we investigate in this report.

2.3.3 Zeeman energy

The energy of a magnetic moment $\boldsymbol{\mu}$ in an applied magnetic field $\mathbf{H}$ is:

$$\mathcal{E}^{i}_{\mathrm{Ze}} = -\mu_0 \boldsymbol{\mu}_i \cdot \mathbf{H}_i \tag{2.10}$$

For a system of atoms:

$$\mathcal{E}_{\mathrm{Ze}} = \sum_i \mathcal{E}^{i}_{\mathrm{Ze}} \tag{2.11}$$

The Zeeman energy is at a minimum when all the magnetic moments in a sample are in alignment with the applied field.

2.3.4 Dipolar energy

Dipolar energy (often called magnetostatic or demagnetising energy) is the resultant energy from the interaction of magnetic moments with each other. Two magnetic moments at positions $\mathbf{r}_i$ and $\mathbf{r}_j$ have the dipolar energy:

$$\mathcal{E}^{i,j}_{\mathrm{di}} = \mu_0 \left(\frac{\boldsymbol{\mu}_i \cdot \boldsymbol{\mu}_j}{|\mathbf{r}_{ij}|^3} - \frac{3(\boldsymbol{\mu}_i \cdot \mathbf{r}_{ij})(\boldsymbol{\mu}_j \cdot \mathbf{r}_{ij})}{|\mathbf{r}_{ij}|^5} \right) \tag{2.12}$$

where

$$\mathbf{r}_{ij} = \mathbf{r}_j - \mathbf{r}_i \tag{2.13}$$

For N magnetic moments this becomes:

$$\mathcal{E}_{\text{di}} = \frac{1}{2}\sum_{i=1}^{N}\sum_{j\neq i}\mathcal{E}_{\text{di}}^{i,j} \tag{2.14}$$

Computing the dipolar energy is the most expensive part of any micromagnetic simulation as the dipolar energy is a long-range interaction and therefore must consider the interaction of each magnetic moment $\boldsymbol{\mu}_i$ with every other magnetic moment $\boldsymbol{\mu}_j$.

2.3.5 Total energy

Combining equations 2.4, 2.9, 2.11 and 2.14 yields the total energy:

$$\mathcal{E} = \frac{1}{2}\sum_{i}\sum_{j\in\mathcal{N}_i}\mathcal{E}_{\text{ex}}^{i,j} + \sum_{i}\mathcal{E}_{\text{an}}^{i} + \sum_{i}\mathcal{E}_{\text{Ze}}^{i} + \frac{1}{2}\sum_{i}^{N}\sum_{j\neq i}\mathcal{E}_{\text{di}}^{i,j} \tag{2.15}$$

The number of atoms in comparatively small systems is large. Assuming a cubic structure and a lattice spacing of 2.5Å as in iron, cobalt or nickel, a cube of edge length 100nm would contain 6.4×10^7 atoms.

2.4 Micromagnetic description

Since numerical computations based on the equations in section 2.3 are at an atomic level, they are historically limited to simple cases containing not too many degrees of freedom (*Aharoni*, 2000, p173). For larger problems other techniques must be used.

Brown (1963) suggested a theory which is referred to as *micromagnetic* theory. Instead of considering individual magnetic moments, a continuous magnetisation function $\mathbf{M}$ is used to approximate the atomic interaction described above. The magnetisation represents the locally averaged density of magnetic moments:

$$\mathbf{M}(\mathbf{r}) = \frac{1}{V(\mathbf{r},\Delta r)}\sum_{i\in\mathbb{J}(\mathbf{r},\Delta r)}\boldsymbol{\mu}_i \tag{2.16}$$

where $V(\mathbf{r},\Delta r)$ is a sphere of radius Δr placed at $\mathbf{r}$ and $\mathbb{J}(\mathbf{r},\Delta r)$ is the set of indices:

$$\mathbb{J} = \{i : \mathbf{r}_i \in V(\mathbf{r},\Delta r)\} \tag{2.17}$$

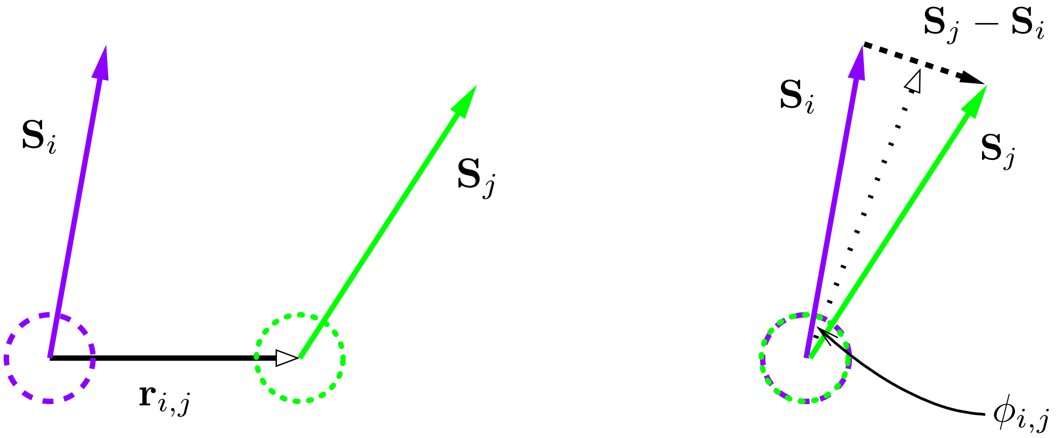

Figure 2.5: The unit vectors of two moments $\mathbf{S}_i$ and $\mathbf{S}_j$

for magnetic moments $\boldsymbol{\mu}_i$ that are located inside the volume $V(\mathbf{r}, \Delta r)$.

This averaging can be performed over the scale of the exchange length (see equation 2.40) and will always contain many magnetic moments.

$\mathbf{M}(\mathbf{r})$ is assumed to be a continuous and differentiable function which allows the expression of the interactions described above using differential operators. The resulting equations can be solved analytically (if possible) or numerically.

2.4.1 Exchange energy

Taking the atomic representation for exchange energy between two moments (equation 2.2), we can assume that the angle between two neighbouring spins is $\phi_{i,j}$. The sum of all the exchange energies based on equation 2.4 can be rewritten as:

$$\mathcal{E}_{\text{ex}} = -\mathcal{J}S^2 \sum_i \sum_{j \in \mathcal{N}_i} \cos\phi_{i,j} \tag{2.18}$$

where $S = 1$ since $\mathbf{S}$ is a unit vector (equation 2.3) and for small values of $\phi_{i,j}$ we use the leading terms in the Taylor expansion of $\cos\phi_{i,j}$ (figure 2.6):

$$\cos\phi_{i,j} \approx 1 - \frac{\phi_{i,j}^2}{2} \tag{2.19}$$

With this assumption, equation 2.18 can be rewritten:

$$\mathcal{E}_{\text{ex}} = \mathcal{K} + \frac{\mathcal{J}S^2}{2} \sum_i \sum_{j \neq i}^{\mathcal{N}} \phi_{i,j}^2 \tag{2.20}$$

where $\mathcal{K}$ is a constant. Since $\mathbf{S}_i = \frac{\mathbf{M}(\mathbf{r}_i)}{M_s}$ and $|\mathbf{S}_i| = |\mathbf{S}_j| = 1$ (figure 2.5):

$$\begin{aligned} |\phi_{i,j}| &\approx |\mathbf{S}_i - \mathbf{S}_j| && (2.21) \\ &= a\frac{|\mathbf{S}_i - \mathbf{S}_j|}{a} && (2.22) \end{aligned}$$

and $\frac{|\mathbf{S}_i - \mathbf{S}_j|}{a}$ approximates the spatial derivative of $\mathbf{S}$ over the lattice spacing a.

If we take $\mathbf{r}_{i,j}$ to be a lattice translation vector of magnitude a as in figure 2.5, the directional derivative $\nabla_{\mathbf{r}_{i,j}}\mathbf{S}$ can be used to express $|\mathbf{S}_i - \mathbf{S}_j|$.

Inserting this into equation 2.18, the exchange energy can now be represented as (*Blundell*, 2001):

$$\begin{aligned} \mathcal{E}_{\text{ex}} &= -\mathcal{J}S^2 \sum_i \sum_{j \neq i}^{\mathcal{N}} [(\mathbf{r}_{i,j} \cdot \nabla)\mathbf{S}]^2 && (2.23) \\ &= -\mathcal{J}S^2 a^2 \sum_i \sum_{j \neq i}^{\mathcal{N}} \left[(\nabla m_x)^2 + (\nabla m_y)^2 + (\nabla m_z)^2\right] && (2.24) \end{aligned}$$

if we take $\mathbf{r}_{i,j}$ outside the summations and redefine this as a (the nearest neighbour distance). Since we will integrate over volume to obtain the continuous representation, if we consider a unit cell site number $z = 1$, 2 or 4 (for simple cubic, body-centred cubic and face-centred cubic respectively), we can define the exchange coupling constant (*Aharoni*, 2000):

$$A = \frac{\mathcal{J}S^2 z}{a} \qquad (2.25)$$

We can now ignore the discrete lattice, yielding the continuous form:

$$\mathcal{E}_{\text{ex}} = A \int_V \left[(\nabla S_x)^2 + (\nabla S_y)^2 + (\nabla S_z)^2\right] \mathrm{d}^3 r \qquad (2.26)$$

2.4.2 Anisotropy energy

The continuous form of the anisotropy energy is computed by integrating the anisotropy energy w_{an} (*Aharoni*, 2000), which is in the form of either equation 2.5 or 2.8:

$$\mathcal{E}_{\text{an}} = \int_V w_{\text{an}} \mathrm{d}^3 r \qquad (2.27)$$

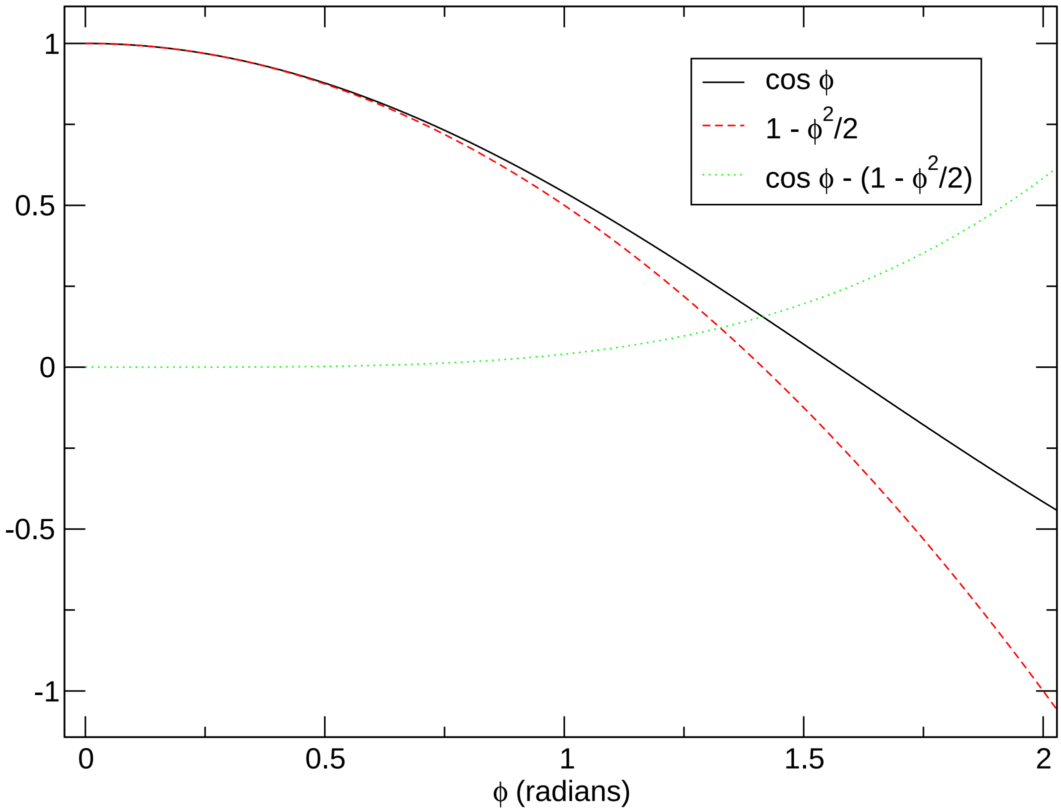

Figure 2.6: The functions $\cos\phi$ (solid black) and $1 - \frac{\phi^2}{2}$ (dashed red). The dotted green line represents the difference between the two functions

2.4.3 Zeeman energy

By ignoring the discrete lattice, equation 2.11 becomes (*Aharoni*, 2000):

$$\mathcal{E}_{\mathrm{Ze}} = -\mu_0 \int_V \mathbf{M}(\mathbf{r}) \cdot \mathbf{H}(\mathbf{r}) \mathrm{d}^3 r \tag{2.28}$$

2.4.4 Dipolar energy

The dipolar energy can be represented continuously by:

$$\mathcal{E}_{\mathrm{di}} = -\mu_0 \int_V \mathbf{H}_{\mathrm{de}}(\mathbf{r}) \cdot \mathbf{M}(\mathbf{r}) \mathrm{d}^3 r \tag{2.29}$$

where $\mathbf{H}_{\mathrm{de}}(\mathbf{r})$ is the demagnetising field with components contributed from the divergence of magnetisation within the volume and surface poles (*O'Handley*, 1999):

$$\mathbf{H}_{\mathrm{de}}(\mathbf{r}) = \frac{1}{4\pi}\left(-\int_V \mathrm{d}^3 r' \nabla \cdot \mathbf{M}(\mathbf{r}') \frac{\mathbf{r}-\mathbf{r}'}{|\mathbf{r}-\mathbf{r}'|^3} + \int_S \mathrm{d}^2 r' \mathbf{n} \cdot \mathbf{M}(\mathbf{r}') \frac{\mathbf{r}-\mathbf{r}'}{|\mathbf{r}-\mathbf{r}'|^3}\right) \tag{2.30}$$

and $\mathbf{n}$ is the surface normal.

A complete derivation of $\mathbf{H}_{\mathrm{de}}$ is given in *Brown* (1963), *Aharoni* (2000) and *Blundell* (2001).

2.5 From static to dynamic

In order to study dynamical phenomena we can combine the equations above with the work of Landau, Lifshitz and Gilbert. Taking Brown's equations for energy and the effective field $\mathbf{H}_{\mathrm{eff}}$:

$$\mathcal{E} = \mathcal{E}_{\mathrm{ex}} + \mathcal{E}_{\mathrm{an}} + \mathcal{E}_{\mathrm{Ze}} + \mathcal{E}_{\mathrm{di}} \tag{2.31}$$

$$= -\int \mu_0 \mathbf{H}_{\mathrm{eff}}(\mathbf{r}) \cdot \mathbf{M}(\mathbf{r}) \mathrm{d}^3 r \tag{2.32}$$

where

$$\mathbf{H}_{\mathrm{eff}} = -\frac{1}{\mu_0} \nabla_{\mathbf{M}} \mathcal{E} \tag{2.33}$$

then the time development of the magnetisation can be written as (*Landau and Lifshitz*, 1935):

$$\frac{\mathrm{d}\mathbf{M}(\mathbf{r})}{\mathrm{d}t} = \gamma \mathbf{M}(\mathbf{r}) \times \mathbf{H}_{\mathrm{eff}}(\mathbf{r}) - \frac{\bar{\alpha}}{M_s}\mathbf{M}(\mathbf{r}) \times (\mathbf{M}(\mathbf{r}) \times \mathbf{H}_{\mathrm{eff}}(\mathbf{r})) \tag{2.34}$$

where $\gamma \mathbf{M}(\mathbf{r}) \times \mathbf{H}_{\mathrm{eff}}(\mathbf{r})$ is representative of the precession of $\mathbf{M}(\mathbf{r})$ in a local field $\mathbf{H}_{\mathrm{eff}}(\mathbf{r})$ and $\frac{\bar{\alpha}}{M_s}\mathbf{M}(\mathbf{r}) \times (\mathbf{M}(\mathbf{r}) \times \mathbf{H}_{\mathrm{eff}}(\mathbf{r}))$ is an empirical damping term.

The damping constant $\bar{\alpha}$ is not well understood but at zero temperature it is due to spin waves quantised as magnons (*Blundell*, 2001, p122), and at finite temperature due to atomic lattice oscillations quantised as phonons.

2.6 Computational models

Equation 2.15 requires the evaluation of a number of sums. The computational effort for n magnetic moments scales as $\mathcal{O}(n^2)$ as a result of the dipolar term (see section 2.3.4).

Brown's continuum approximation postulates that the magnetisation $\mathbf{M}$ (*i.e.* the magnetic moment per unit volume) can be regarded as a continuous function of space. This allows an approximation of equation 2.15 to be expressed as a partial differential equation (equation 2.32) for which the standard mathematical techniques for solving PDEs can be used.

The following sections describe different approaches attacking this challenge. In section 2.6.1 the Stoner-Wohlfarth model is described which reduced the number of degrees of freedom to tackle the reversal of small magnetic particles.

In section 2.6.2 we show how the Landau-Lifshitz-Gilbert (LLG) equations can be used to determine the time development of the magnetisation once the effective field is determined through Brown's static equations.

Section 2.7 introduces the simulation packages used n this work which solve the equations of Brown and Landau-Lifshitz-Gilbert numerically — this is commonly referred to as computational micromagnetism.

2.6.1 The Stoner-Wohlfarth model

The Stoner-Wohlfarth model (*Stoner and Wohlfarth*, 1948) is the model of coherent rotation of magnetisation. This makes the assumption that the direction of magnetisation of all moments within the system are parallel leaving only two degrees of freedom and reducing the exchange energy factor to zero. One then only need consider the interaction with the applied field and the anisotropic energy of the system (*Aharoni*, 2000):

$$\mathcal{E} = K_1 V \sin^2(\theta - \phi) - \mu H \cos\phi \tag{2.35}$$

where K_1 is the anisotropy energy density, V is a particle volume, μ is the magnetic moment, ϕ is the direction of the magnetic moment to the *easy* axis (that is, the axis with which the magnetisation prefers to align), θ is the angle between the easy axis and the applied field.

The Stoner-Wohlfarth model is applicable to smaller systems with a comparatively large contribution to anisotropy, where one can consider all magnetic moments to be aligned. If single-domain behaviour can be expected then the Stoner-Wohlfarth model is appropriate. For larger systems the approximation breaks down as it neglects the dipolar component and consequently more complicated magnetic microstructures, such as domains and vortices, are unable to form with this model.

2.6.2 The Landau-Lifshitz-Gilbert equation

With the rapidly-increasing processing capability of modern computers, there has been a surge of interest in the field of computational micromagnetics, and indeed computer-based simulation in general. An important differential equation was derived by *Landau and Lifshitz* (1935).

The Landau-Lifshitz-Gilbert equation, briefly introduced in section 2.5, is a fundamental part of time-dependent computational micromagnetics. Different arrangements of this equation are used in calculations and simulations.The OOMMF simulation software (*Donahue and Porter*, 1999) uses the Landau and Lifshitz form:

$$\begin{aligned}\frac{\mathrm{d}\mathbf{M}(\mathbf{r},t)}{\mathrm{d}t} &= -|\bar{\gamma}|\mathbf{M}(\mathbf{r},t)\times\mathbf{H_{eff}}(\mathbf{M}(\mathbf{r},t)) \\ &\quad -\frac{|\bar{\gamma}|\alpha}{M_s}\mathbf{M}(\mathbf{r},t)\times(\mathbf{M}(\mathbf{r},t)\times\mathbf{H_{eff}}(\mathbf{M}(\mathbf{r},t)))\end{aligned} \tag{2.36}$$

which is more commonly written as

$$\frac{\mathrm{d}\mathbf{M}}{\mathrm{d}t} = -|\bar{\gamma}|\mathbf{M}\times\mathbf{H_{eff}} - \frac{|\bar{\gamma}|\alpha}{M_s}\mathbf{M}\times(\mathbf{M}\times\mathbf{H_{eff}}) \tag{2.37}$$

where $\mathbf{M}$ is the magnetisation (*i.e.* the magnetic moment per unit volume), $\mathbf{H_{eff}}$ is the effective magnetic field, α is the Landau and Lifshitz phenomenological damping parameter (where $\bar{\alpha}$ from equation 2.34 is equivalent to $|\bar{\gamma}|\alpha$) and $\bar{\gamma}$ is the Landau and Lifshitz electron gyromagnetic ratio (the ratio of the magnetic dipole moment to the mechanical angular momentum of some system). If one assumes

$$\gamma = (1+\alpha^2)\bar{\gamma} \tag{2.38}$$

then this can be shown to be mathematically equivalent to the Gilbert form (*Gilbert*, 1955)

$$\frac{\mathrm{d}\mathbf{M}}{\mathrm{d}t} = -|\gamma|\mathbf{M} \times \mathbf{H_{eff}} + \frac{\alpha}{M_s}\left(\mathbf{M} \times \frac{\mathrm{d}\mathbf{M}}{\mathrm{d}t}\right) \tag{2.39}$$

2.7 Simulation

There are two software packages underpinning the simulations performed for this work. The first is the *Object Oriented MicroMagnetic Framework*, or OOMMF (*Donahue and Porter*, 1999) provided by the National Institute of Standards and Technology. OOMMF employs the finite difference (FD) method which requires the *discretisation* (or segmentation, see section 2.7.1) of a chosen geometry over a grid of cells each of identical volume and cuboidal shape.

The second is *magpar* (*Scholz*, 2003, *Scholz et al.*, 2003a), developed by Werner Scholz and the group of Prof. Fidler and Prof. Schrefl of the Technische Universität Wien. This software uses the hybrid finite element/boundary element method (FE/BE) and as such requires that the chosen geometry be discretised with tetrahedral volume elements which can be of variable volume and shape.

The aspect of these software packages which shifts the configuration of the magnetisation on a step-wise basis is an *evolver*, based on the Landau-Lifshitz-Gilbert (LLG) differential equation (2.37).

2.7.1 Discretisation

When a particular geometry is decided upon for simulation, this must be discretised into lots of smaller cuboidal cells to be able to use the finite difference method. Each cell is considered to be homogeneously magnetised, *i.e.* within a micromagnetic simulation all of the atomic magnetic moments inside this cellular domain are thought to behave as a single particle. This is an acceptable assumption because at an atomic length scale the exchange interaction, responsible for the homogeneous alignment of magnetic moments, is overwhelmingly the most significant energy term. These smaller cells can then be used to perform the simulation. The separate simulation cells represent a certain amount of magnetic material. Obviously in this instance a finer discretisation mesh — a smaller simulation cell size — is more desirable than a coarser mesh, particularly when there are curved surfaces in the geometry.

Figure 2.7 demonstrates the effect of altering the number of cells in a geometry. In the case of extremely coarse discretisation using the finite difference method, a sphere can resemble more a cuboid than a sphere (figure 2.7, left). A poor representation of the shape in the discrete model can affect the influence of the shape anisotropy (see section 2.3.2) on the magnetisation, and subsequently negatively affect the results.

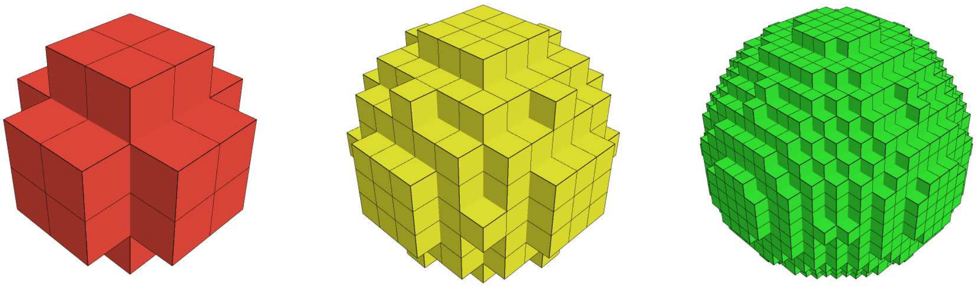

Figure 2.7: The effect of altering the number of cells in a geometry, in this instance a sphere. $4^3 = 64$ cells (left) gives poor shape resolution for the sphere. Increasing this to $9^3 = 729$ cells (centre) improves the resolution but $19^3 = 6859$ cells (right) gives a much more "spherical" representation

Figure 2.8 shows the discretisation of a sphere using both fixed size cubic cells (finite difference) and variable sized tetrahedral cells (finite element). In this sphere example, there are four times fewer cells in the finite element example yet it is aesthetically more sphere-like.

The exchange length is a length scale over which the direction of $\mathbf{M}$ does not change significantly, as across this length the exchange energy is overwhelmingly the dominant component and other influences have little effect. A coarse mesh will not allow the software to resolve the exchange length properly, so independent domains will not form correctly. The exchange length is calculated by considering (*Kronmüller and Fähnle*, 2003, *Seberino and Bertram*, 2001):

$$\lambda_{\mathrm{ex}} = \sqrt{\frac{A}{\frac{1}{2}\mu_0 M_s^2}} \tag{2.40}$$

where A is the exchange energy (measured in $\mathrm{J/m}$), μ_0 is the magnetic constant ($4\pi 10^{-7}\ \mathrm{T} \cdot \mathrm{m} \cdot \mathrm{A}^{-1}$) and M_s is the magnetisation in $\mathrm{A/m}$.

The exchange length λ_{ex} therefore gives us a quantitative measure for the required mesh resolution.

The derivation of the exchange energy in the micromagnetic theory uses the Taylor series expansion of the cosine between two moments (equation 2.19) to the second-order. It is crucial that the maximum angle between these two adjacent moments is not high (*Donahue and McMichael*, 2002) — indeed if the angle becomes larger than $\pi/2$ radians, then the results of the simulation are highly inaccurate as the torque between the two spins begins to decrease when the angle is further increased; this could potentially lead to the scenario where the angle between two adjacent spins is π radians — according to the second-order Taylor expansion of the cosine, this would be a perfectly legitimate low-energy state, although this is clearly not the case as the exchange energy and consequently the torque between these two spins in this state would be extremely large.

material	exchange energy A (J/m)	magnetisation M_s (A/m)	anisotropy K_1 (J/m^3)	exchange length λ_{ex} (nm)
nickel	9×10^{-12}	4.9×10^5	-5.7×10^3 (cubic)	7.72
iron	2.1×10^{-13}	1.70×10^6	4.8×10^4 (cubic)	3.40
cobalt	3.0×10^{-13}	1.40×10^6	5.2×10^5 (uniaxial)	4.94
supermalloy	1.05×10^{-13}	8.0×10^5	0	5.11
permalloy $\mathrm{Ni}_{50}\mathrm{Fe}_{50}$	5.85×10^{-12}	1.11×10^6	0	2.76
permalloy $\mathrm{Ni}_{80}\mathrm{Fe}_{20}$	1.30×10^{-13}	8.6×10^5	0	5.29
iron-palladium	1.5×10^{-11}	1.36×10^6	3.5×10^6 (uniaxial)	3.59
iron-platinum	1.0×10^{-11}	1.14×10^6	7.7×10^6 (uniaxial)	3.50

Table 2.3: Properties of some common ferromagnetic materials

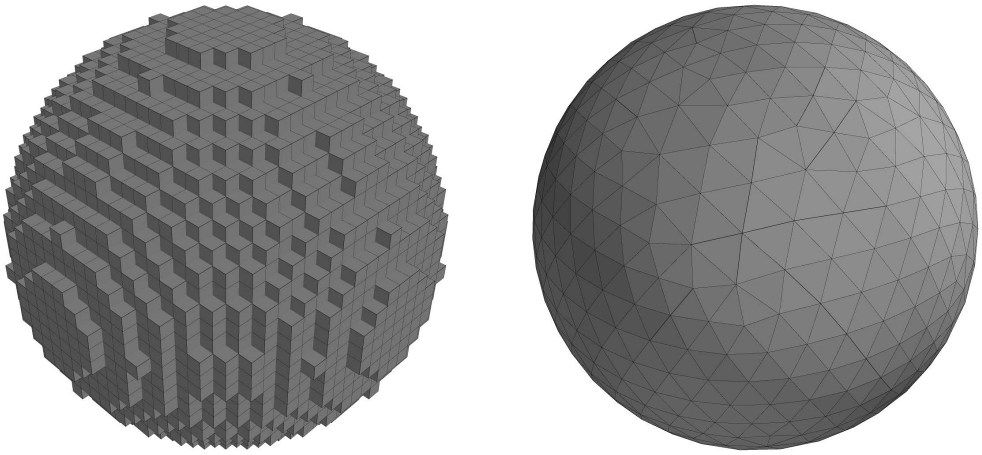

Figure 2.8: Finite difference (left) and finite element (right) meshes. For adequate shape resolution, the finite difference model requires more cells than the finite element model; in this case 27000 and 5000 respectively

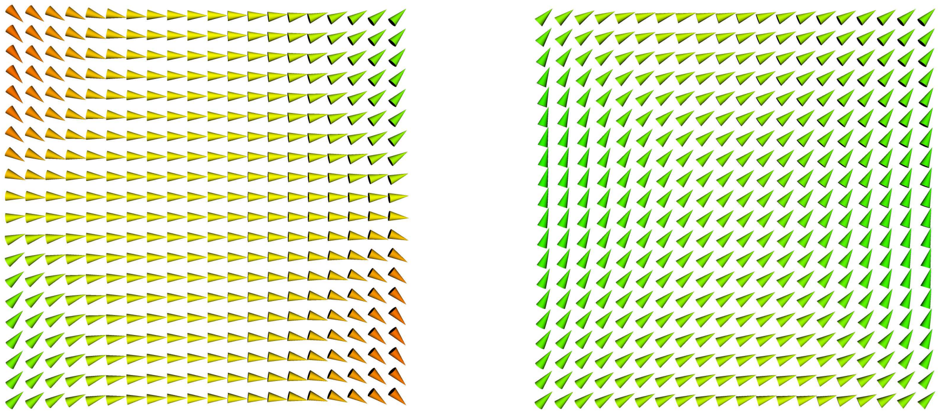

Figure 2.9: Cutplane showing the relaxed magnetisation from an edge-aligned initial state (left) and a diagonally-aligned initial state (right)

Incidentally, it is worth noting that since the simulation is not atomistic, (*i.e.* it doesn't compute the exchange energy using equation 2.2), the use of the discretised version of the micromagnetic expression for the exchange energy 2.26 is always slightly inaccurate from a quantitative perspective, however if the angle between two spins is greater than $\pi/2$ radians then the behaviour becomes qualitatively wrong.

The answer to these problems is of course to create a finer mesh; however if one makes the mesh n times as fine, then the number of the cells in the simulation increases by n^3 (since the system is three-dimensional) and this results in a massively increased computational overhead.

2.7.2 LLG relaxation

For problems where we are only interested in a static metastable magnetisation state — *i.e.* those for which we do not need to know the coercive field value or indeed need the hysteresis loop — these can be simply "relaxed". Relaxing the system involves defining some initial magnetisation configuration, usually homogeneous or random, and then allowing the system to iterate over the Landau-Lifshitz-Gilbert equation until the rate of change of magnetisation is below a certain threshold. The configuration, complete with any domains and states in which it might prefer to exist, can be observed and then the magnetic microstructure can be analysed. This should, of course, be repeated several times to verify that the remanent magnetisation states are consistent. Figure 2.9 shows the relaxation states of a 100nm × 100nm × 20nm supermalloy (79% nickel, 17% iron and 4% molybdenum) nanomagnet from our computations; virtually identical results can be seen in the paper by *Cowburn* (2000).

2.8 Micromagnetic systems

2.8.1 The hysteresis loop

The hallmark of a magnetic system is the *hysteresis loop*. This is traditionally represented graphically as the overall magnetisation of the sample against some applied magnetic field. The value of the applied field where the loop crosses zero magnetisation is known as the *coercive* field H_c or B_c, and this therefore represents the amount of applied field required to reverse the magnetisation direction of the magnet. The *remanent magnetisation* M_r is the magnetisation which remains when the applied field is reduced to zero.

Comparing the hysteresis loops, such as those in figure 2.10, of a soft and a hard magnet, one can make the observation that the softer magnet will have a narrow hysteresis loop, *i.e.* the applied field necessary to reverse the magnetisation is relatively low, and the hard magnet will possess a comparatively wide hysteresis loop.

The point at which the overall magnetisation of a sample can no longer be increased (as all the magnetisation is pointing utterly in a single direction) — the *saturation* point or M_s — is identified as a plateau at the extremes of applied field in a hysteresis loop.

Also one should note that the area underneath the hysteresis loop is equivalent to the energy which, when the field is reversed, is converted into heat.

For the long-term storage of data, it is desirable to have a material with a wide hysteresis loop, and therefore a large coercive field, as this makes it more difficult for the said material to lose its magnetisation state. A narrow hysteresis loop is a characteristic beneficial for applications such as recording heads, as in these temporary magnetisation promotes easy switching between magnetisation states. The ideal hysteresis loops for applications in magnetic media can be seen in figure 2.11.

2.8.2 Domains

Figure 2.12 shows a relatively large (*i.e.* a size order of 10^{-6} metres) ferromagnet which contains domains. Domains can be thought of as the magnetic structures which form at small scales within magnets in particular circumstances (*Hubert and Schäfer*, 1998, 2000). Within these domains the magnetisation is parallel, though the overall magnetisation of any given domain is not in a particular direction. This gives rise to a mean magnetisation of approximately zero across a sample in zero field. Figure 2.13 illustrates an example of domains formed in a sample with a simple closed flux.

At high applied fields — what defines a high field is dependent on the type, size and shape of the magnet; it must be enough to fully saturate the magnetisation

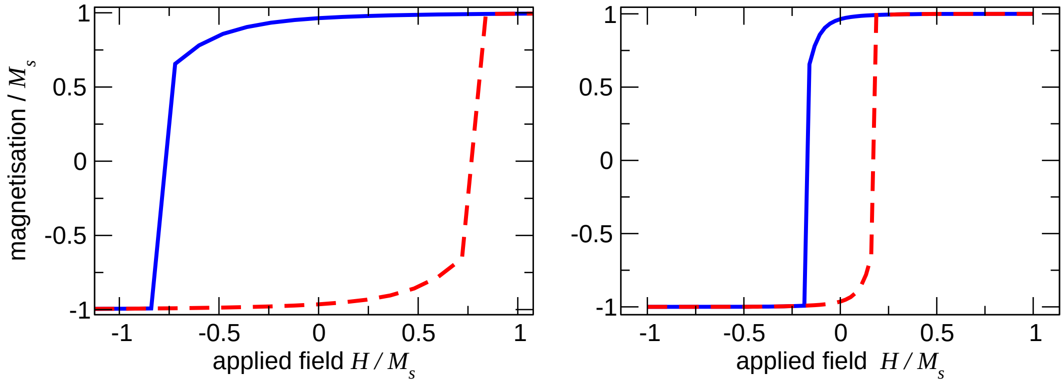

Figure 2.10: Two typical hysteresis loops — the left loop shows some permanently magnetic material, the right loop a softer magnet. The solid blue line indicates reducing field, the dashed red line indicates increasing field

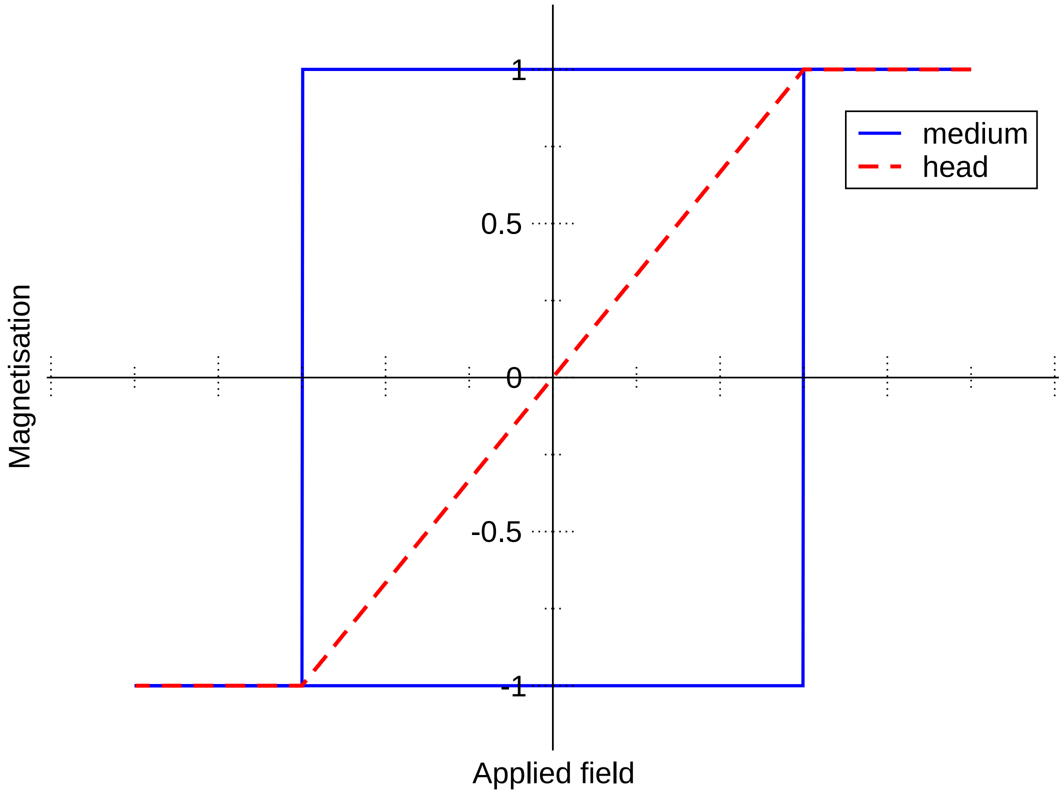

Figure 2.11: Magnetic recording ideals. A square loop with a high coercivity is good for the long-term storage of data; an infinitely narrow loop with diagonal characteristics is desirable for the field switching required of read heads in magnetic media applications

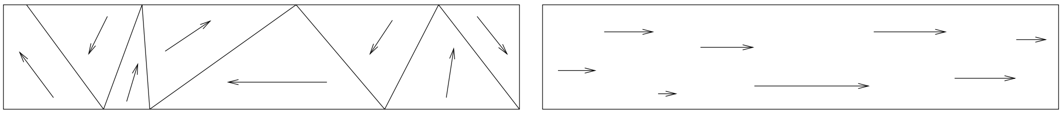

Figure 2.12: A typical ferromagnet in zero field (left) and in an applied field (right)

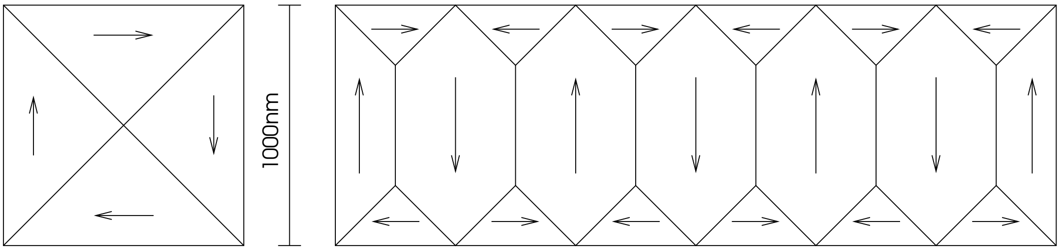

Figure 2.13: Flux closure (left), and (right) a larger sample attempting to close its flux through domains.

— no individual domains will form as the overall magnetisation in the sample is homogeneous at these fields; this can be considered to be a *single domain*. However, when these fields are reduced, other domains can form in order to minimise the overall magnetisation, which often remains at zero field.

Smaller ferromagnets exhibit the property of magnetisation alignment with an applied magnetic field, though below a certain critical size they will not form domains but may form states (see section 2.8.3).

2.8.3 States — microstructures of magnetisation

At nanometre length scales in magnetic samples, particularly interesting states occur (see figure 2.14) as a result of the system attempting to reduce its overall energy.

The *single-domain* state, also called the *monodomain* state (see figure 2.14, top left), occurs when an infinitely large external field is applied to a magnetic material. In small particles, the single-domain state is often maintained as the field is reduced since the exchange energy is the most dominant term.

The *C* state (see figure 2.14, top centre) is known as such because the magnetisation direction roughly reflects the curve of the letter "C", tending to point along some direction in one part of the sample and gradually changing to the opposite direction in another part of the sample.

The *S* state (see figure 2.14, top right) is also named after the shape of the letter it reflects. The magnetisation undulates along the sample pointing initially in one direction, gradually turning towards another direction and then finally pointing back in the initial direction.

A cuboidal geometry of a certain size with a saturated magnetisation can fall into the *flower* state when an applied field is removed (see figure 2.14, bottom left). In this state the magnetic moments at the extremities point out of the sample along the overall magnetisation, and into the sample at the other side of the

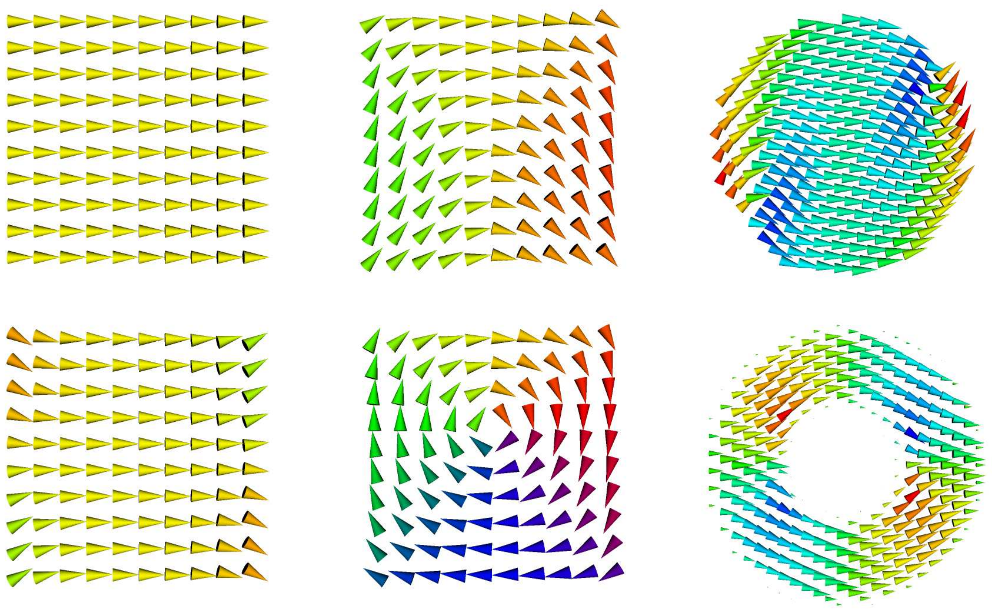

Figure 2.14: Common metastable states of magnetisation microstructures. *Top row*: (left) single-domain state — homogeneous magnetisation, (centre) C state and (right) S state. *Bottom row*: (left) flower state, (centre) vortex state and (right) onion state. The colour indicates the in-plane angle of magnetisation; the square samples are of size order ≈200nm, the circular samples of size order ≈500nm. Parameters for isotropic nickel ($A = 8.5\times10^{-12}$ J/m, $M_s = 4.93\times10^5$ A/m, $K_1 = K_2 = 0$ J/m^3) were used in these sample simulations.

overall magnetisation. Further examples showing the *C*, *S* and *flower* states can be seen in *Huang* (2003).

At lower fields, or in larger sample sizes, the *vortex* state might occur (see figure 2.14, bottom centre). This is where the magnetisation in a sample curls in order to minimise its dipolar energy, except at the centre, or *core*, of the vortex, where a minimisation of exchange energy causes the magnetisation here to point in one particular direction; in this case out of the plane.

In ring samples the *onion* state (see figure 2.14, bottom right) is likely to occur as an applied field is reduced. This state often occurs prior to vortex nucleation. The majority of the magnetisation is homogeneous, however towards the edges the magnetisation tends to follow the shape of the sample.

2.9 Computational Issues

To perform micromagnetic simulations, two different procedures are necessary depending on whether the *OOMMF* software (*Donahue and Porter*, 1999) or *magpar* (*Scholz et al.*, 2003a) is used to determine the demagnetising field.

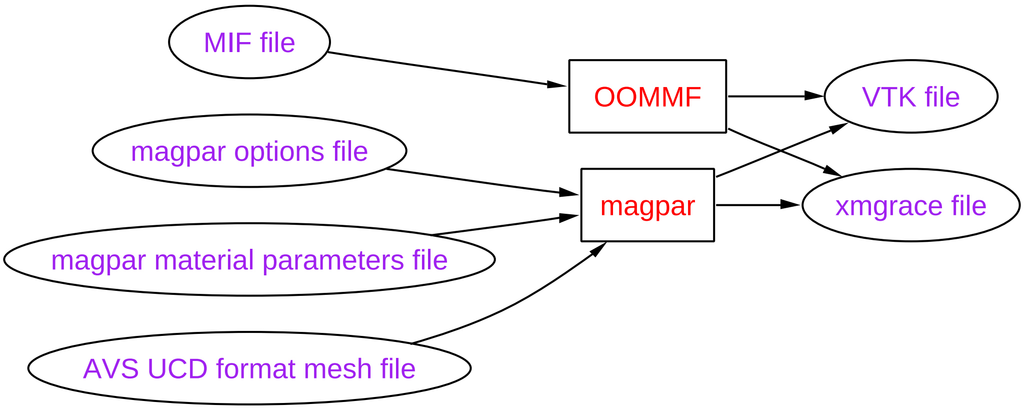

Figure 2.15: The simplified simulation process. The left-hand side of the chart represents the input files for the simulation packages for OOMMF (finite difference method; the *m*icromagnetic *i*nformation *f*ormat file contains material, simulation and geometric parameters) or magpar (hybrid finite element/boundary element method, material; simulation and geometric (mesh) parameters as individual files). The results from each of these packages are transformed into unified output formats (right-hand side) for analysis (xmgrace (*Turner*, 1995)) and visualisation (VTK)

2.9.1 *OOMMF* software requirements

We use three pieces of software to perform micromagnetic studies with the finite difference method. Each of these packages is an extension on other widely-available applications (see figures 2.15 and E.1).

The first piece of software is a proprietary program, *mifmaker*, which we developed to create simulation environments. Ordinarily a significant amount of manual effort is required to generate a simulation, as the problem must be directly defined in a Tcl-based format which *OOMMF* can recognise. There is no method built-in to *OOMMF* which allows this process to be automated for three-dimensional problems. The *mifmaker* program is a command-line application which can accept a series of geometric, material and simulation parameters and generate a valid *OOMMF* problem description.

Using *mifmaker* it is straightforward to generate batches of valid simulation problems which can subsequently be solved. This is ideal for performing size-dependence studies and generating phase diagrams. The operation of *mifmaker* depends on *Python* (*Hetland*, 2002, *Lutz and Ascher*, 2003, *van Rossum and Drake*, 2001).

After the appropriate magnetic problem has been generated by *mifmaker*, this is sent to *OOMMF* — the *Object Oriented MicroMagnetic Framework* — developed by the National Institute of Standards and Technology. *OOMMF* can then solve the micromagnetic problem which we have presented to it. *OOMMF* is heavily dependent on *Tcl/Tk* (*Ball*, 1999, *Flynt*, 1999, *Raines and Tranter*, 1999, *Smith*, 2000, *Welch*, 1999).

Figure 2.16 shows how the requirements for system memory in *OOMMF* scale in a cubic system (*i.e.* the length of the x, y and z sides of the cube are the same

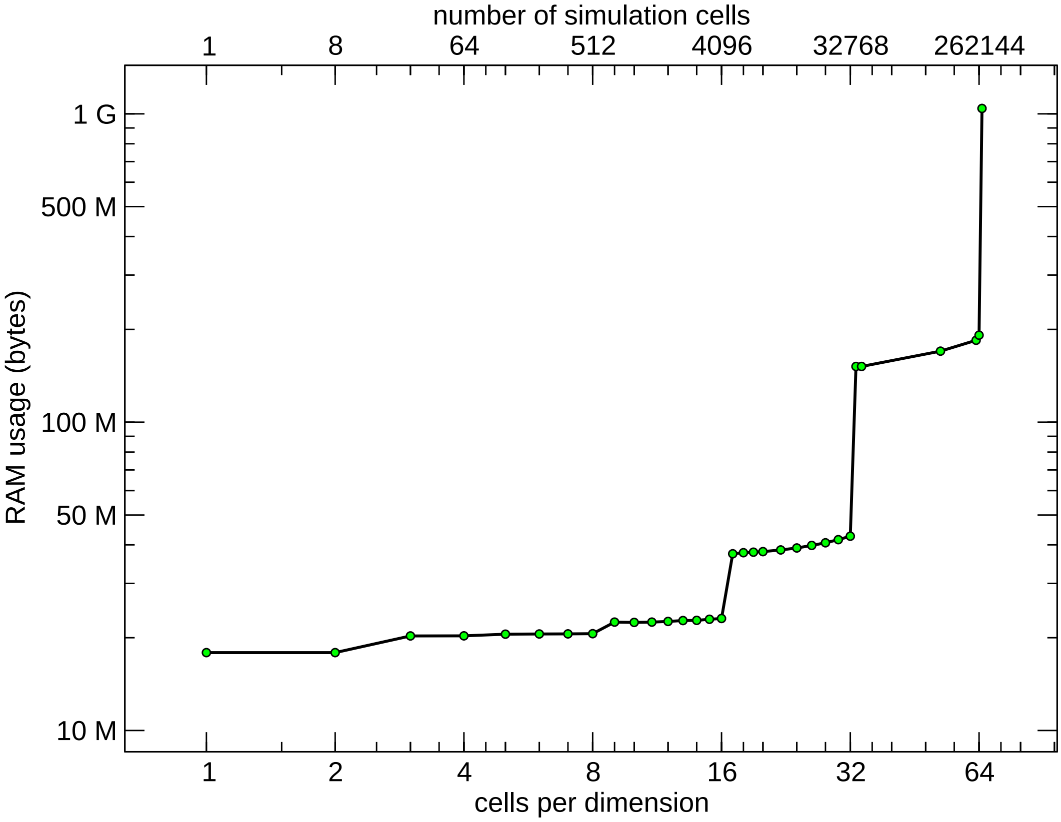

Figure 2.16: The memory requirements of *OOMMF* as a function of the number of discrete simulation cells per edge for a three-dimensional geometry

length and have the same discrete cell size) as a function of the number of cells.

2.9.2 *magpar* software requirements

The procedure for hybrid finite element/boundary element problems is more complicated. The *magpar* software (*Scholz et al.*, 2003a) requires that the geometry of the problem be defined with a finite element mesh. For this, any finite element modelling software can be used, provided that its output is converted to the AVS unstructured cell data (UCD) format. We used the finite element mesh generator *NETGEN* (*Schöberl*, 2003). Natively, this software does not create AVS/UCD format files, however it does have a fairly flexible approach to constructive solid geometry (CSG) allowing for the creation of complex geometries.

Figure 2.17 shows how the memory requirements of *magpar* scale as a function of both the number of surface elements and the volume elements, while figure 2.18 demonstrates *magpar* and *OOMMF* memory scaling.

In order to prepare the neutral file format created by *NETGEN* for *magpar* we created a custom *Python* script to convert this file to an AVS/UCD-compliant mesh.

The simulation problem and material parameters are generated with another

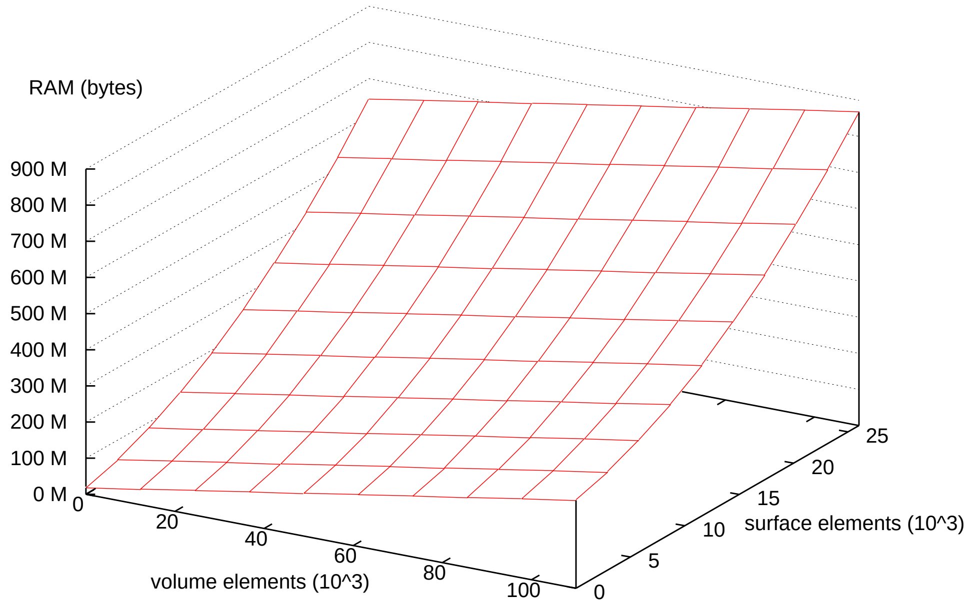

Figure 2.17: Memory usage scaling with *magpar* derived from runtime measurements

bespoke *Python* script to create the complex input files required for simulation with *magpar*. At this point the problem can now be solved using either a standalone uniprocessor or symmetric multi-processing workstation, or a clustered supercomputer.

Further details can be found in appendix E.

2.9.3 Post-processing

Finally, to visualise the results of the simulation, the magnetisation vector datasets are transformed from either the *OOMMF* format or the *magpar* format to the *Visualisation Toolkit* (VTK) format, an open standard for visualisation. These results are visualised with *MayaVi*, a piece of data visualisation software initially developed to assist with the visualisation of computational fluid dynamics environments. *MayaVi* depends on *VTK*.

All of these applications should run in any operating system environment for which an ANSI-compliant C/C++ compiler is available, however in this project we have only made extensive use of GNU/Linux and Microsoft Windows machines running on either Intel or AMD processors.

We have written many other smaller tools to assist with pre- and post-processing of data files generated by all of the aforementioned applications.

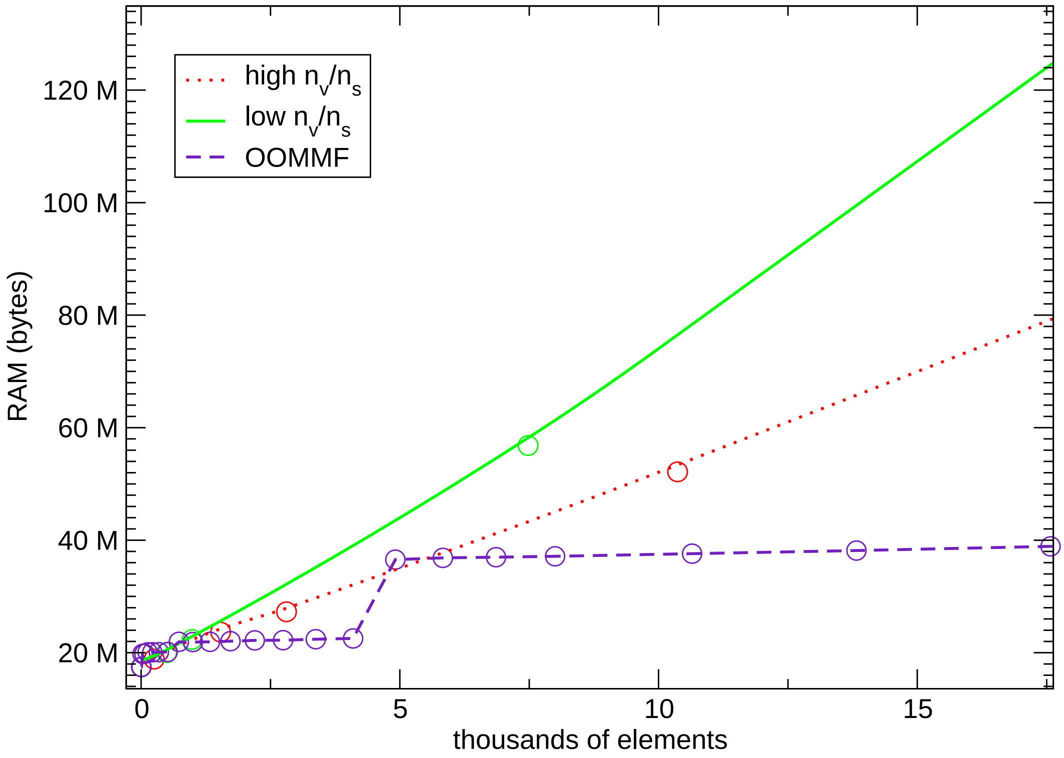

Figure 2.18: Memory usage of *OOMMF* and *magpar*. The dotted lines for *magpar* represent a high volume element to surface element ratio (*i.e.* a sphere) and the solid line represents a low volume element to surface element ratio (as in a thin film). Curve fits are shown for *magpar*; in all cases the circles represent measured results.

2.9.4 Hardware requirements

Theoretically, these pieces of software have modest hardware requirements, however as with all simulation problems of this nature "bigger is better". Ideally, a machine with a minimum of one gigabyte of RAM should be used to maximise the size of the potential problem which can be solved.

Each discrete cell within a micromagnetic problem to be solved with *OOMMF* consumes approximately one kilobyte of RAM, therefore to solve a system with 1×10^6 cells, one gigabyte of RAM is required just to run the simulation. This is without taking into account the size of the simulation package itself, which must be loaded into RAM and creates a fixed overhead.

Once operating system overheads are considered, it is clear that the amount of physical system RAM available to a machine should be greater than the amount of RAM required by the simulation — this is primarily to avoid "thrashing", a situation where the operating system is forced to temporarily write ("swap") areas of the RAM to the hard disk and read other areas back into RAM from the disk. The precise amount of RAM required for operating overheads will vary from system to system; a system dedicated and optimised for performing only simulations may only need a few megabytes reserved for the operating environment, but a workstation which is running other applications concurrently (*e.g.* visualisation software, e-mail clients, document editors and Internet web browsers) may require several hundreds of megabytes.

Bearing in mind that the access times in modern hard disks are several orders of magnitude greater than those of RAM (these access times are measured in milliseconds for hard disk drives and nanoseconds for RAM), this will slow down any particular simulation by this factor, making successful completion of the simulation impossible from a practical standpoint. Even in an optimised scenario where data seek latency is eliminated, the hard disk can be expected to deliver data approximately 100 times more slowly than RAM (*Barclay et al.*, 2003).

The speed at which the processor can perform floating point calculations is overwhelmingly the primary factor when considering the time a simulation will take to complete. Any processor which has a fast floating point unit coupled with a compiler which is able to take maximum advantage of this floating point unit when optimising the simulation source code is ideal — through our own studies we note that carefully chosen compiler options can increase the execution speed of the simulation threefold.

Additional methods such as high-throughput batch processing (*Litzkow*, 1987, *Litzkow et al.*, 1988) and clustering (*Ridge et al.*, 1997) allow either sets of simulations to be performed (*e.g.* many small computations such as those needed for phase diagrams) or larger computations which would be impossible to compute with neither the memory capacity nor the processing power of a supercomputer. *OOMMF*, unlike *magpar*, is unable to take advantage of the message-passing interface (*Snir et al.*, 1995, *Walker*, 1992) common to computational clusters.

2.9.5 Disk space

A collection of large hard disks is also beneficial to allow the long-term storage of previous simulation runs, assisting with the rapid retrieval of past vector data created by simulations.

Either 32-bit (single precision) or 64-bit (double precision) floating point numbers (*IEEE*, 1985) can be used to store the components of the vector data. The case for selecting one precision over another can be argued (*Goldberg*, 1991) from two perspectives: storing 32-bit numbers will save disk space if the extra precision offered by 64-bit numbers is not necessary, however vector interpolation used by certain visualisation techniques (*e.g.* the calculation of streamlines, figure 2.20) may benefit from a higher-precision. Further arguments for the use of single or double precision numbers can be found in *Bennett Goldberg* (1967), *Demmel* (1984), *Goldberg* (1991) and *Knuth* (1998). It is worth noting that *OOMMF* will perform the simulation using double precision numbers irrespective of the precision of the output format, and the solver component of *magpar* (*Balay et al.*, 2002, 1997) uses double precision numbers.

Double precision floating point numbers usually require eight bytes of storage each. To store the magnetisation vectors for a given mesh in *OOMMF*, each position of the mesh requires three 64-bit numbers to describe it (x, y and z components). This gives a simple equation for calculating the amount of space needed to store one set of magnetisation data for a simulation:

$$s = a + \frac{l_x}{c_x}\frac{l_y}{c_y}\frac{l_z}{c_z}\frac{3p}{8} \tag{2.41}$$

where a is the space consumed by a header describing the relationship between the vector data and the simulation, l_x, l_y and l_z represent the size of the complete mesh, c_x, c_y and c_z are the edge lengths of the discrete cell and p is the number of bits used to store one floating point number. Note that with *OOMMF*, even empty cells (*i.e.* where $|\mathbf{M}| = 0$) are stored by default.

For example, to store the magnetisation vectors for a sphere of diameter 120nm ($l_x = l_y = l_z = 120 \times 10^{-9}$m) with a cubic mesh cell size of 5nm^3 ($c_x = c_y = c_z = 5 \times 10^{-9}$m) with 64-bit precision ($p = 64$), $(120/5)^3 * (8 * 3) = 331776$ bytes of disk space are needed, plus a small fixed overhead. If a coarser mesh were used, such that $c_x = c_y = c_z = 10 \times 10^{-9}$m, then only 41472 bytes of disk space are necessary to store the magnetisation data for one timestep.

For a complete simulation many sets of magnetisation vector data are stored, each usually representing a particular “stage” — a point where the magnetisation configuration for an externally adjustable factor, such as applied magnetic field, is considered stable. A typical simulation might have 100 of these stages. In the case of the sphere example above, this equates to over 31 megabytes of disk space. For a sphere of double the diameter with a high field step resolution (giving 1000 stages if $-500\text{mT} \leq B_x \leq 500\text{mT}$ and B_x is reduced in 1mT steps), over 2.5 gigabytes of storage space would be necessary. Doubling the mesh resolution and the diameter further, such that $c_x = c_y = c_z = 2.5\text{nm}$ and $d = 480\text{nm}$, the amount of required disk space grows to well over 150 gigabytes.

2.9.6 Commodity computing

Although it is possible to perform micromagnetic simulations on a local workstation, throughput is limited. Having only one CPU means only one simulation can be effectively performed at one time. When more CPUs are available to use then more simulations can be performed simultaneously, making parameter dependence studies such as phase diagrams practical.

By configuring several powerful local workstations with MPI (*Snir et al.*, 1995), it is possible to perform simulations normally impractical; code which can take advantage of MPI environments such as *magpar* is capable of using the total available memory of those MPI-enabled machines effectively as one contiguous block — this allows larger simulations to be performed.

Condor (*Litzkow et al.*, 1988) provides another mechanism for distributing and computing smaller problems. Whereas high-performance commodity computing systems such as Beowulf require dedicated compute resources, Condor is designed to take advantage of the CPU cycles left idle on “normal” workstations. Since these workstations are not dedicated, the jobs which run on them generally relinquish their resources when the owner of the workstation returns. Useful results can therefore only be acquired if the jobs which run via Condor are capable of completing in a short time.

Iridis is the University of Southampton’s Linux-based clustered computational facility, consisting of several hundred Intel and AMD processors. Time is reserved in advance on this system and scheduling priority organised according to the size of the job in terms of CPU hours and node availability. As a dedicated compute resource it is designed to handle both batch and MPI jobs according to requirements, however competition for CPU cycles means that only a relatively small proportion of the total power can be used by an individual.

By using Iridis for extended studies with several variables, Condor for phase diagrams on smaller samples and optimised local workstation clusters for the most extreme situations, a varied cross-section of results from the different software can be acquired.

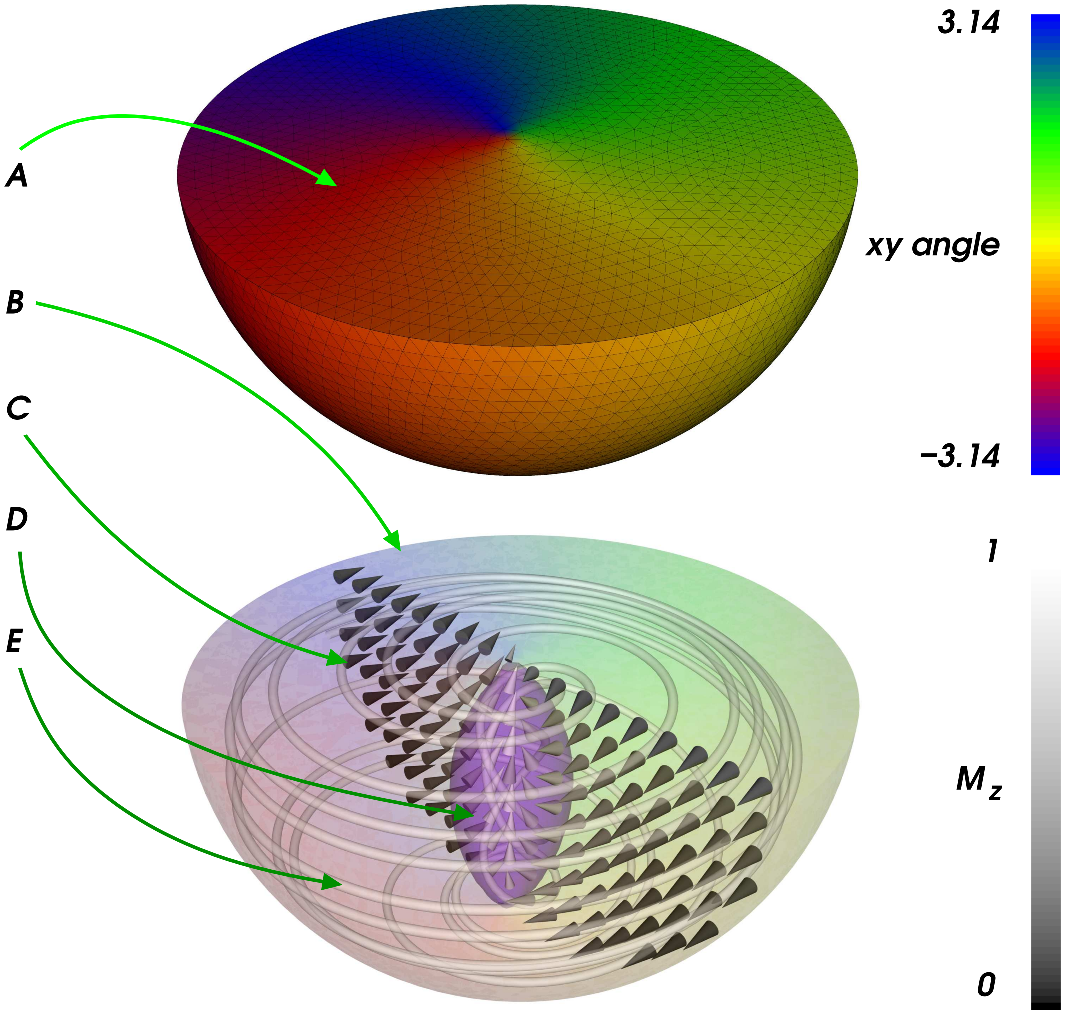

Figure 2.19: A visualisation showing a surface map (A), translucent surface map (B), area mean magnetisation vectors (C), isosurface (D) and streamlines (E)

2.9.7 Visualisation

Visualisation is an important part of scientific computation, both for the analysis of results and their presentation. To visualise computed results, we use MayaVi (*Ramachandran*, 2001), which makes use of Kitware's VTK (*Schroeder et al.*, 1996, 1997) as the middleware for preparing the data prior to being rendered in either POV-Ray or a Pixar Renderman® (*Pixar*, 1989, 2000) compliant raytracer.

We can exploit the features of these tools, particularly by adding features commonly found in computational fluid dynamics to further our understanding of the magnetisation patterns resulting from our simulations.

Figure 2.19 shows a typical visualisation. Point A in the upper image shows the surface map of a scalar, in this instance the xy angle of magnetisation. For clarity a wireframe map showing the outline of the finite element mesh is visible. In the lower image, the scalar surface map remains, though it is translucent (point B). The

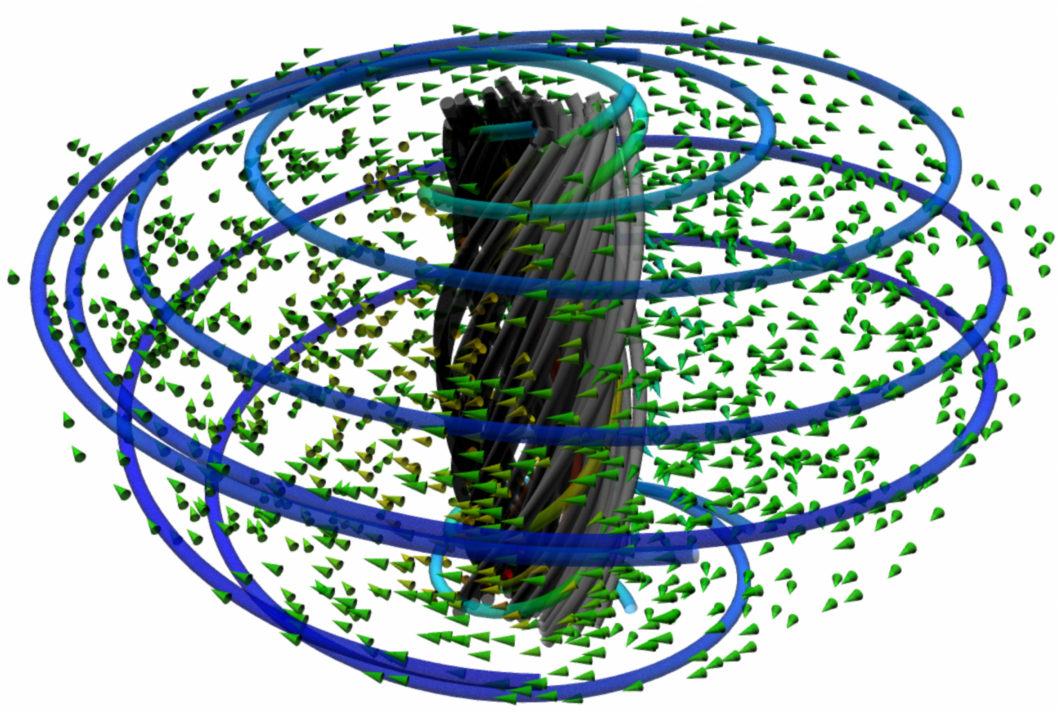

Figure 2.20: Vortex at the core of a droplet object (see section 5.5) highlighted with streamlines (massless particles, or *tracers*) injected into the material. At the edges of the sample these follow the magnetisation as if it were a velocity field; at the core these follow the curl of the magnetisation.

cones indicated by point C represent the mean magnetisation of the small area immediately surrounding the cones; the colour shows a scalar (the z component of the magnetisation) and the direction of the cone reflects the magnetisation vector itself. Where smaller cones are present in a visualisation, these represent an interpolation of the vector where source data is only available around that point rather than at the point itself. This usually takes place at boundaries, arising from a linear interpolation between $\mathbf{M}$ and 0.

To highlight points of interest, an isosurface of a scalar (such as that indicated by point D) may be shown. The isosurface in this example is again based on the z component of the magnetisation and attaches a visual representation to the core of a vortex. Finally, point E shows streamlines, which are the result of tracer particles being “dropped” into the system. These tracers follow the path of the magnetisation and provide a visual cue for interesting features of the visualisation; here they gradually follow the magnetisation around the surface of the sample, spiralling in until they reach the vortex core.

Where the volume of the sample is of particular interest, a random point mask can be applied to the visualisation, such as that in figure 2.20. Here streamlines have again been used to add depth to the visualisation and by operating on a derived vector (in this case, the curl of the magnetisation) the bounds of the vortex

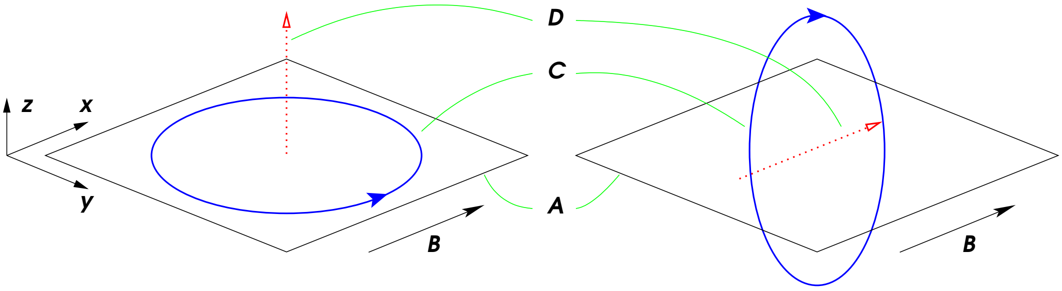

Figure 2.21: Schematic of out-of-plane (left) and in-plane (right) vortices. The dotted red arrow indicates the vortex core direction; the solid blue arrows show the magnetisation circulating around the core

core are clear.

Python (*van Rossum*, 2003) and Linux shell scripts (*Ramey*, 2003) were employed extensively in coordinating the process to take raw simulation results and produce camera-ready images and animations suitable for the analysis of magnetic microstructures.

Schematic drawings are occasionally used to assist understanding physical geometry or aspects of magnetisation. Figure 2.21 shows two schematics of a generic sample with arbitrary shape and a symmetry in the xy plane (point A), here represented by a rhombus. The axes on the left indicate the three-dimensionality of the sample. If the applied field (point B) were initially applied along the x direction, then two possible vortex types emerge. The vortex shown in the left sample has an *out-of-plane* vortex, where the magnetisation circulates in the xy plane (point C, solid blue arrow) and the core of the vortex (point D, dotted red arrow) points perpendicular to this symmetric plane, *i.e.* in z. The vortex shown in the right sample has an *in-plane* vortex — the circulation of the magnetisation (point C, solid blue arrow) is in the yz plane and the core of the vortex (point D, solid red arrow) is aligned with the direction of the initial applied field, *i.e.* in x.

2.10 Applications

Micromagnetic modelling is important to understand the behaviour of modern hard disk media and the research of novel materials and designs which could be incorporated into future hard disk platters.

Other emerging applications such as magnetic RAM can also benefit greatly from the investigation of micromagnetic systems offered through simulation techniques.

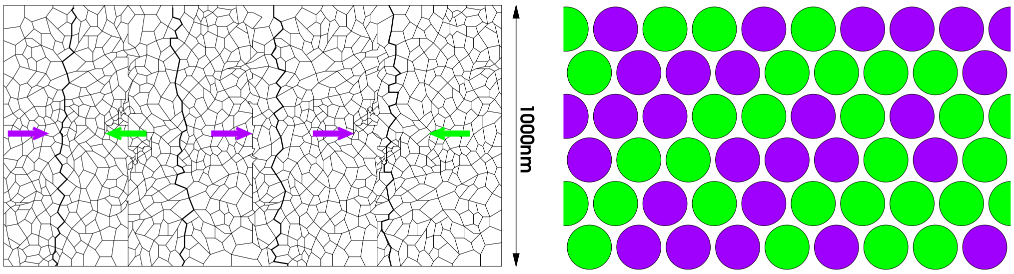

Figure 2.22: A schematic representation of non-patterned media is shown on the left, such as that used in traditional hard disk media (*Albrecht et al.*, 2003, *Süß*, 2002); the thicker line delimits one bit. The representation shown on the right is that of patterned media with each "dot" containing a single bit

2.10.1 Patterned and non-patterned media

Most modern hard disk drives have non-patterned media platters. The platter consists of a substrate, usually made of glass (though in the past aluminium and magnesium have been used), and is plated with nickel-phosphorous. On top of this substrate a magnetic cobalt-chromium-platinum-tantalum (CoCrPtTa) film is deposited by evaporation. This results in an irregular structure approximated in figure 2.22; the sizes of the individual grains within this structure are approximately 20nm in size (*IBM*, 2002), though the grain size in the most recent disks is around 5mn (*de Groot*, 2005). When pieces of data are written to this film, they are written along tracks shown by the dashed lines in the figure; the magnetisation of the crystals within the area representing that bit is set to a binary state. When the pieces of data are read back, the drive takes a mean of the magnetisation as measured by the head and decides whether that particular segment should be a 'zero' or a 'one', *i.e.* a *bit* of data. Typically, one bit is made up of 20 grains by 50 grains, giving a total physical bit size of 400nm × 1000nm ($0.4\mu\text{m} \times 1\mu\text{m}$) (*IBM*, 2002). Figure 2.1 shows the relationship between bit size and storage capacity.

Advancements in hard disk drive technologies have allowed capacity and performance increases in a similar order of magnitude to that of computer processors — traditionally doubling approximately every eighteen months but recently every twelve months; for example, the giant magnetoresistance (GMR) effect discovered in 1988 (*Baibich et al.*, 1988) gave manufacturers a head technology capable of reading smaller physical data bits on account of their increased sensitivity. Subsequently, to increase data density, manufacturers can reduce the width of the tracks; at 6 Gbit/in^2 this is approximately $1\mu\text{m}$.

At some point it becomes impossible to reduce the track width any further whilst ensuring reliability, and consequently data integrity, as there are too few CoCrPtTa grains within the track width to guarantee a particular overall state (*i.e.* zero or one); a very narrow track may reduce the strength and therefore the "clarity" of the read signal. To increase reliability, manufacturers must reduce the size

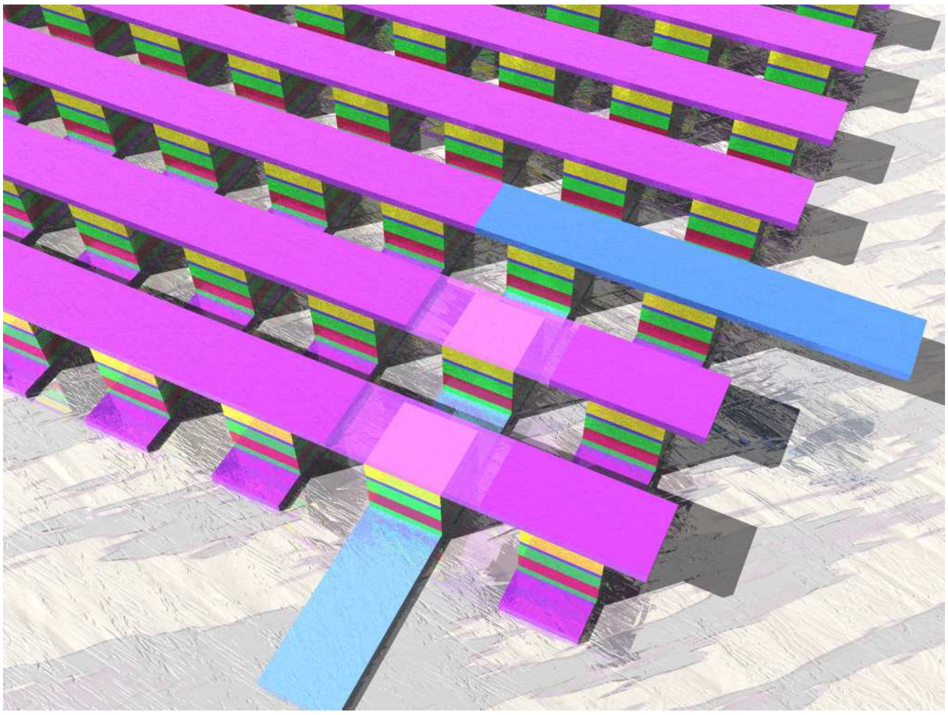

Figure 2.23: A depiction of how data can be accessed in MRAM; light blue areas represent the read path. Between the purple tracks, from top to bottom: free ferromagnet (yellow), tunnel junction (dark blue), pinned ferromagnet (green), antiferromagnet (red), seed layer (dark green)

of the particles which coat the substrate, thereby increasing the relative number of grains representing one state; if these particles fall below a certain critical size, the superparamagnetic effect may reverse the magnetisation in individual grains due to thermal fluctuations.

Patterned magnetic arrays (*Ross*, 2001) at a nanoscopic level are becoming feasible as hard disk storage media (*Chou*, 1997, *Chou et al.*, 1996) owing to advancement in fabrication processes (*Cowburn et al.*, 1999a,b), including self-assembly techniques (*Bartlett et al.*, 2003a, *Hoinville et al.*, 2003, *Mayes et al.*, 2003, *Zhukov et al.*, 2004a, 2003). However, to understand *what* precisely should be assembled, a study is needed into the relative merits of the entities making up the array; indeed, as nanoscopic length scales are approached, the physical shape of an entity becomes more important (*Aharoni*, 2000, p115) than other factors, such as magnetocrystalline anisotropy, because it will affect increasingly the characteristics of the hysteresis loop (see section 2.8.1). In chapter 5 we investigate the properties of such nanodots.

2.10.2 Magnetoresistive random access memory

In 1974 IBM Research developed the magnetic tunnel junction, the main component of magnetostatic random access memory (MRAM). This tunnel junction is a sandwich of ferromagnetic and antiferromagnetic material between columns of bits and rows of words, allowing an "$[x, y]$"-like access to individual bits within the memory; this can be seen in figure 2.23.

MRAM has the potential to be fast and dense, but even more importantly, it is non-volatile *i.e.* it does not require a constant application of power to retain its state), unlike standard dynamic random access memory (DRAM). This non-volatility provides another benefit in the form of low-power consumption, making MRAM ideal for applications where power is paramount, such as laptop and palmtop computers, mobile telephones and portable music systems.

To help understand which particle shapes are useful as part of a typical MRAM configuration (*Teherani et al.*, 1999), it is beneficial to study these through simulation.

Chapter 3

Basic geometries: flat cylinders and spheres

3.1 Introduction

The knowledge which can be acquired from micromagnetic simulation reveals the underlying physical processes that govern the hysteresis loop. This complements experimental work in which the average magnetisation as usually shown in hysteresis loops is observed.

The ability to examine numerically the micromagnetic behaviour of a given ferromagnetic system is of particular interest to experimentalists because it allows us to investigate in great detail the microstructures of the magnetisation which form inside the system and observe their effects.

We wish to understand the micromagnetic behaviour of the droplets later presented in chapter 5 which our collaborators in Prof. Bartlett's group can fabricate and our collaborators in Prof. de Groot's group investigate experimentally. In this chapter we study some more fundamental geometries to prepare this investigation.

3.2 Prior work

Previous work with flat cylinders, *i.e* where the diameter of the circular plane is significantly larger than the height, has been done by *Cowburn et al.* (1999a,b). These papers present hysteresis loops and SEM micrographs for supermalloy single-domain circular nanomagnets (flat cylinders). The diameter d of these cylinders is between 55nm and 500nm, and their height h is between 6nm and 15nm. Cowburn concludes that there is a distinct behaviour switch between the vortex state and the single-domain state (see figure 3.1) dependent on the diameter of the nanomagnet, confirmed by micromagnetic simulation (*Dao et al.*, 2001). Two-dimensional simulation studies by *Gubbiotti et al.* (2002) show the vortex behaviour in circular permalloy dots of diameter 200nm. Other single-domain to vortex state

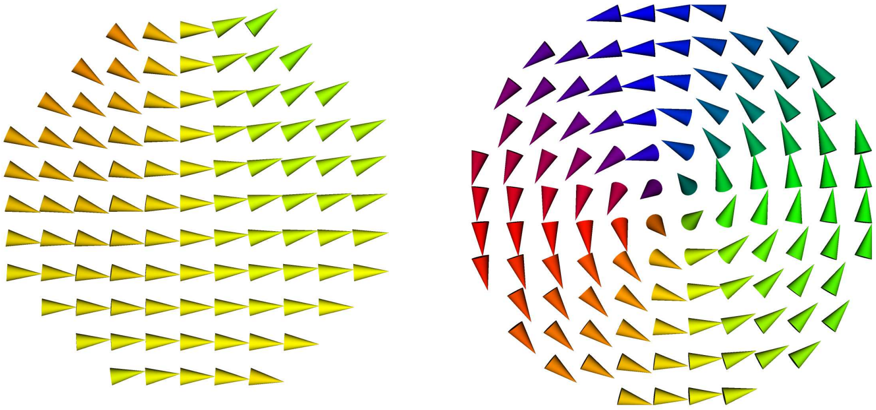

Figure 3.1: Two states: the single domain state (left) and the vortex state (right)

transitions and phase studies have been performed by *Scholz et al.* (2003b).

Ha et al. (2003) suggest that many interesting states are formed in permalloy cylinders, which are dependent on height, radius and applied field. In flat cylinders at zero field with a diameter of 200nm, they observe the onion state; when the diameter is doubled, the vortex state is apparent at zero field.

Initial micromagnetic studies of spheres have been previously performed (*Aharoni*, 1980, *C. H. Stapper*, 1969, *Eisenstein and Aharoni*, 1975) and the results of these studies indicate that there is a smooth, gradual reduction in the overall magnetisation of a sphere as the applied field is reduced. Later work (*Aharoni*, 1983) notes there is a form to the magnetisation transition which is not certain.

Mayes et al. (2003) and *Hoinville et al.* (2003) discuss the practicality of storing data on spherical cobalt-platinum nanoparticles, created using a biological process and provide experimental results when used directly as a coating on a hard disk platter.

In this chapter, we take this work further, and simulate and observe the behaviour of a sphere (*C. H. Stapper*, 1969, *Eisenstein and Aharoni*, 1975, *Lam*, 1992), with a diameter d of 200nm and a flat cylinder (disc) of diameter $d = 100$nm and height $2/5d = 80$nm; in both cases we use the material parameters for isotropic nickel ($M_s = 493380$ A/m, $A = 8.5 \times 10^{-12}$ J/m, $K_1 = 0$ J) with a damping parameter α of 0.25 to assist with convergence. We also demonstrate the different magnetic microstructures when the height of the cylinder is altered, and perform a diameter dependence study with the cylinder.

3.3 Parameterisation of geometry

To instruct *OOMMF* what geometry to simulate, a Tcl function (*Flynt*, 1999, *Welch*, 1999) describing a constructive solid geometry (see appendix F) needs to be written

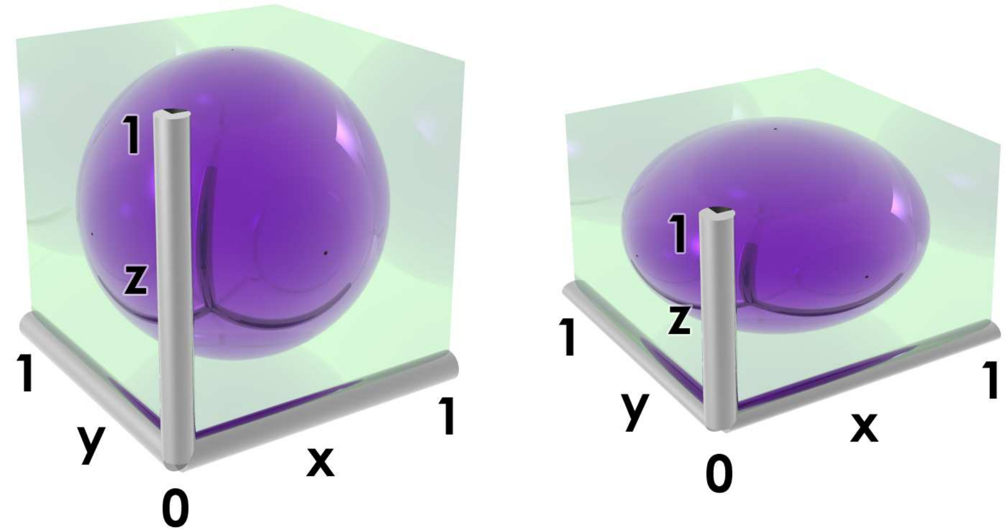

Figure 3.2: Anisotropic simulation domain. The image on the left has the physical x, y and z components of the simulation domain equal to each other — as such the inscribed geometry is a sphere — while the image on the right has the physical z component half the size of the physical x and y components, causing the inscribed geometry to be ellipsoidal. Both inscribed geometries are described by equation F.1

that is part of a problem configuration file. The convention chosen by OOMMF is to always operate in a geometric simulation space with internal coordinates ranging from 0 to 1 in all three dimensions (see figure 3.2). In addition, *OOMMF* requires knowledge about the absolute size of this simulation cell and will scale the normalised cell accordingly.

We have found this approach counterintuitive at times and have therefore written a Python program (*mifmaker*) which takes the size of the object we wish to investigate in absolute units, and will then create the necessary configuration file for *OOMMF* automatically, including the Tcl function to describe the geometry in normalised units. To generate a problem which will simulate a cobalt cylinder of diameter 100nm and height 40nm, with a mesh resolution of 2.5nm and an in-plane applied field ranging from 500mT to -500mT in 1mT steps, we need to issue the following command to *mifmaker*:

```
mifmaker --cylinder --material=cobalt --xy=100e-9 -z 40e-9 \
         -c 2.5e-9 -h 500 -l -500 -s 1000 --direction=down
```

The investment in creating this "one-shot" approach to generating micromagnetic problems pays off when the parameter space is to be explored systematically.

When OOMMF interprets the problem configuration file, it tests each point in the normalised geometric simulation space against the geometry function. At this point, the function can return results of either M_s or zero, depending on whether or not material is present at the point of test. By inverting the results when the

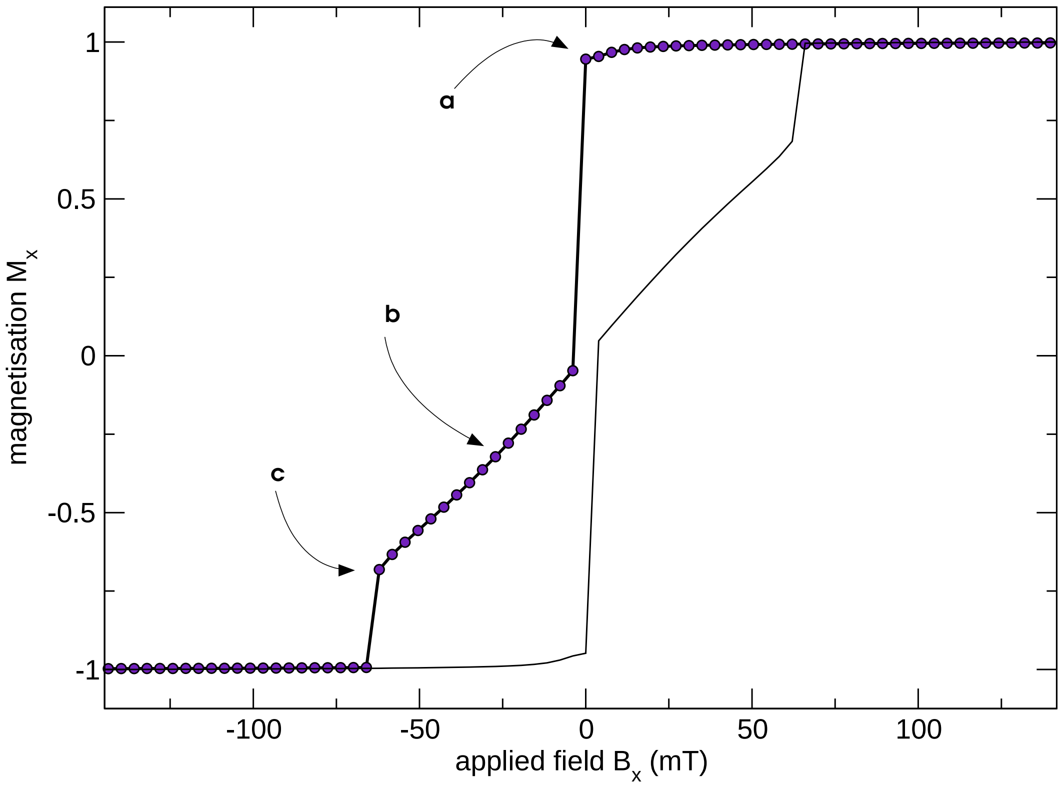

Figure 3.3: Hysteresis loop for a flat nickel cylinder of height 40nm and diameter 200nm. The points on the graph correspond to the states described in the text and figures 3.5, 3.7 and 3.8

conditions are met, negative geometries can be built up, such as the "antisphere" — a spherical hole in an otherwise solid (cubic) geometry.

3.4 Flat cylinder

We compute a hysteresis loop as shown in figure 3.3 in the following way: initially, a magnetic field is applied in the simulation such that the magnetisation across the cylinder is homogeneous (see figure 3.4).

For $B_x = 0$mT (point a in figure 3.3) the magnetisation appears roughly homogeneous (figure 3.5) but closer inspection (figure 3.6) reveals a slight out-of-plane magnetisation shift at either end of the sample due to a small contribution from the dipolar interaction. This can also be seen in figure 3.5 (*Bertram*, 1994), and overall an *onion state* occurs, present to minimise the dipolar surface charges (*Ha et al.*, 2003); this is shown in figure 3.6, and the homogeneous magnetisation state at this point can be seen with a normalised colour scale in figure 3.5 and corresponds to point a in figure 3.3.

As the applied field is reduced further a vortex forms in the x-y plane (figure 3.7). Note that this vortex (point b in figure 3.3) does not appear until *after* the applied field has passed zero; the vortex appears here as there is an energy

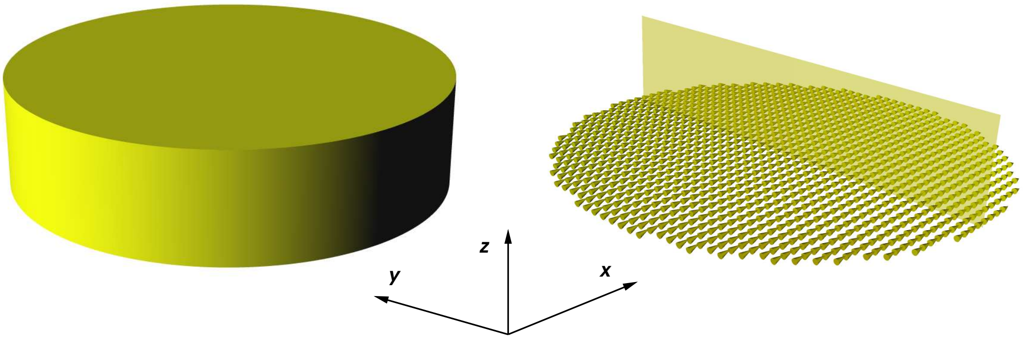

Figure 3.4: Overview of the cylindrical geometry (left) with the magnetisation (represented by the cones) in a high applied field (right). The rectangular surface on the right is a cut-plane through the sample, the colour of which reflects the scalar value of the in-plane $x - y$ angle.

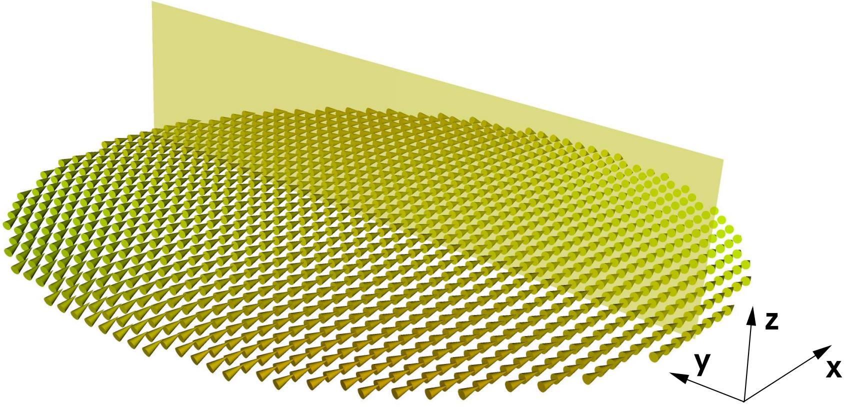

Figure 3.5: Flat cylinder with homogeneous magnetisation (point a in figure 3.3). The colour is representative of the in-plane x-y angle. There is a small out-of-plane magnetisation shift due to demagnetising energy at the edges which is not present in a high applied field (figure 3.4)

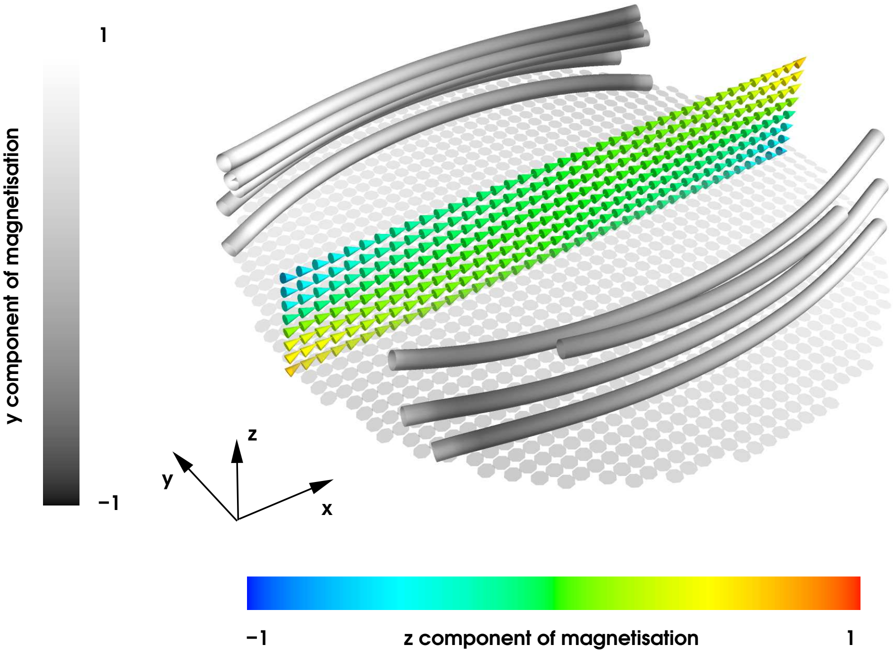

Figure 3.6: The flower state and the onion state shown together in a cylinder of diameter 200nm and height 40nm in zero applied field. The flower state is shown by the coloured cut-plane (xz) and exists in the x-z plane. The onion state is shown by monochrome streamlines which follow the magnetisation direction; this exists in the x-y plane.

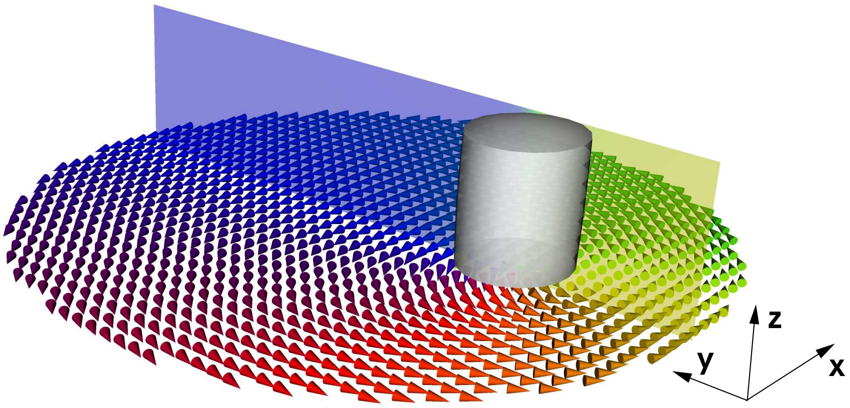

Figure 3.7: Flat cylinder entering the vortex state (point b in figure 3.3). The direction of the cones corresponds to the direction of the magnetisation; their colour shows their angle in the x-y plane — yellow is 0° from $+x$, blue is 180° from $+x$. The translucent cutplane in y-z shows the magnetisation pattern is consistent throughout the height, and the grey isosurface outlines the core of the vortex.

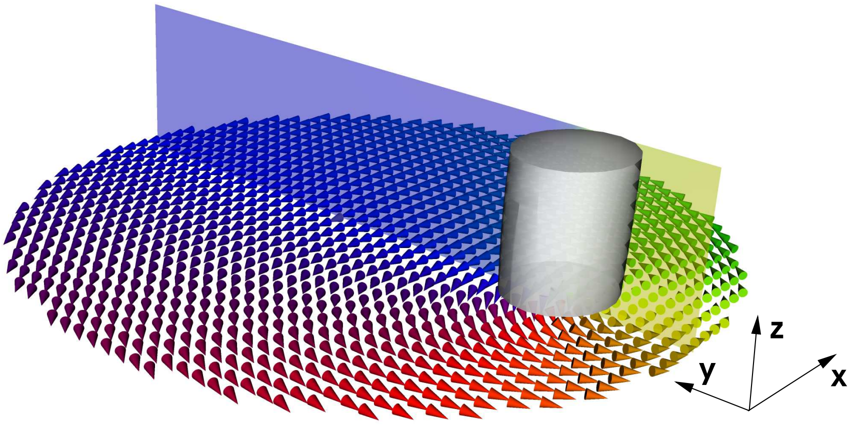

Figure 3.8: Flat cylinder just before leaving the vortex state (point c in figure 3.3).

barrier which it must first overcome. This results in the vortex forming slightly off-centre, so that when the vortex is created the magnetisation jumps from a high positive value to approximately $-0.1M_S$, where M_s is the saturation magnetisation (see figure 3.5). The position of the core of the vortex is a reflection of the amount of magnetisation which is following the applied field to minimise the Zeeman energy.

As the field is further reduced, the core of the vortex can be seen to pass through the cylinder in the negative y direction until $M_x = -0.7M_s$ (figure 3.8), corresponding to point c in figure 3.3; at this point the core of the vortex is close to the edge of the cylinder and disappears with another increase in the magnitude of the applied magnetic field, leaving the magnetisation once more homogeneous in the direction of the applied field, which is the opposite situation to that in figure 3.5.

Taking a cylinder of diameter 200nm, we study the microstructures of the magnetisation which form for different heights of a cylinder between 5nm and 100nm. Using the technique outlined in section 2.7.2 we assign a uniform magnetisation in

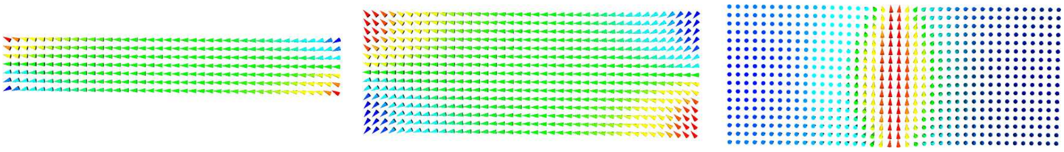

Figure 3.9: Height dependence of the remanent state in cylinders - vertical cutplanes in the xz plane of a cylinder of diameter 200nm in zero applied field are shown. The images are (left) a cylinder of height 35nm, (centre) h =75nm and (right) h =85nm. The colour variation represents the z component of the magnetisation.

the x direction, allow the system to relax in zero applied field, and make observations.

Figure 3.9 shows the flower state, clearly visible in the shorter cylinders; however as the height is increased, the dipolar energy exerts a greater influence, as in figure 3.6. The dipolar energy continues to exert more and more pressure on the cylinder to abandon its flower state in favour of a vortex — at a height of 75nm the top and bottom of the cylinder are completely dominated by the magnetostatic energy. Increasing the height a little further from here to 80nm causes this structure to collapse and fall into the vortex state at zero field.

Figure 3.10 shows the reversal behaviour of nickel cylinders dependent on height and diameter. As height is increased, the single domain behaviour disappears and vortex reversal behaviour occurs; the same is true as the diameter is increased.

3.5 Sphere

3.5.1 Finite differences and finite elements

Figure 3.11 depicts the hysteresis loops obtained from simulations of a nickel sphere (diameter d=200nm, K_1=0). The loops in the upper left, upper right and lower left of the figure show loops yielded with the *OOMMF* software, whilst the lower right loop was computed with *magpar*.

For each simulation, the applied field direction was varied in θ and ϕ, respectively the azimuth and polar angle of the applied field. These are relative to the orientation of the finite difference grid, aligned with the x-, y- and z-axes.

All the loops show a similar pattern just below saturation, with small openings in the hysteresis where the magnetisation moves from the single domain state into the vortex state.

It is interesting to note that in the loops computed with *OOMMF* there is an “opening” in the hysteresis loop around B_x=0, the size of which varies with the direction of the applied field, although it is never quite eliminated. The results from *magpar* do not display this characteristic.

These data show that the inner loop depends on the angles θ and ϕ. For the spherically symmetric system that we wish to simulate, how the coordinate system

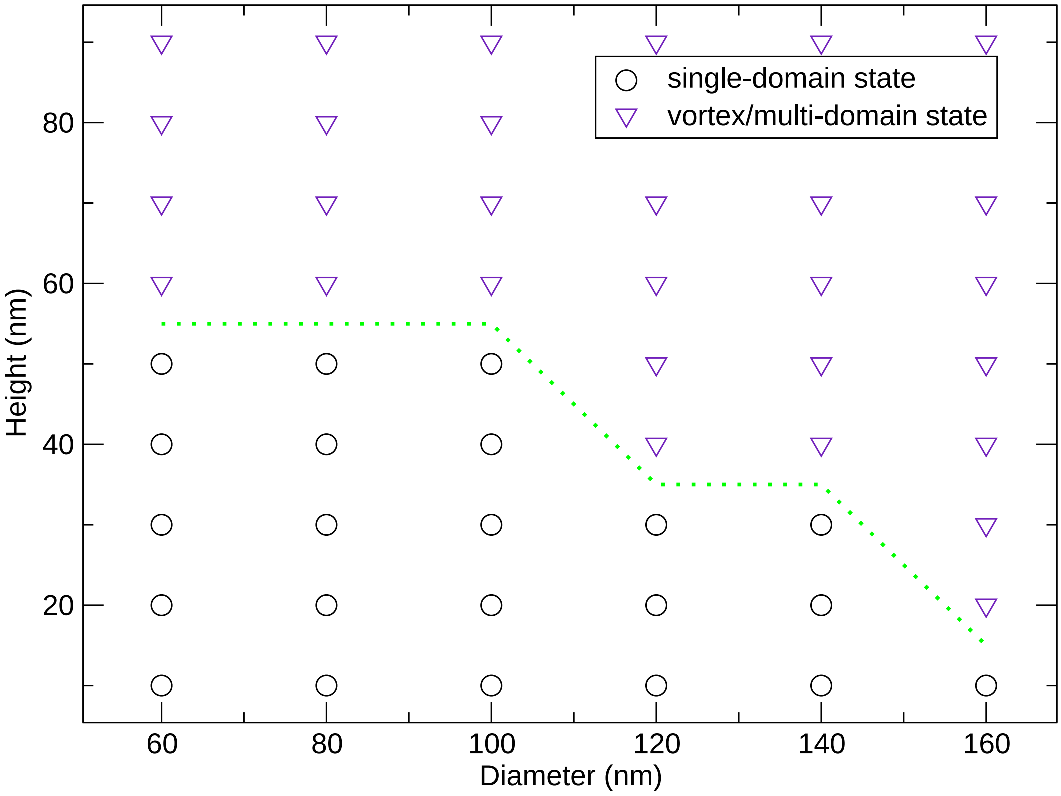

Figure 3.10: Phase diagram of the remanent magnetisation state for nickel cylinders of varying height and diameter

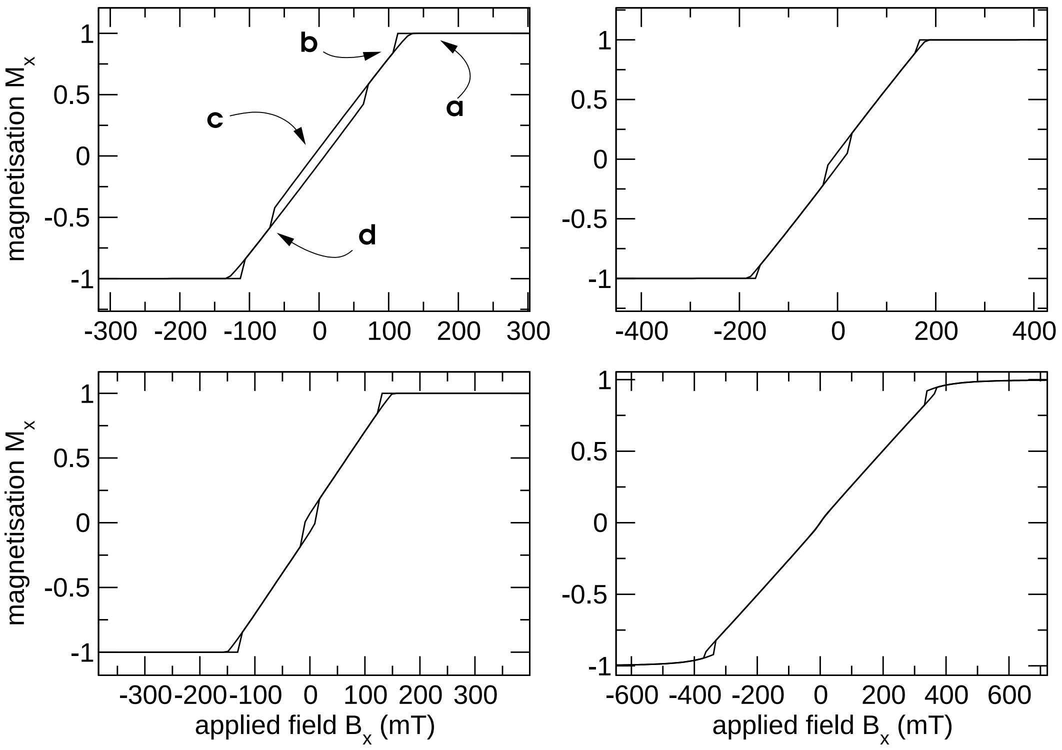

Figure 3.11: Hysteresis loops for nickel spheres of diameter d=200nm with no magnetocrystalline anisotropy with varying applied field offsets in xy (θ) and xz (ϕ). The top left hysteresis loop was performed with *OOMMF* with applied field offsets θ=45^o, ϕ=0^o. The top right loop (*OOMMF*) has θ=10^o, ϕ=0^o. The bottom left loop (*OOMMF*) has θ=30^o, ϕ=18^o. The bottom right hysteresis loop was performed with *magpar* using an applied field offset of θ=4^o, ϕ=6^o

of the simulation software is aligned relative to the direction of the applied field should be irrelevant. It is therefore likely that the inner openings in the hysteresis loops are an artefact of the finite difference simulation technique as these vary substantially as a function of this direction.

Initially, we assume the applied field is zero and the magnetisation forms a vortex with the core pointing in the x direction as shown later in figure 3.15, and a very small field is applied in the opposite direction (*i.e.* $-x$) such that the vortex structure of the magnetisation is not significantly affected. Since the overall magnetic moment of the magnetisation is finite and points in the direction of the moments in the vortex core, it is therefore energetically favourable for the system to align the vortex core with the applied field.

In order for this to happen, the vortex core needs to turn around by 180 degrees (*i.e.* point in $-x$ rather than $+x$. If there is no magnetocrystalline anisotropy in the system, the spherically symmetric sphere should allow the core to rotate round in either θ or ϕ, similar to a typical Stoner-Wohlfarth particle. The spherical symmetry should not allow the occurrence of the "inner" hysteresis loop indicated in figure 3.11; this is supported by the results presented in the lower right of figure 3.11 computed with the finite element code.

It is plausible therefore to assume that directions along the discretisation axis are either favoured or avoided by the system when a finite difference grid is introduced for symmetric geometries.

3.5.2 Reversal mechanism

A strong magnetic field applied across a nickel sphere of diameter 200nm gives a homogeneous magnetisation. As this field is reduced the magnetisation at the surface of the sphere diverges as a consequence of the dipolar interactions (figure 3.12 corresponding to point a in figure 3.11; also shown in figure 3.13); this behaviour is similar to that in small cylinders.

As the field is reduced, the sphere falls into the vortex state a little above 100mT (see figure 3.14, corresponding to point b in figure 3.11), but, contrary to the cylinder, this vortex forms *around* the axis of the applied field. The majority of the magnetisation at this stage is pointing in the direction of the applied field rather than against it, as the core of the vortex is aligned with the direction of the initial magnetisation. The magnetisation around the core of the vortex is able to maintain its circular vortex pattern and adjust its alignment with the present applied field.

At zero field, the magnetisation in the vortex core remains pointing in the direction of the applied field (figure 3.15, corresponding to point c in figure 3.11), however if the field is increased in the $-x$ direction then the magnetisation in the core is reversed (figure 3.16, point d in figure 3.11).

Further increasing the field eventually results in the vortex dissipating at around

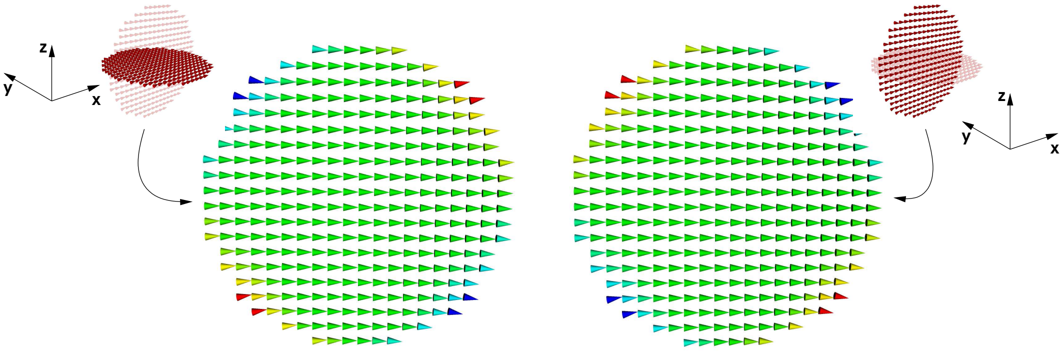

Figure 3.12: Nickel sphere in high applied field showing spin tapering owing to demagnetising energy; the left image shows a cut-plane through x and y, the right image shows a cut-plane through x and z. This corresponds to point a in figure 3.11

180mT. This results in the magnetisation of the sample pointing entirely in the direction of the applied field as in figure 3.13, only in the opposite direction.

3.5.3 Size dependence

A size dependence study was performed on the diameter of nickel spheres; the results of this can be seen in figure 3.17, showing a change in behaviour at a certain diameter.

There is a qualitative change in the magnetisation reversal when the diameter is reduced; the hysteresis loops for spheres of diameter 50nm and 80nm are shown in figure 3.18.

The following equation (*O'Handley*, 1999) gives the *critical radius* (*i.e.* the radius above which a sphere changes from single domain behaviour to vortex behaviour) of a spherical sample of some material which has a low anisotropy value.

$$r_{n+1} = \sqrt{\frac{9A}{\mu_0 M_s^2}\left[\ln\left(\frac{2r_n}{a}\right) - 1\right]} \tag{3.1}$$

Using this equation, one can quickly converge on the critical radius for nickel by iterating equation 3.1 until $r_{n+1} - r_n = 0$. The calculated critical radius of 34nm agrees well with our simulations of nickel spheres; these studies show that the magnetisation pattern of a nickel sphere of diameter 60nm ($r = 30$nm) reverses as a single-domain, and the magnetisation pattern when the diameter is 70nm is vortex-like.

3.6 Summary

We have studied the magnetisation reversal in nickel cylinders and spheres of the size order 200nm. Around this size, in nickel the samples will not tend to form

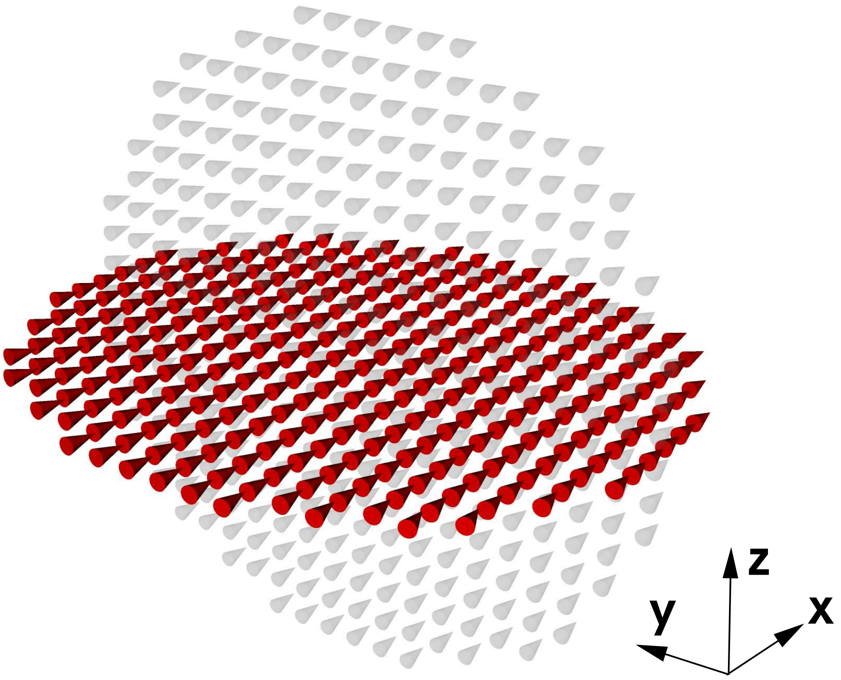

Figure 3.13: Sphere at high applied field (point a in figure 3.11); see also figure 3.12.

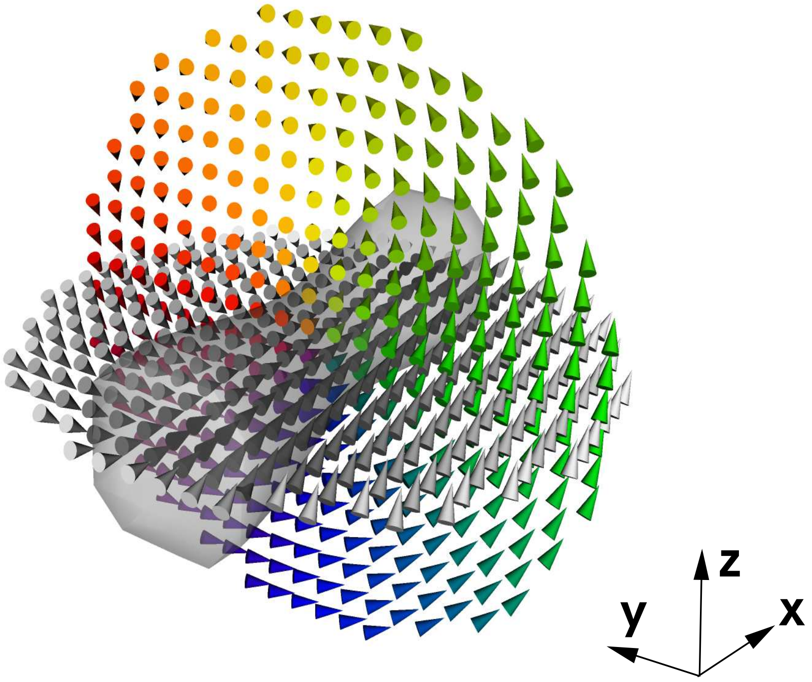

Figure 3.14: Sphere immediately after entering the vortex state (point b in figure 3.11).

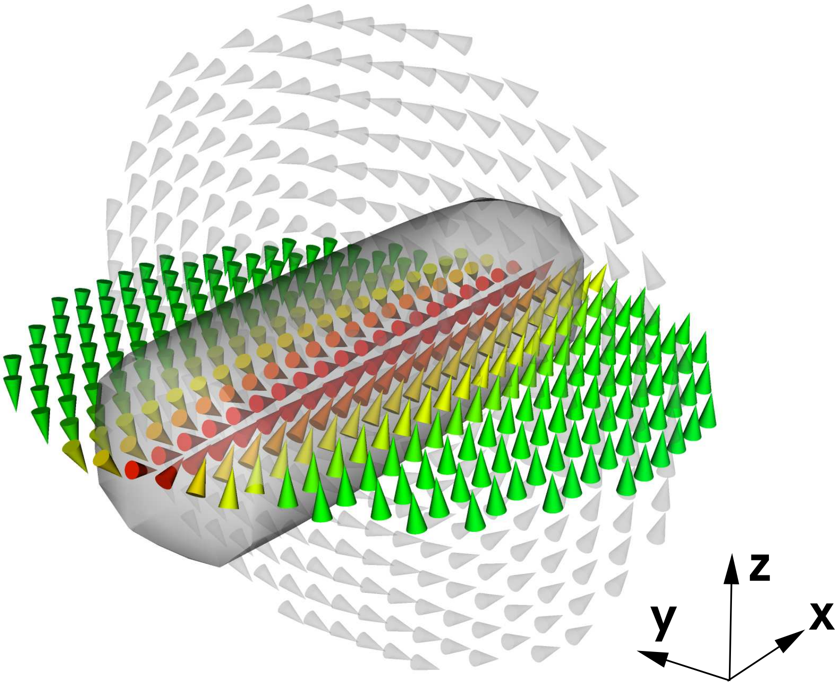

Figure 3.15: Sphere in vortex state (point c in figure 3.11).

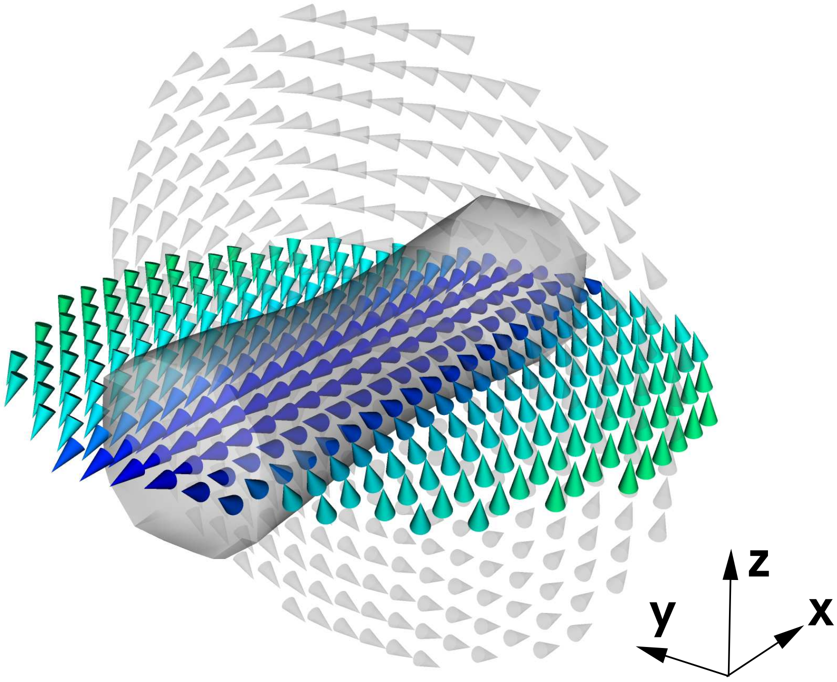

Figure 3.16: Sphere in vortex state at a further reduced field (point d in figure 3.11).

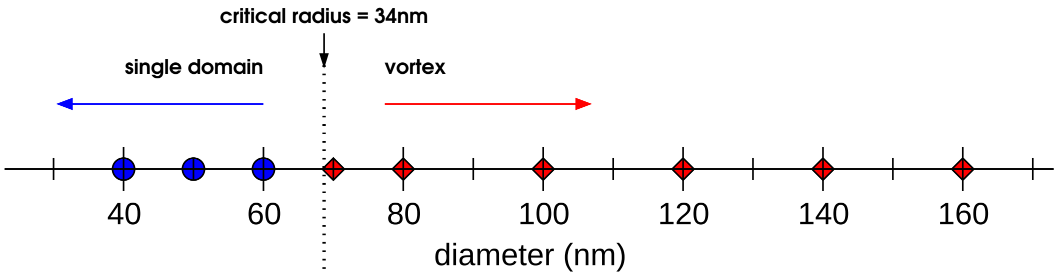

Figure 3.17: Size dependence of the domain state in nickel spheres. The vertical dotted line shows the critical radius for state transition computed with equation 3.1

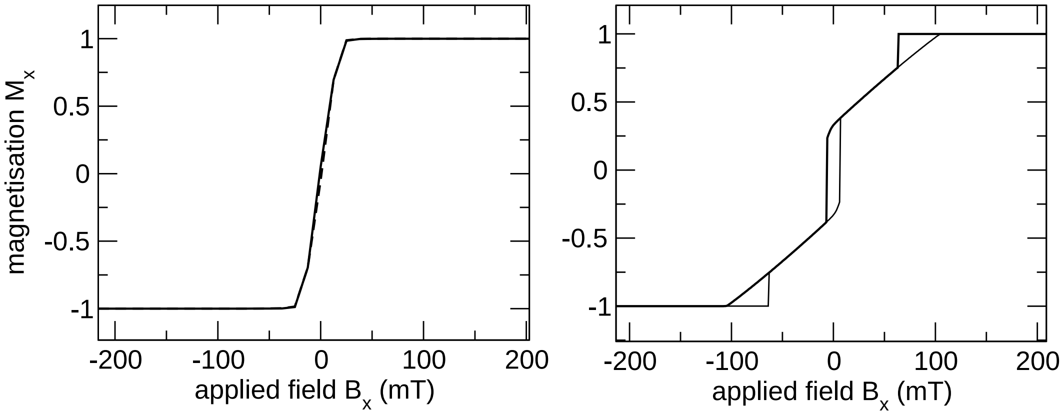

Figure 3.18: Hysteresis loops for nickel spheres of (left) diameter 50nm and (right) diameter 80nm. The 50nm sphere reverses through the single-domain state; the 80nm sphere through the vortex state

domain walls as the samples are physically too small — the energy from dipolar interaction is not great enough to counteract the domain wall energy — and neither will the shapes behave as single-domain states as the dipolar energy is then too great (*Wachowiak et al.*, 2002).

Below a certain critical diameter, cylinders exhibit single-domain behaviour. Above this critical diameter, the cylinders enter the vortex state. In this regime, the vortex penetrates and moves to adapt M_x to B_x after the field is reversed. In all cases, nickel cylinders cannot maintain a single-domain reversal method once their height is above a critical value; we find that the vortex reversal method is present in all cylinders with a height greater than 60nm. The results for the simulated cylinders are qualitatively in agreement with work by *Cowburn et al.* (1999b), however these cannot be compared directly because different materials have been investigated.

With the simulated spheres, vortex behaviour exists for a sufficiently large system, however the vortex penetrates at a greater applied field than that in a cylinder of comparable size. The vortex in spheres is also static with the core of the vortex pointing in the original direction of the applied field, as opposed to the vortex appearing in cylindrical samples, where the core of the vortex is able to move through the system to compensate for a change in applied field. In cylindrical samples, the core of the vortex is perpendicular to the direction of the applied field, *i.e.* it points out of the circular plane.

We have shown that for non-cuboidal structures, great care has be taken to ensure that the finite difference simulation technique does not introduce artefacts that do not reflect the behaviour of the physical system. In subsequent chapters we have used finite element simulations to corroborate finite difference simulation results, and varied the directions of applied field to ensure to exclude such artefacts from our observations.

Chapter 4

Cones

The work described in this chapter has been submitted to Physical Review B (*Boardman et al.*, 2005a).

4.1 Introduction

Tapered structures such as pyramids and cones are commonly used in magnetic force microscopy (*Dahlberg and Proksch*, 1999, *Sáenz et al.*, 1987); the phase shift induced by the movement of a cantilever attached to the structure can be interpreted to yield the stray field pattern of a sample (*McVitie et al.*, 2001).

Part-conical samples of size order $1\mu\text{m}$ and above have previously been fabricated for bubble devices (*Sanders et al.*, 1981). Nanolithographically defined structures created through electron beam lithography (*Chou*, 1997, *Chou et al.*, 1996) result in arrays of tapered pillars which are geometrically conical. The coercivity of arrays of shorter cones created with interference lithography has been previously investigated experimentally and numerically (*Ross et al.*, 2001).

In this chapter, we study the magnetic reversal behaviour of cones systematically and compute a magnetisation remanence phase diagram as a function of diameter and height.

4.2 Parameters

We use the material parameters for $\text{Ni}_{80}\text{Fe}_{20}$ permalloy (J_s = 1.0 T, A = 1.3×10^{-11} J/m, K_1 = 0.0 J/m^3) (*Skomski and Coey*, 1999) and a damping constant α of 0.25 to improve convergence.

We perform simulations on cones where the overall diameter d of the base ranges from 10nm to 100nm, the height h between the base and the tip ranges from 10nm to 100nm and the external magnetic field is applied along the x direction of the cone (see figure 4.1).

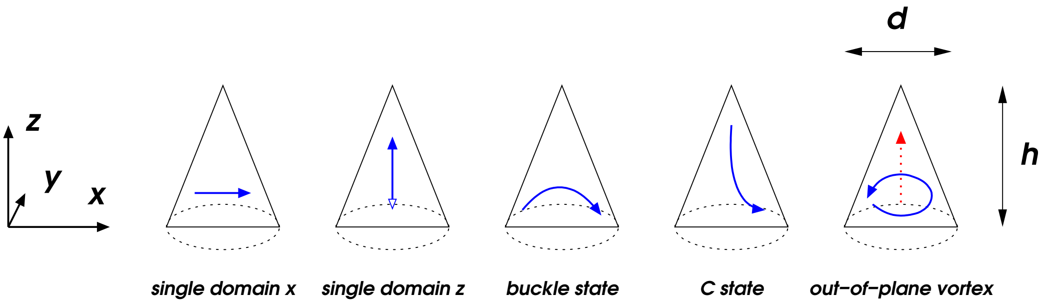

Figure 4.1: Representation of remanent magnetisation states; the solid arrows indicate the magnetisation direction, the dotted arrow shows the vortex core direction. From left to right: single domain state in x, single domain state in $+z$ (filled arrow) and $-z$ (hollow arrow), buckle state (*Koltsov et al.*, 2000), C state and out-of-plane vortex state.

The mesh for the *magpar* hybrid FE/BE simulation is created using *NETGEN* (*Schöberl*, 2003). For the cone where $d = 100\text{nm}$ and $h = 100\text{nm}$, the mesh contains 210825 tetrahedra, with the largest element having an edge length smaller than 4nm, which is below (*Donahue and McMichael*, 1997) the calculated exchange length $\lambda_{\text{ex}} = \sqrt{2A/\mu_0 M_s^2}$ (*Kronmüller and Fähnle*, 2003) of 5.71nm.

The remanent magnetisation configurations using *OOMMF* and *magpar* are in agreement providing the shape is sufficiently well resolved in both cases. To ensure this is the case with *OOMMF*, the cones were discretised into 8000 cells, in the largest case the cell edge length is 5nm with a maximum adjacent cell spin angle of 0.5 radians.

Starting from an initially uniform magnetisation state pointing in the $+x$ direction, we apply a magnetic field of 500mT capable of maintaining a nearly homogeneous magnetisation and reduce this field in steps of 1mT until the magnetisation is reversed to compute the hysteresis loop. When the applied field is reduced to zero, we classify the magnetisation pattern to create the remanence phase diagram. Figure 4.1 shows schematic plots of the observed remanent states.

4.3 Results

Figure 4.2 shows the phase diagram for the remanent magnetisation states in cones where $10\text{nm} \leq d \leq 100\text{nm}$ and $10\text{nm} \leq h \leq 100\text{nm}$ and the applied field was originally in the $+x$ direction (see figure 4.1). Where h is less than 20nm, the remanent state is a single domain state with the magnetisation pointing in the x direction (figure 4.1, left). If h is above 50nm and the ratio h/d is high (*i.e.* a tall, thin cone) then the single domain state in z is preferable due to shape anisotropy (figure 4.1, second from left). We have observed two types of single domain states in z: one with the magnetisation pointing up towards the tip of the cone and the other with the magnetisation pointing down towards the base. The single domain states in x

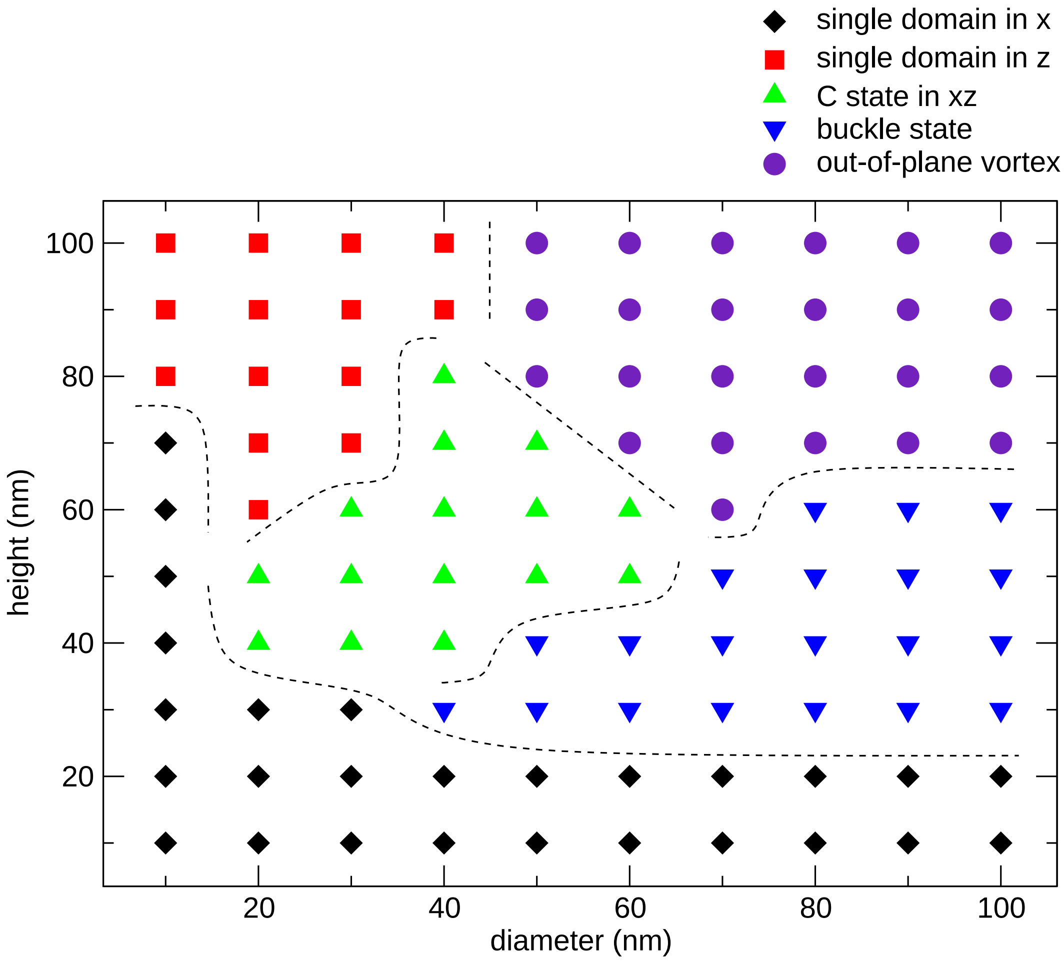

Figure 4.2: Phase diagram of the remanent magnetisation states for cones where the applied field was originally in the $+x$ direction. The symbols represent computed points, dashed lines are guides to the eye.

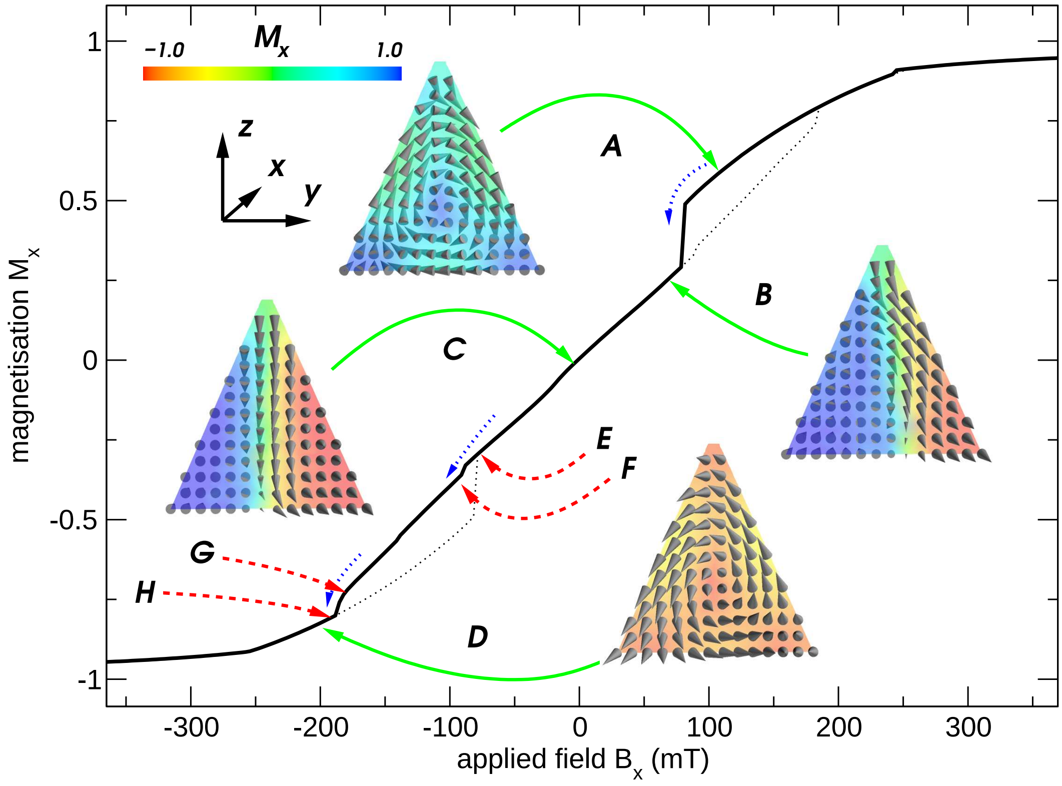

Figure 4.3: Hysteresis loop and reversal mechanism for a cone where $d = h$ =100nm and the applied field is across the diameter. Points E, F, G and H are explained in figure 4.4.

and z are in agreement with experimental data in *Ross et al.* (2001).

For larger h and d the demagnetising energy grows and the remanent state is the vortex state with the magnetisation in the core of the vortex pointing out of the xy plane (figure 4.1, right).

For intermediate values of h we find at large d the buckle state (figure 4.1, centre), in which the overall magnetisation points in x but around the centre of the xy plane this bends slightly upwards and downwards in z. The buckling is an indication of the growing dipolar energy of the single-domain state.

At smaller d for intermediate h the remanent state is a C-shaped configuration (figure 4.1, second from right). The C state is related to the single domain state in z by the shape anisotropy driving the magnetisation to point primarily in the -z direction. In larger diameters the magnetisation will attempt to reduce the demagnetisation energy — the bending of the magnetisation in the $+x$ direction close to the base of the cone shows the history of the system: prior to the field being reduced to zero the magnetisation was pointing in the $+x$ direction.

Figure 4.3 shows the complete hysteresis loop for a cone with d=h=100nm, computed using *magpar*. When the applied field is reduced from saturating the magnetisation in the $+x$ direction, it forms an in-plane vortex (*i.e.* where the magnetisation circulates in yz and the vortex core points in the x direction) shown at point A. The same behaviour is observed for the magnetisation reversal of spheres (*Boardman et al.*, 2005b, *Eisenstein and Aharoni*, 1975) of similar size. Note that this configuration is not observed in the absence of an applied field and therefore this state is not shown in figure 4.1.

The in-plane vortex is replaced by an out-of-plane vortex (*i.e.* where the magnetisation circulates in xy and the vortex core points in the z direction) shown at point B after overcoming an energy barrier. The core of this vortex is anchored at the tip of the cone and compensates for the applied field by tilting the core, allowing the majority of the magnetisation to align with the applied field, thus minimising Zeeman energy.

A further reduction of the field (point C) causes the core of the vortex to shift to the centre of the cone. Reducing the field below zero causes the vortex to bend in the opposite direction to point B. At $B_{\mathrm{x}} = 0\mathrm{mT}$ the magnetisation is in the vortex state as shown in figure 4.1 (right). Another energy barrier needs to be overcome to destroy the out-of-plane vortex, leaving the magnetisation with an in-plane vortex (point D) with the core pointing in the opposite direction to the vortex at point A.

Once the field is sufficiently high the in-plane vortex aligns into a homogeneous saturated magnetisation in the -x direction for $|B_{\mathrm{x}}| \geq 250\mathrm{mT}$.

Figure 4.4 shows specifically the magnetisation at points E, F, G and H from figure 4.3 to explain the subtle “kinks” in the hysteresis loop. The top row shows a magnetisation cross section along the height of the cone and the bottom row that along the base. The middle row is a schematic representation of the two vortices corresponding to the cross sections above and below.

Starting at point E, the system contains two vortices: the out-of-plane vortex with the core pointing in the +z direction introduced at point B, and the formation of an in-plane vortex with the core in the -x direction parallel to the applied field. Increasing the field in the -x direction causes the in-plane vortex to become more dominant (point F). A further increase of the applied field in the -x direction allows the in-plane vortex to become even more influential, moving the out-of-plane vortex to the edge of the sample (point G). There is a small energy barrier present to force the out-of-plane vortex from the system; once this has been overcome only the in-plane vortex remains (point H).

4.4 Summary

We have simulated the magnetisation reversal in conical samples, and five separate remanent states — single-domain in x, single-domain in z, out-of-plane vortex, buckle and C-state — have been observed.

By analysing the remanent magnetisation configuration for a series of simulations, we have created a phase diagram showing these results. The dynamics of the

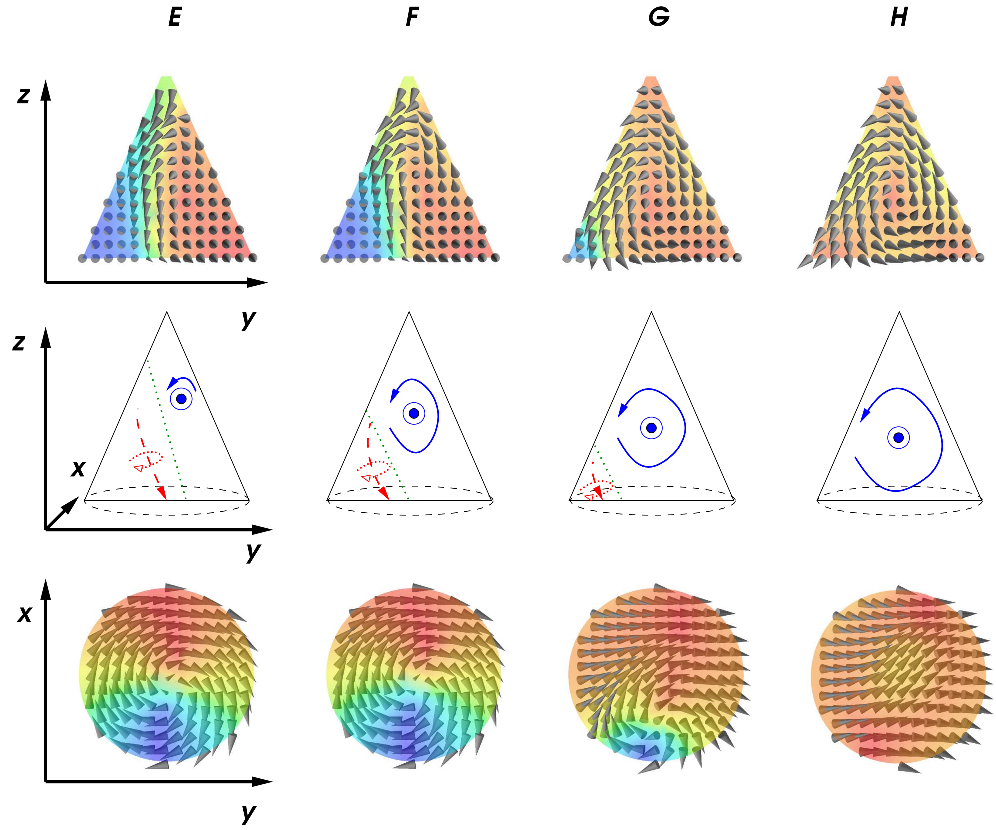

Figure 4.4: Reversal mechanism detail for points E, F, G and H in figure 4.3. Top: yz cutplanes of magnetisation shaded by the x component of the magnetisation (M_x). Middle: schematics indicating vortex behaviour (solid arrows for the in-plane vortex shown the in top row, dashed arrows for the out-of-plane vortex shown in the bottom row). Bottom: xy cutplanes of the magnetisation at the base of the cone.

magnetisation reversal are more complicated to classify and describe.

We have investigated and presented in more detail the magnetisation reversal of larger cones (height greater than 70nm and diameter greater than 50nm) and find that for parts of the hysteresis loop, two coexisting vortices can be found in the magnetisation (with cores pointing in approximately perpendicular directions).

Chapter 5

Nanodots

The work described in this chapter has been published in two papers in the Journal of Applied Physics (*Boardman et al.*, 2004, 2005b).

5.1 Introduction

Figure 5.1 shows an array of nanodots created using the novel "double template" method imaged using a scanning electron microscope.

Figure 5.2 shows the experimentally measured hysteresis loop for such an array of nickel nanodots (see section 5.1.1) with a bounding sphere diameter d of 500nm (*Zhukov*, 2004) obtained through magneto-optical Kerr effect (*Argyres*, 1955) microscopy. The motivation here is to reveal the physics in this hysteresis loop through micromagnetic simulation.

Although the precise shape of the nanodot is not known, we do know the manufacturing method (see section 5.1.3) and from this we can derive an approximate representation of the nanodot.

It is not feasible to perform a three-dimensional micromagnetic simulation of a large array of nanodots so instead a single nanodot is modelled numerically. Despite some inevitable dipolar interaction in the real system, particularly when the nanodots are close together, it remains of interest to investigate the magnetisation of an independent nanodot.

5.1.1 What is a nanodot?

We define a nanodot to be a magnetic sample with a physical edge size l_x of less than 1μm and "short" in geometry, *i.e.* $l_z \leq 0.5 l_x$. Arrays of nanodots are strong candidates for use in patterned media, as the consistency of shape from one nanodot to the next promotes predictable behaviour; one nanodot will behave in the same way to another nanodot, in contrast to irregular grains where clusters of grains are required to reduce the effects of this irregularity.

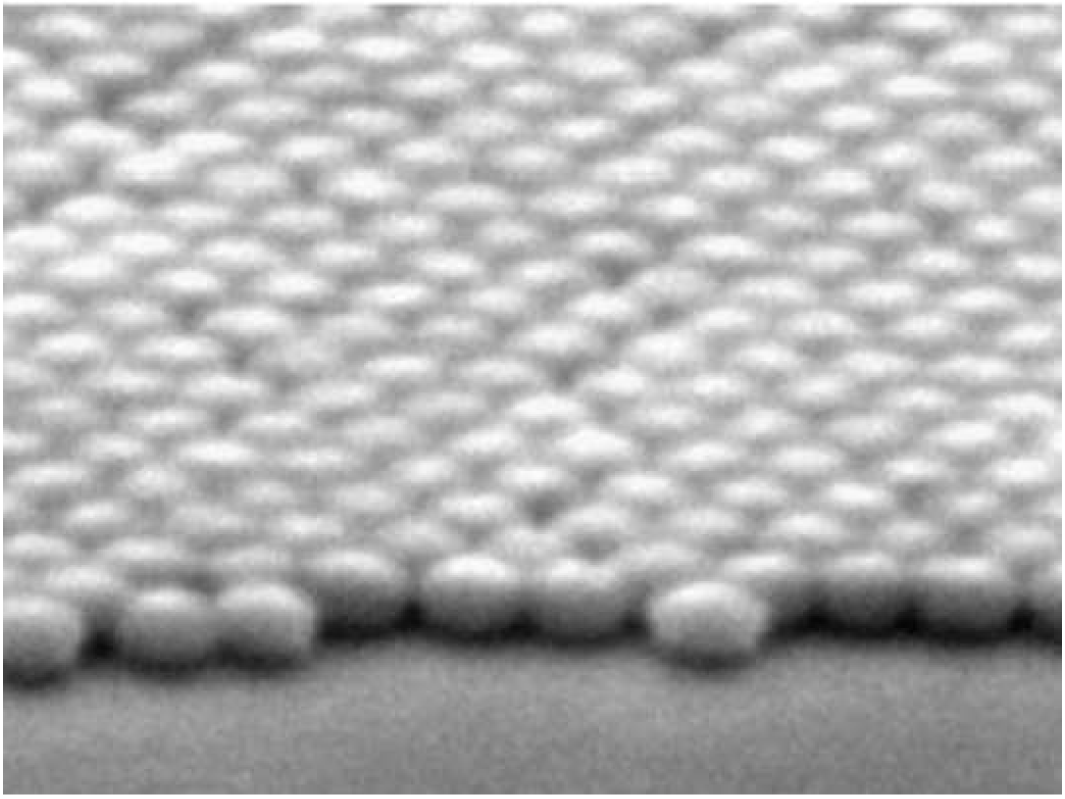

Figure 5.1: Scanning electron microscope image of a droplet array

5.1.2 Lithography

There are several different ways of creating nanodots. Lithographic methods such as those used by *Cowburn et al.* (1999a), *Li et al.* (2002) and discussed in chapter 3, although successful, are limited in the grain size they can produce; in photolithography the wavelength of light used in the fabrication process effectively limits the dot size to those above 0.4μm, and electron beam lithography is still a prohibitively expensive process.

5.1.3 Self-assembly

Self-assembly methods (*Denkov et al.*, 1993) appear to be a cost-effective way to create templates, from which an array of structures as shown in figure 5.1 can be formed (*Ghanem et al.*, 2004, *Zhukov et al.*, 2003). These structures are the motivation behind this chapter. One particular method of chemical self-assembly involves the formation of templates through the evaporation of an aqueous suspension of polystyrene latex spheres (*Bartlett et al.*, 2002, 2003a), initiating the self-assembly. Figure 5.3 shows this process schematically.

Using these templates, it is possible to create magnetic structures from sizes of 50nm to 1000nm by filling the spaces between the close-packed spheres with some

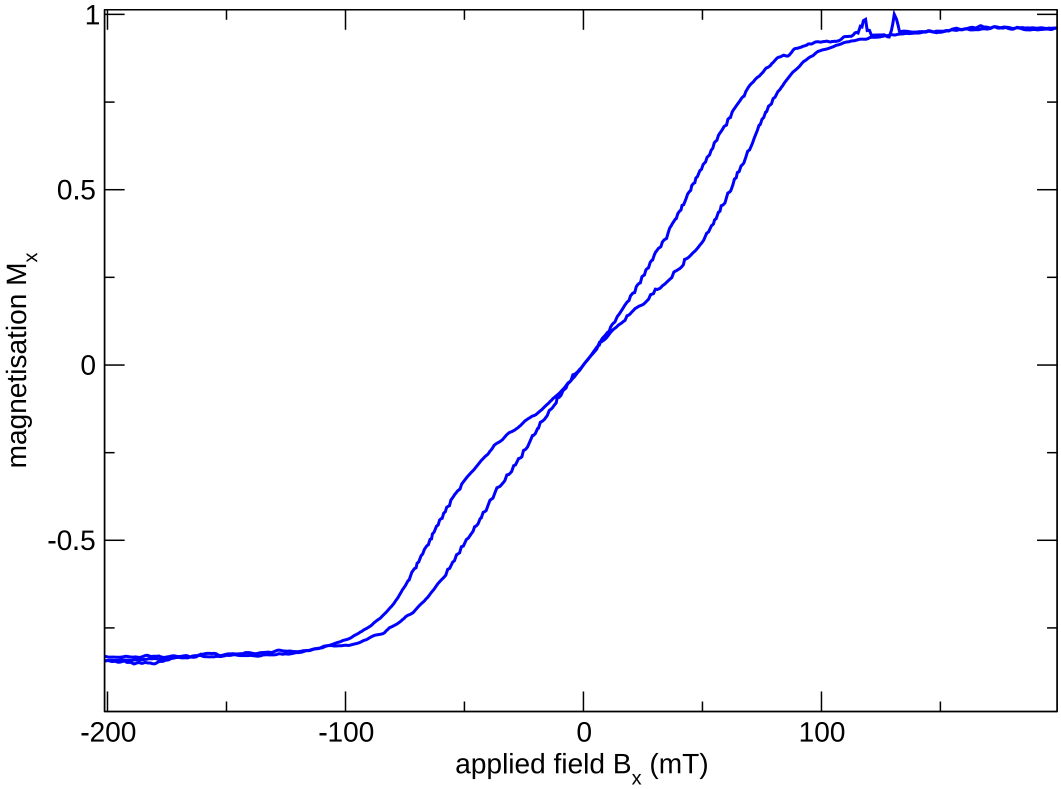

Figure 5.2: Normalised MOKE measurements for a nickel dot array of diameter 500nm

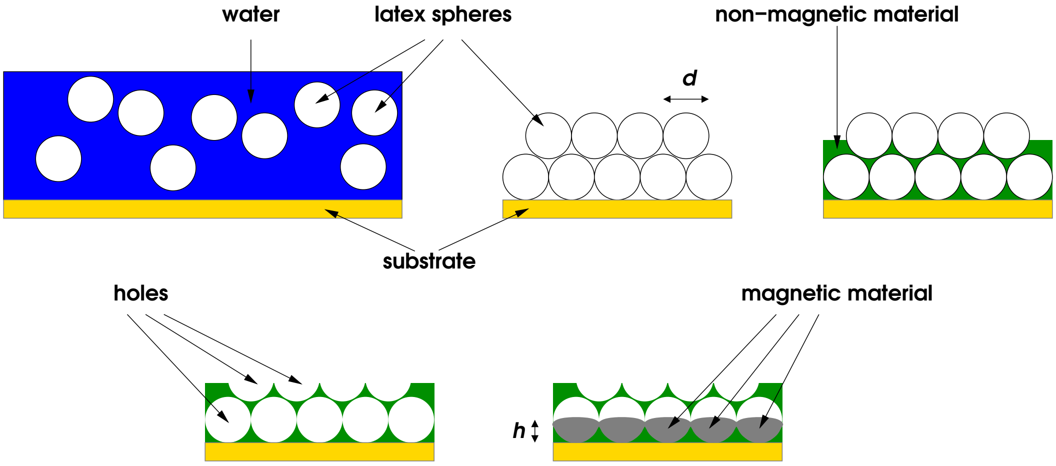

Figure 5.3: The double-template self-assembly technique. First, an aqueous suspension of latex spheres (top left) of diameter d is poured onto a substrate. As the water evaporates, the latex spheres are attracted to each other (top centre), forming a regular close-packed structure. This template can be filled with a non-magnetic material (top right) and the latex spheres etched away (bottom left). The resulting gaps can be filled with a magnetic material to a varying height h (bottom right) to form arrays of connected or disconnected part-spherical nanodots.

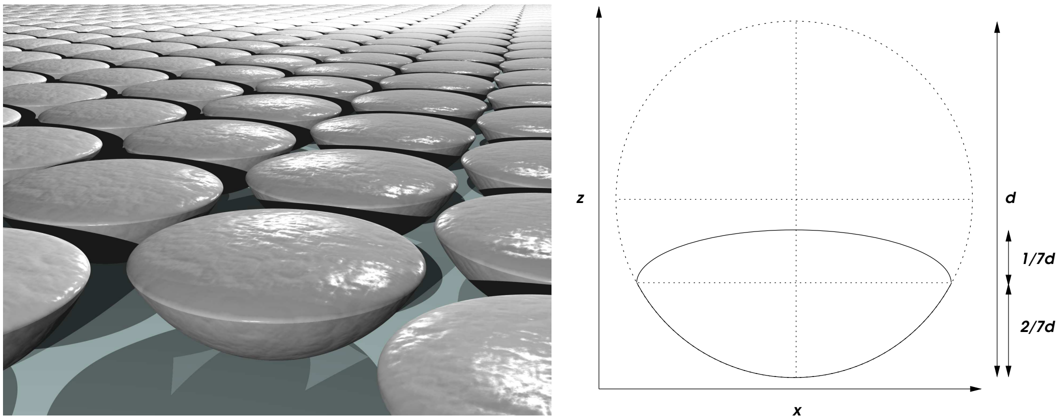

Figure 5.4: A typical nanodot "droplet" geometry arranged in a hexagonal lattice (artist's impression on the left) and a schematic of the droplet (right)

material through electrochemical deposition. By etching away the polystyrene spheres, another template is formed. This template can then be filled with magnetic material, and by varying the fill amount of the resulting spherical holes, connected or disconnected arrays of dots can be formed. This is known as the double-template self-assembly method.

The resulting structures have several applications, such as photonic materials (*Bogomolov et al.*, 1997, *Vlasov et al.*, 2001), microchip reactors (*Gau et al.*, 1999) and biosensors (*Velev and Kaler*, 1999). The application in which we are interested for this work pertains to magnetism.

We present here the results for two types of nanodot geometry — part-sphere and "droplet". The droplet geometry can be considered to be a part-sphere with a rounded upper; this is described in more detail in section 5.5.

5.2 Half-sphere

We wish to simulate a half-sphere so we can see what effect the rounded upper dome (which can be seen in figure 5.1) has on the results; these can then be compared to "droplet" systems (section 5.5) which reflect the shape in figure 5.1. The half-sphere nanodot we simulate here is isotropic nickel ($M_s = 493380$ A/m, $A = 8.5 \times 10^{-12}$ J/m, $K_1 = 0$ J), with a diameter of 200nm. We use *OOMMF* to simulate this geometry with a finite difference cubic cell of edge length 5nm.

5.2.1 Results

Applying a sufficiently large magnetic field across the circular plane of a half-sphere results in an initially homogeneous magnetisation pattern, and as with the sphere in section 3.5, a slight deviation at the surface resulting from the demagnetising field. This corresponds to point a in figure 5.5; the homogeneous magnetisation

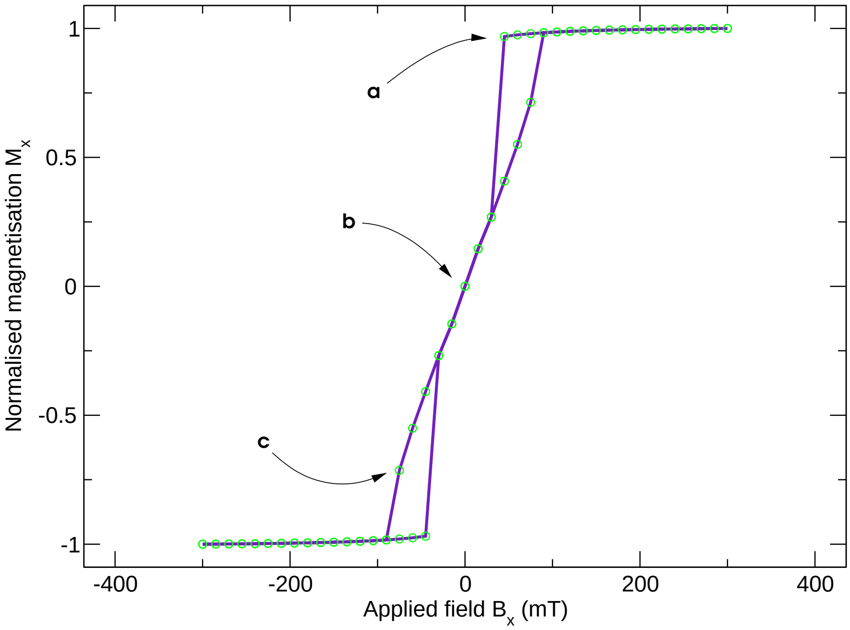

Figure 5.5: Hysteresis loop for a nickel half-sphere of diameter 200nm

is illustrated in figure 5.6.

Reducing the field further causes the nucleation of a vortex at around 30mT, resulting in the magnetisation drop immediately following point a in figure 5.5.

The vortex core moves in the $-y$ direction while the field is reduced further (point c in figure 5.5; illustrated in figure 5.8), until the vortex leaves the system and a homogeneous magnetisation in the $-x$ direction is established.

5.2.2 Discussion

Although hysteretically this exhibits a qualitative similarity with the sphere (figure 3.11) insofar as their possession of two minor loops, the magnetic microstructure is more reminiscent of the flat cylinder in that the vortex nucleates out of the plane and moves through the geometry in the same fashion as the flat cylinder (figures 3.3 to 3.8), however the vortex appears *prior* to the applied field being reduced below zero.

Figure 5.7 illustrates that at zero field the direction of the vortex core is perpendicular to and in the centre of the xy plane; see point b in figure 5.5. For isolated half-spheres we always find the magnetisation in the core of the vortex to point "down" (*i.e.* towards the spherical surface). We attribute this to the asymmetry of the half-sphere in the z direction.

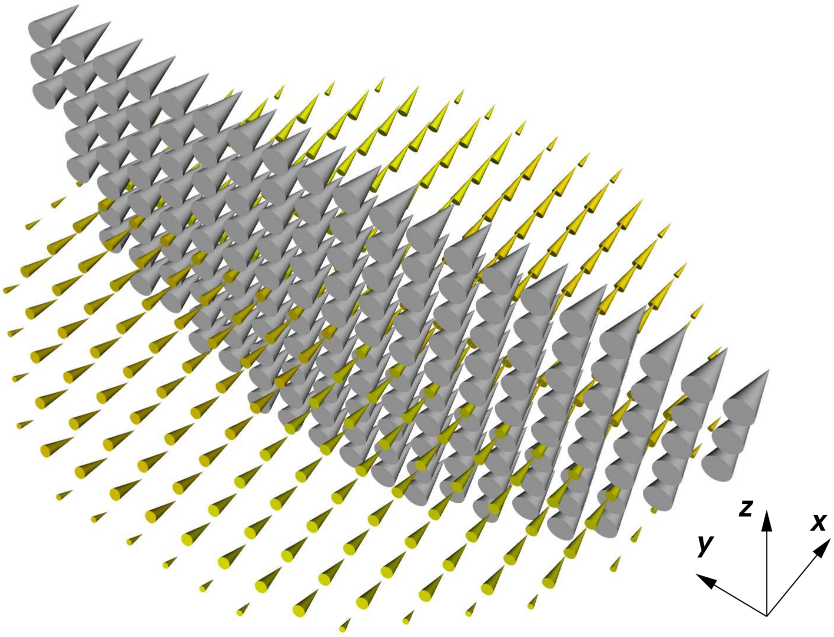

Figure 5.6: Half-sphere at high applied field (point a in figure 5.5)

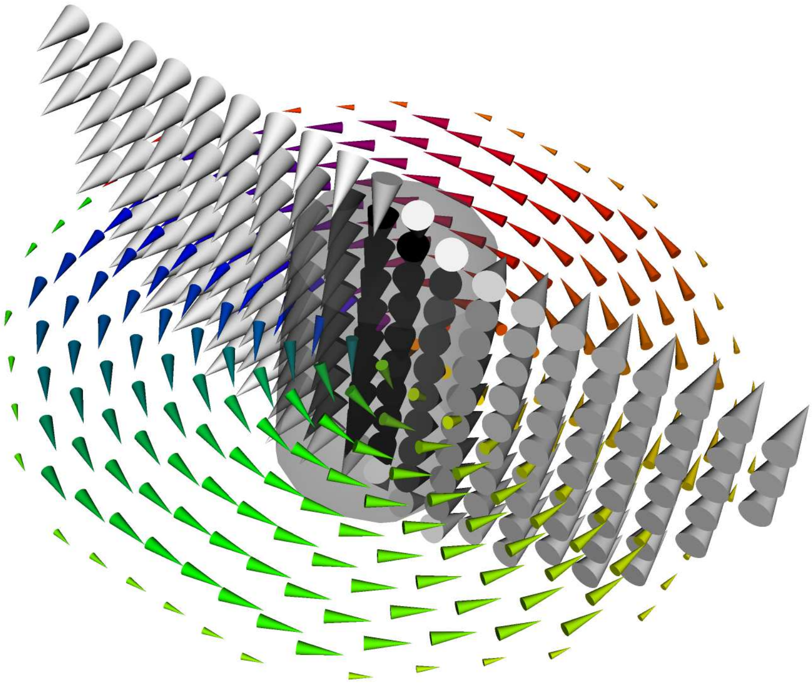

Figure 5.7: Half-sphere in vortex state in zero applied field (point b in figure 5.5). Axes are the same as those in figure 5.6

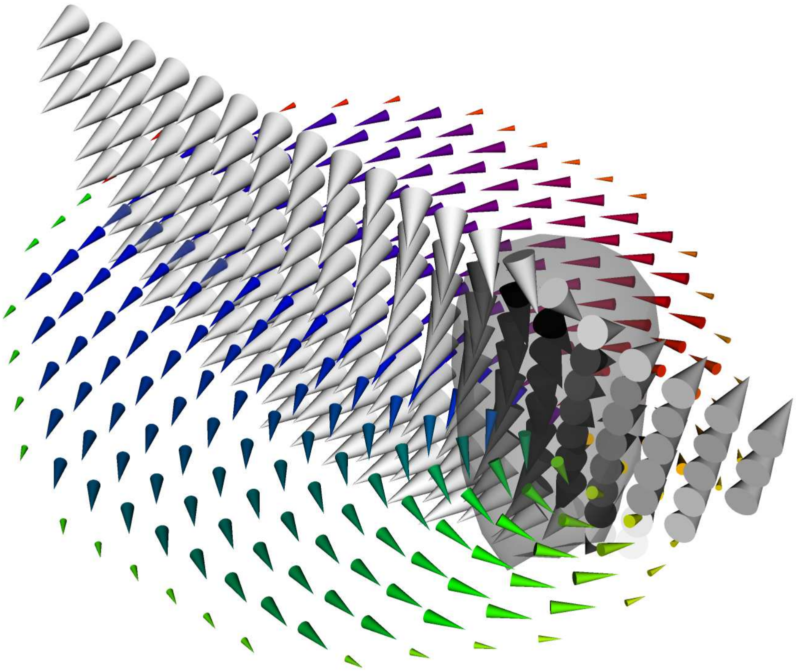

Figure 5.8: Half-sphere in late vortex state (point c in figure 5.5). Axes are the same as those in figure 5.6

5.3 Part-spherical nanodots

We have seen above that the magnetisation reversal in the half-sphere occurs via vortex nucleation similar to the mechanism in the flat cylinder shown in section 3.4. We have shown in section 3.5 that a full sphere reverses via a different mechanism. From this it can be concluded that for some height $h > d/2$ of a part-sphere a transition between the two reversal mechanisms takes place.

These results are also relevant to the experimentally manufactured nanodots because the amount of material that is deposited through the self-assembly method described in section 5.1.3 can be varied to grow spheres of heights $h \leq d$.

We calculate numerically the magnetisation reversal of soft part-spherical particles. The observed reversal mechanisms range from single domain reversal at small radii, to vortex movement in shallow systems at larger radii and vortex core reversal at larger heights as observed in spheres.

In this section we study the behaviour of the new class of part-spherical structures and compute a magnetic reversal phase diagram as a function of diameter and height.

5.3.1 Parameters

Geometrically we consider the part-spheres to have one flat surface when $h < d$; in the case $h = 0.5d$ the geometry will resemble the half-sphere from section 5.2.

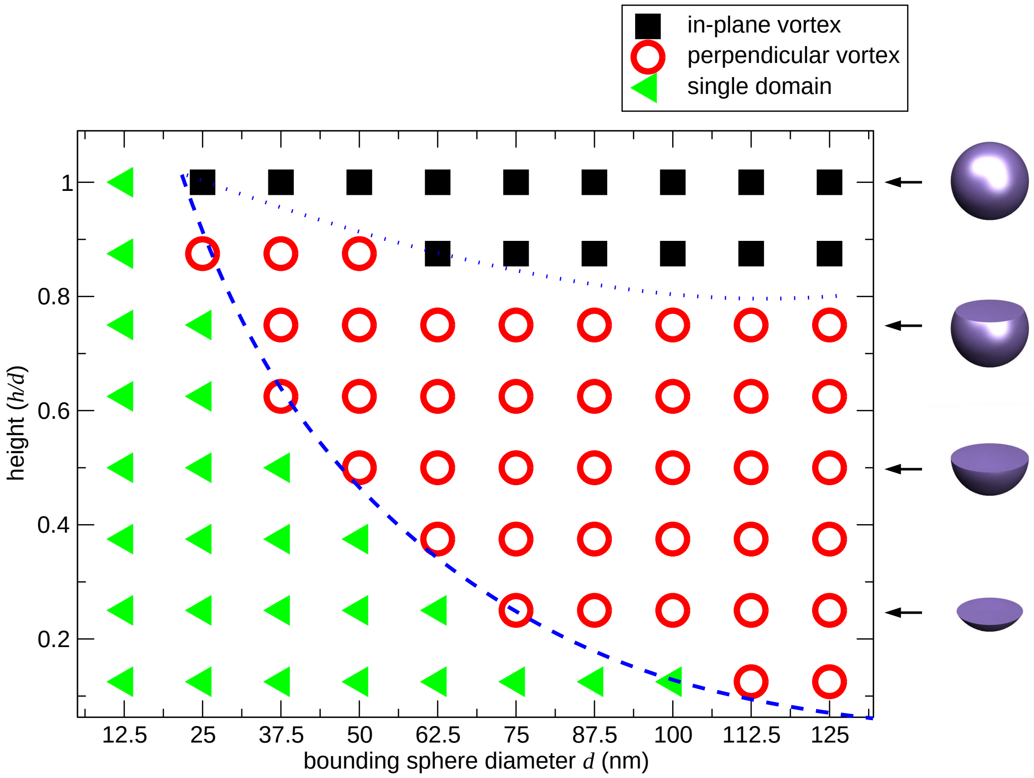

Figure 5.9: Phase diagram of reversal mechanisms for $Ni_{50}Fe_{50}$ permalloy part-spheres. The dotted and dashed lines are guides to the eye indicating reversal mechanism boundaries

We perform the phase diagram studies using the material parameters for $Ni_{50}Fe_{50}$ permalloy (M_s = 1.11×10^6 A/m, A = 5.85×10^{-12} J/m, $K1$ = 0 J/m^3, see also appendix C) and a damping constant α of 0.25 to improve convergence.

5.3.2 Results

Figure 5.9 shows a phase diagram of remanent magnetisation states for systems simulated with *magpar* where the height h increases from $1/8d$ to d in $1/8d$ steps and d varies between 12.5nm and 125nm.

We observe three distinct reversal mechanisms. Taking d=50nm, for $h/d \leq 0.375$ the reversal is coherent; all the magnetic moments remain aligned and rotate homogeneously. Between $h/d = 0.5$ and $h/d = 0.875$ an out-of-plane vortex forms with a core perpendicular to the applied field after some initial energy barrier is overcome and this can freely move around the inside of the part-sphere with the applied field. This is similar to the behaviour seen in cylindrical particles shown in figures 3.3 to 3.8 and in other works (*Boardman et al.*, 2004, *Cowburn et al.*, 1999b, *Ha et al.*, 2003, *Li et al.*, 2002). We will now discuss the reversal mechanism in more detail.

Figure 5.10 shows the perpendicular vortex reversal behaviour. Point A shows the homogeneously aligned state at high applied field, though there is a small C-

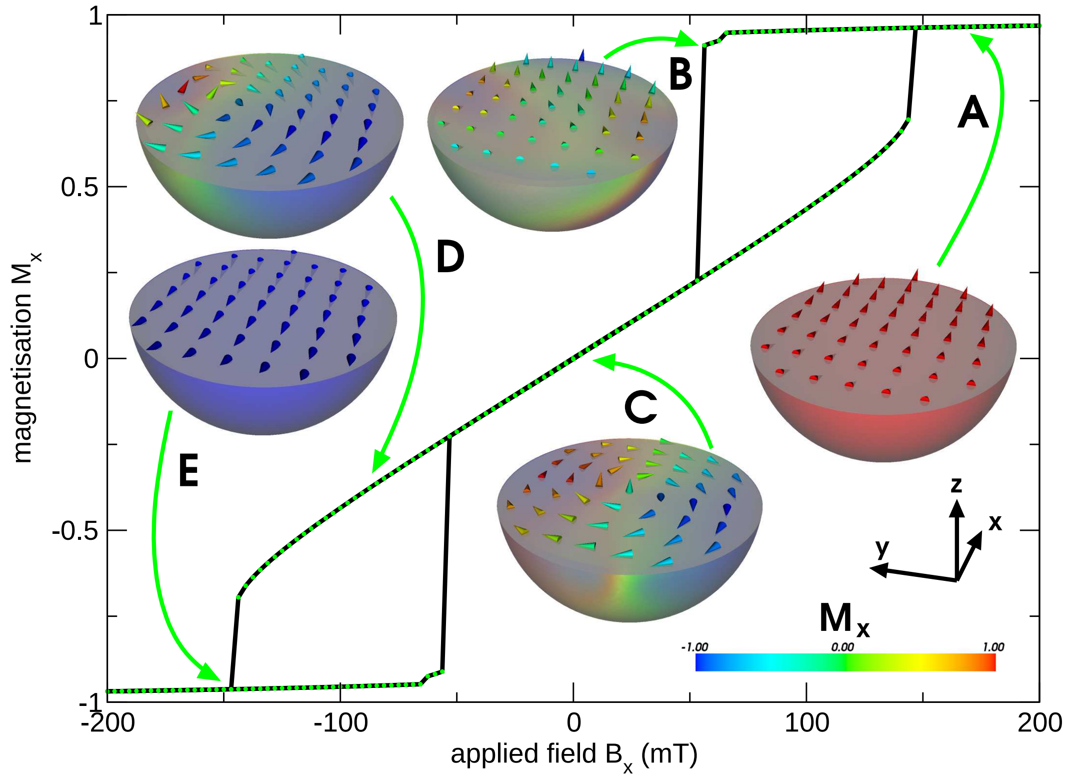

Figure 5.10: Reversal mechanism for d=50nm, h=0.5d

state-like shift in the x-z direction at the extremities in order to minimise dipolar energy. At point B there is a shift into an S-like state in the x-y direction, where the magnetic moments at the edges of the half-sphere persist in the applied field direction while the moments towards the centre are aligned a few degrees away from the x direction into the y direction. Reducing the field further overcomes an energy barrier and a perpendicular (*i.e.* the core of the vortex points in the z direction) vortex is formed. Point C shows the remanent state of the half-sphere with this vortex in the centre; the net magnetisation in the x direction is now zero. Point D shows the effects of a continued field reduction; the vortex has shifted further into the y direction appropriate for allowing the majority of the magnetic moments to point in the negative x direction. Finally, at point E the external field is now sufficiently low to remove the vortex from the system, and a homogeneously aligned state remains.

Figure 5.11 shows the reversal mechanism with an in-plane vortex for a sphere (*i.e.* $h/d = 1.0$). Although the size and material differ from the sphere in section 3.5, there is a qualitative similarity we will review. Point A shows a homogeneous alignment of the magnetic moments in the x direction, which persists until point B, where the field has been lowered enough to overcome the energy barrier and allow an in-plane (*i.e.* where the core points in the x direction) vortex to form; this also allows the majority of the magnetisation to continue pointing in the x direction.

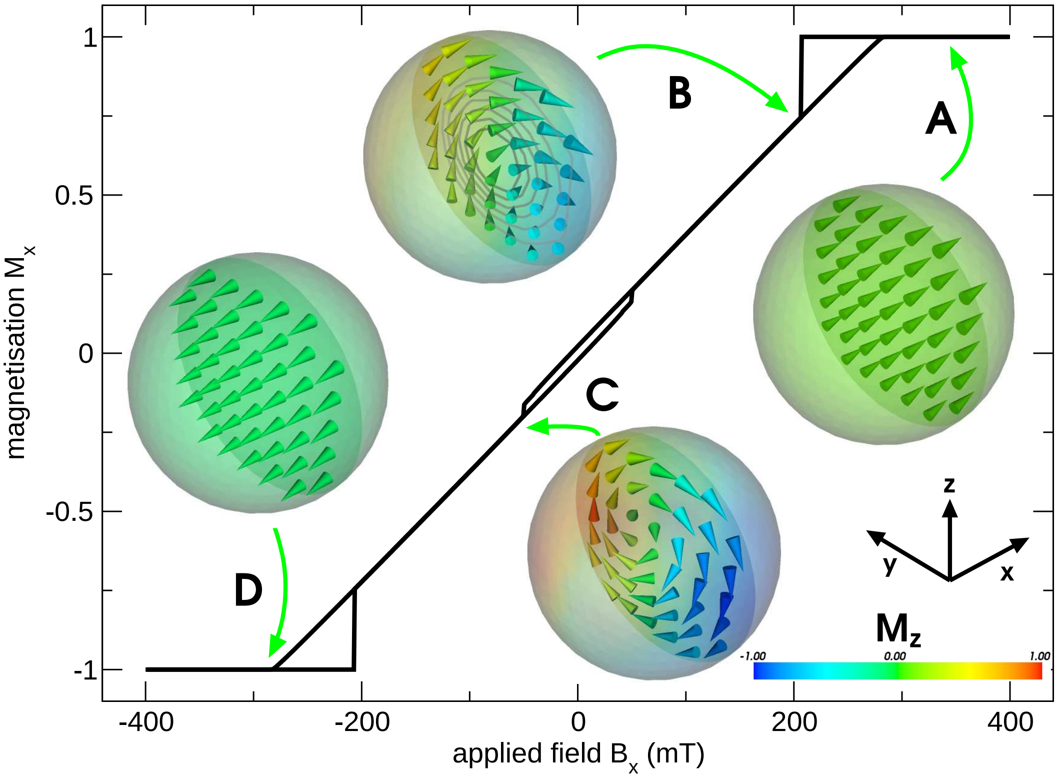

Figure 5.11: Reversal mechanism for d=100nm, h=d

As the field is further reduced, the x component of the magnetisation outside the vortex core continues to follow the applied field; however the core remains pointing wholly in the direction of the initial applied field. At point C, after the field is reduced below zero the core of the vortex flips over, which is responsible for the "minor" hysteresis loop around $B_\mathrm{x} = 0$. The vortex can exit the system when the field is further reduced and the magnetisation becomes homogeneous (point D).

Our simulation results agree with the computation of the critical radius (*O'Handley*, 1999, p305) of single-domain to vortex state transition (equation 3.1) for $\mathrm{Ni_{50}Fe_{50}}$ permalloy in spheres of radius 12.4nm (d=24.8nm): a single-domain remanent state is observed in our simulations of spheres of diameter 24nm and below where the exchange energy is dominant, whilst an in-plane vortex is in the remanent state when the diameter is 25nm or greater as the dipolar energy becomes preponderant.

5.3.3 Comparing *OOMMF* and *magpar*

Figure 5.12 shows results computed during the simulation of a half-sphere of diameter 50nm using two different simulation packages that employ the finite difference method (*Donahue and Porter*, 1999) and the hybrid finite element/boundary element method (*Scholz et al.*, 2003a) respectively. There is good agreement between the two

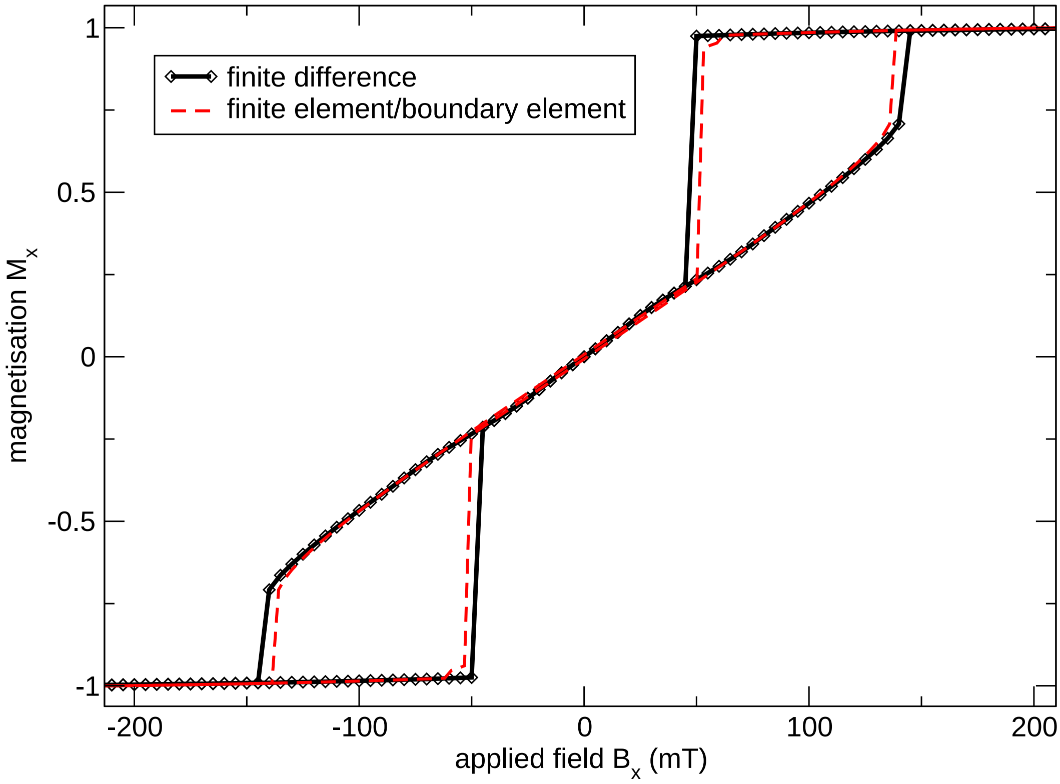

Figure 5.12: Hysteresis loops for a *d*=50nm half-sphere obtained with (solid line) *OOMMF* (finite difference method) and (dashed line) *magpar* (finite element/boundary element method) packages.

The results obtained from both *OOMMF* (FD method) and *magpar* (hybrid FE/BE method) display an energy barrier which is overcome when B_x is below 50mT. Additionally, reversible behaviour around $B_x = 0$ is present in both cases.

The slight aberration in the hysteresis loop for the hybrid FE/BE case is caused by a slight shift in the magnetisation towards the centre of the sample (figure 5.10, point B), present in the simulation as a result of the improved shape resolution over the FD case.

5.4 Multiple vortex states

As the diameter of a part-spherical geometry is increased, further characteristics are observed which resemble those of the full sphere.

Figure 5.13 shows the hysteresis loop for an isotropic nickel half-sphere of diameter 350nm. This hysteresis loop shares some similarity with that of a smaller half-spherical system, such as that in figure 5.10 — it has zero remanence and there are openings in the hysteresis loop. The characteristic difference between the two loops is there are two energy barriers: the first occurs when B_x is around 100mT, followed by another when B_x is approximately 70mT, corresponding to the kink in

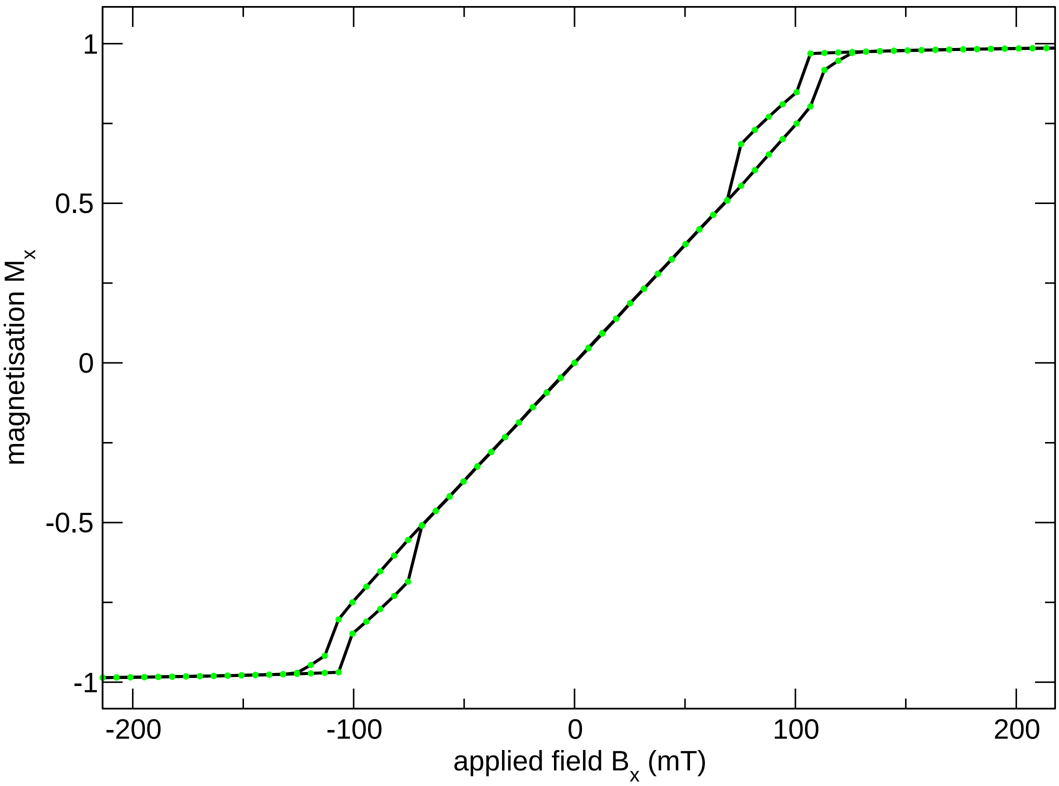

Figure 5.13: Hysteresis loop for an isotropic nickel half-sphere of diameter 350nm. Two energy barriers can be seen: one at ≈100mT and another at ≈70mT. The first indicates the transition from the single-domain state to the in-plane vortex state, the second the transition from the in-plane vortex state to the perpendicular vortex state.

the curve at 60mT in figure 5.10.

Figure 5.14 reveals the magnetic microstructures in this model. The image on the left shows the magnetisation when B_x is 80mT. An in-plane vortex has formed and the magnetisation circulates in the yz plane, with the core of the vortex pointing in the x direction with the applied field. The image on the right shows the magnetisation after B_x has been reduced to 65mT. The in-plane vortex has been replaced by a perpendicular vortex: the magnetisation now circulates in the xy plane with the core of the vortex pointing in the z direction. The core of the vortex is off-centre to allow the majority of the magnetisation to point in the direction of the applied field.

Figure 5.15 shows the hysteresis loop when the diameter of the nickel half-sphere is increased to 750nm. Qualitatively, the same behaviour is observed as when the half-sphere diameter is 350nm. Point A shows the fully-saturated magnetisation at a high applied field in the $+x$ direction. When this is reduced to overcome the first energy barrier (point B) then the in-plane vortex forms, with the core of the vortex pointing in the direction of the applied field. As the field is reduced to immediately prior to the second energy barrier at around 75mT (point C), the magnetisation around the core of the vortex deviates further away from the x direction

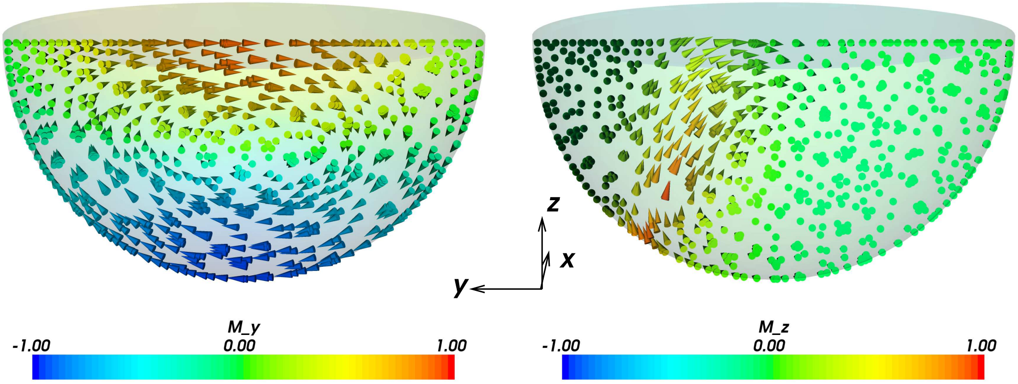

Figure 5.14: Two vortex states in an isotropic nickel half-sphere of diameter 350nm. The images show vector cut-planes of magnetisation in the y-z direction — applied field was in the x direction. The in-plane vortex (left) is clearly visible at B_x ≈80mT. The perpendicular vortex (right) is in a field of ≈65mT, and is off-centre to compensate for the applied field.

to minimise dipolar energy.

Point D shows the magnetisation immediately after the second energy barrier has been overcome. The in-plane vortex has disappeared to be replaced by a perpendicular vortex, with the core pointing in the z direction. The majority of the magnetisation remains in the direction of the applied field. Reducing the field to zero (point E) sees the vortex core move across the sample in the y direction, causing the average M_x to be zero. Increasing the applied field in the opposite direction ($-x$) causes the vortex core to move further along the y direction (point F) allowing the majority of the magnetisation to point in the $-x$ direction, similar to point D.

Increasing the field further in the $-x$ direction overcomes another energy barrier present around -125mT (point G), causing the perpendicular vortex to disappear and an in-plane vortex with the core pointing in $-x$ to form, which disappears when the applied field is increased to -140mT (point H).

5.5 “Droplet” nanodots

5.5.1 Parameters

In this instance, the geometry of the nanodot is similar to that of a “droplet”; we consider the shape to be split into two parts — the lower part follows a “bounding sphere” to some fraction, at which point it is cut off to form a part-sphere. This is then provided with an ellipsoidal top, giving the geometry a dome-topped appearance, which can be seen more clearly in figure 5.4, in order to approximate the experimentally grown droplets (figure 5.1) as well as possible..

For these simulations, we define the height of the geometry thus (as figure 5.4,

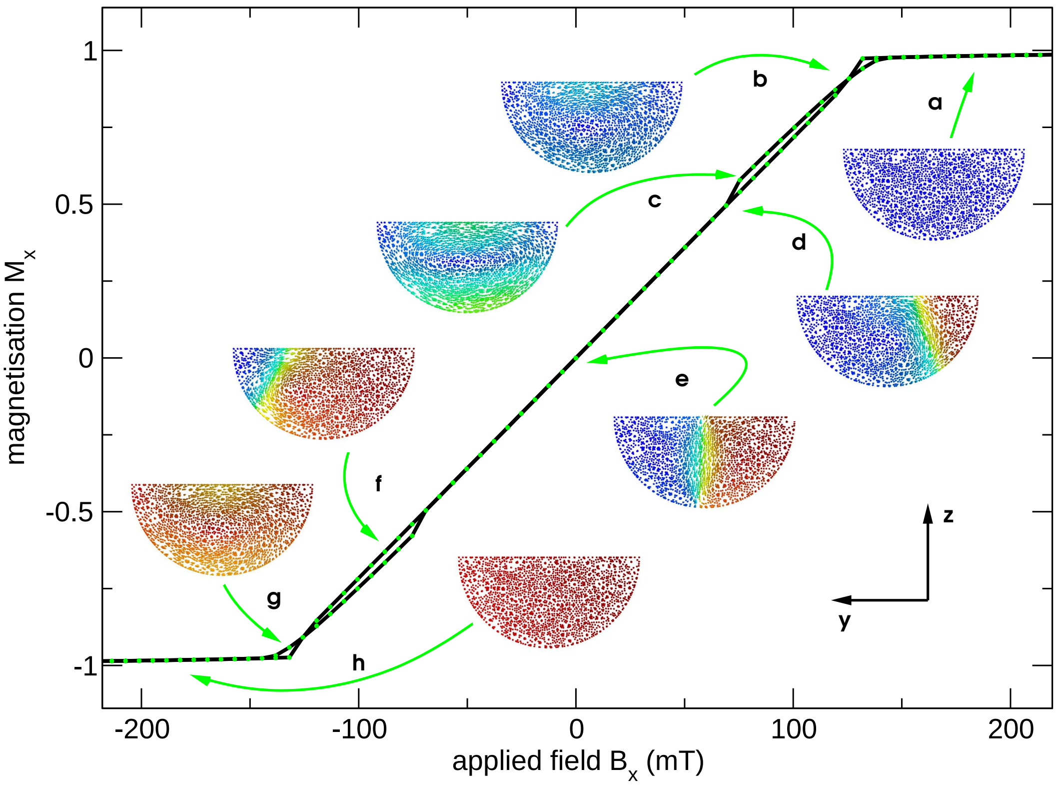

Figure 5.15: Hysteresis loop for isotropic nickel half-sphere of diameter 750nm simulated with *magpar*. The coloured sections of the smaller images represent the magnetisation in the x direction

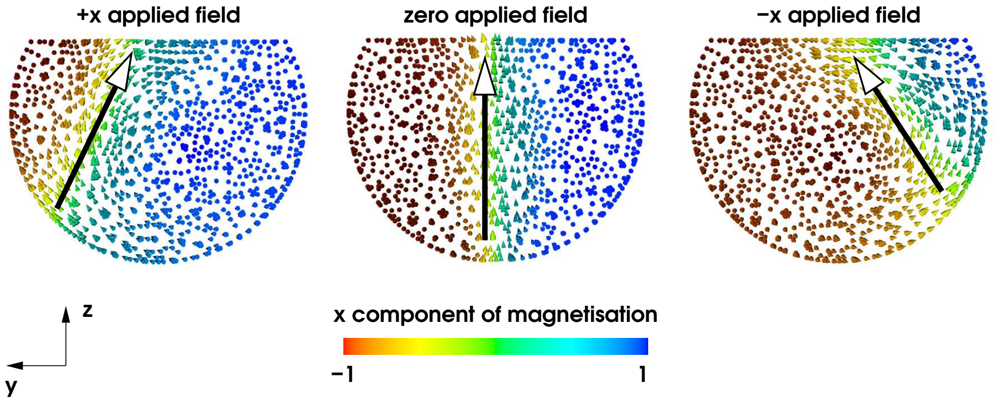

Figure 5.16: Vortex "pinning" in a part-sphere of height $0.75d$. After entering an in-plane vortex state (left), the upper part of the vortex core is situated about the centre of the xy plane while the lower part is towards $+y$. When the field is reduced to zero (centre), the upper and lower parts of the vortex core are around the centre of the xy plane. If a negative field is then applied (right), then the lower part of the vortex core moves towards $-y$, but the upper part remains at the centre of xy.

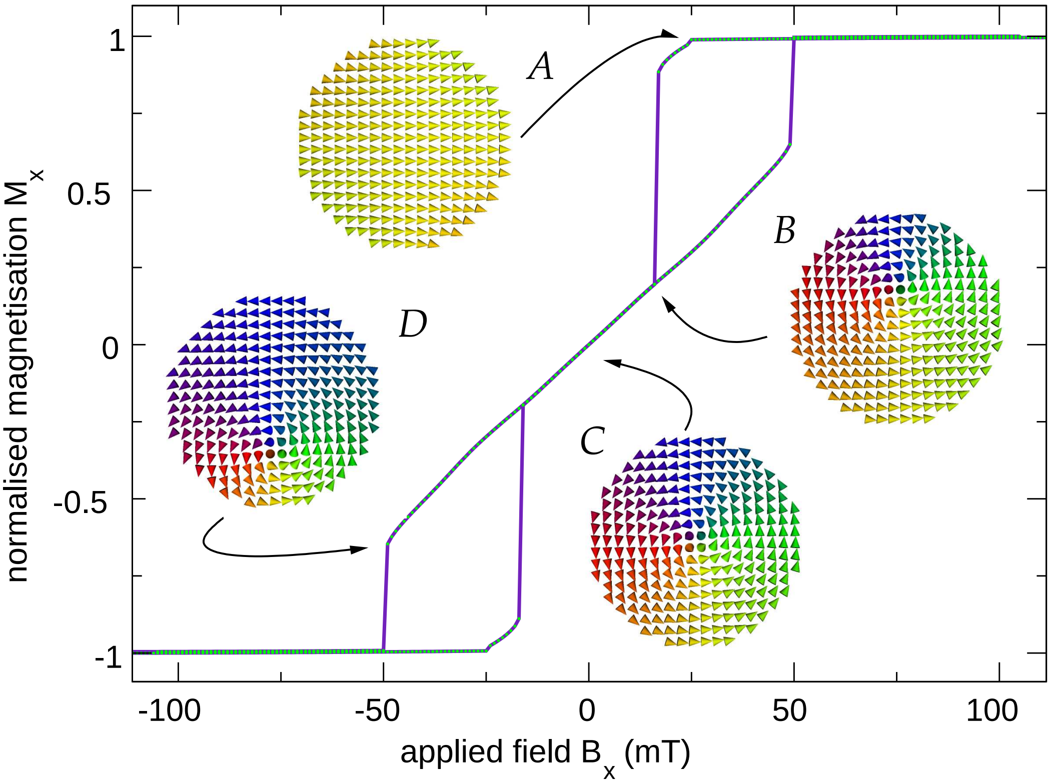

Figure 5.17: The hysteresis loop for the 140nm droplet with inset x-y cut-planes showing vortex propagation

right):

$$l_{z(s)} = 2/7d \tag{5.1}$$

$$l_{z(e)} = 1/7d \tag{5.2}$$

$$\therefore l_z = 3/7d \tag{5.3}$$

$$< 1/2d \tag{5.4}$$

where $l_{z(s)}$ is the part which follows the outline of some bounding sphere of diameter d, and $l_{z(e)}$ is the upper ellipsoidal dome part. These parameters most closely reflect the geometry of droplets resulting from the partial filling of templates with spherical voids. We study the results of simulations performed on such nanodots with d between 50nm and 500nm.

5.5.2 Reversal mechanism

Figure 5.17 shows the hysteresis loop for a droplet with bounding sphere diameter d = 140nm. From an initially homogeneous magnetisation brought about through the application of a saturating magnetic field in the x direction, a slight tapering effect appears at the surface as this field is reduced owing to long-range dipolar

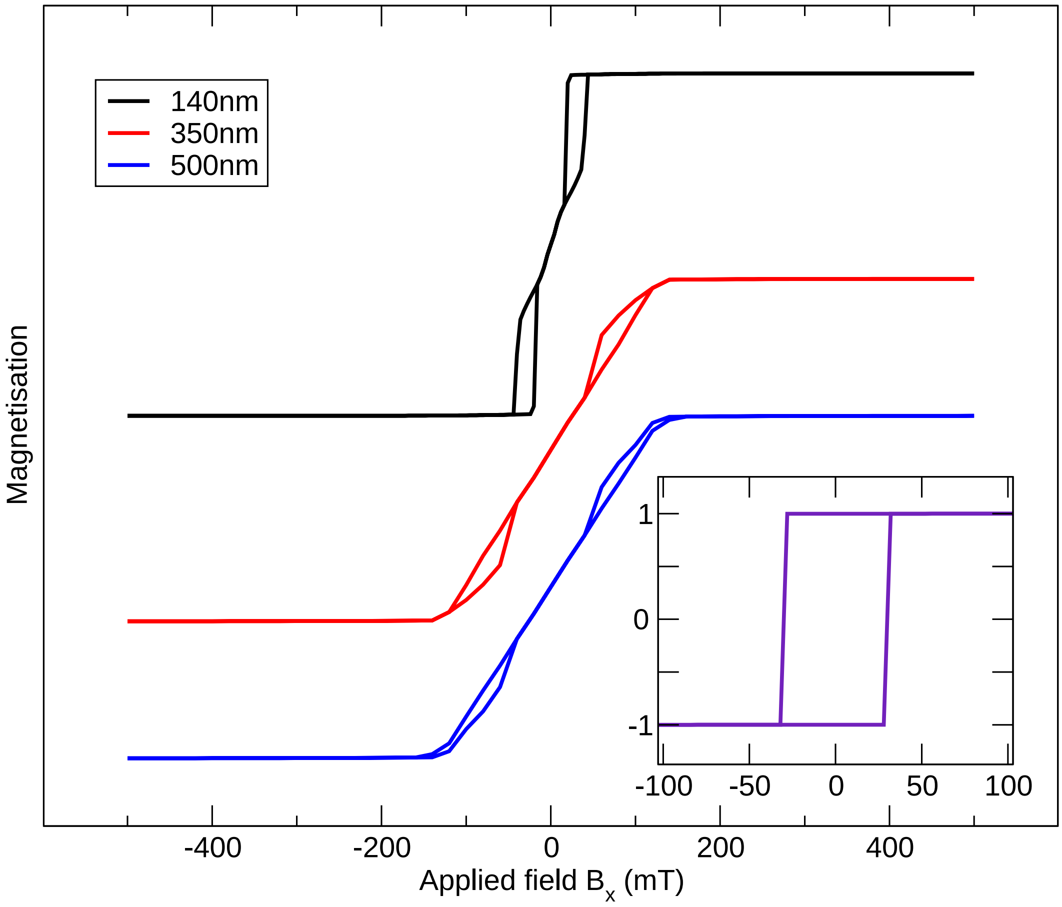

Figure 5.18: Hysteresis loops for droplets of bounding sphere diameter 140nm, 350nm and 500nm; note that the loops are offset in the y direction for clarity. Inset is the hysteresis loop for a droplet of bounding sphere diameter 50nm.

interactions (see figure 5.17, point A).

Further reduction of the applied field causes the dipolar energy to become more dominant. At slightly above zero field this causes the formation of a vortex slightly away from the sample centre (see figure 5.17, point B), the direction of which allows the overall magnetisation direction to remain in that of the applied field. The vortex moves closer to the centre of the sample as the field tends towards zero, and when there is no applied field, the Zeeman energy term is also zero and the vortex moves to the centre.

The net magnetisation M_x of the sample at this point is now zero (see figure 5.17, point C). Reducing the field further (*i.e.* increased in the opposite direction) shifts the vortex further across the sample (see figure 5.17, point D), until the Zeeman energy term influences the magnetisation more than the other energy terms and the magnetisation of the sample becomes homogeneous in the direction of the applied field.

It is interesting to note that if the height $l_{z(s)}$ from equation 5.1 is increased to around $0.5d$, the reversal mechanism is slightly different. Although the magnetisation falls into the vortex state, only the lower half of the vortex moves through the system; the upper half is 'pinned' to the centre of the ellipsoidal part during the entire reversal in a similar fashion to the three-quarter sphere in figure 5.16. This gives the vortex a pendulum-like movement throughout the system. Indeed, immediately after nucleation, the vortex is almost flat across the droplet in the plane of the applied field in a similar way to the sphere in section 3.5.

5.5.3 Size dependence

We have varied the diameter d of the droplet from 50nm to 500nm and computed a hysteresis loop for every d in steps of 10nm. We find two different régimes. Figure 5.19 reflects the size dependence of the coercive field for these droplets.

When $d <$ 140nm, the magnetisation reversal mechanism is single-domain (see figure 5.21, left and centre). When $d \geq$ 140nm, the magnetisation reverses through the vortex state (see figure 5.17 and figure 5.21, right).

The relatively consistent coercivity of 5mT between 60nm and 130nm in figure 5.19 is a result of a coherent rotation reversal process, unlike that shown by dots smaller than 60nm. The hysteresis loops at 60nm $\leq d \leq$ 130nm are substantially less "square" than those shown with sub-60nm bounding sphere sizes and bear a resemblance to the loops from 140nm and greater droplets, as indicated by the centre loop (d=90nm)in figure 5.21.

Above 140nm the coercivity of the droplets is zero. For droplets of greater size the hysteresis characteristics are similar, although as the size is increased the reversal takes place over an increasingly large applied field, and the smaller loops at the top and bottom of the hysteresis graph become more rounded (see figure 5.18).

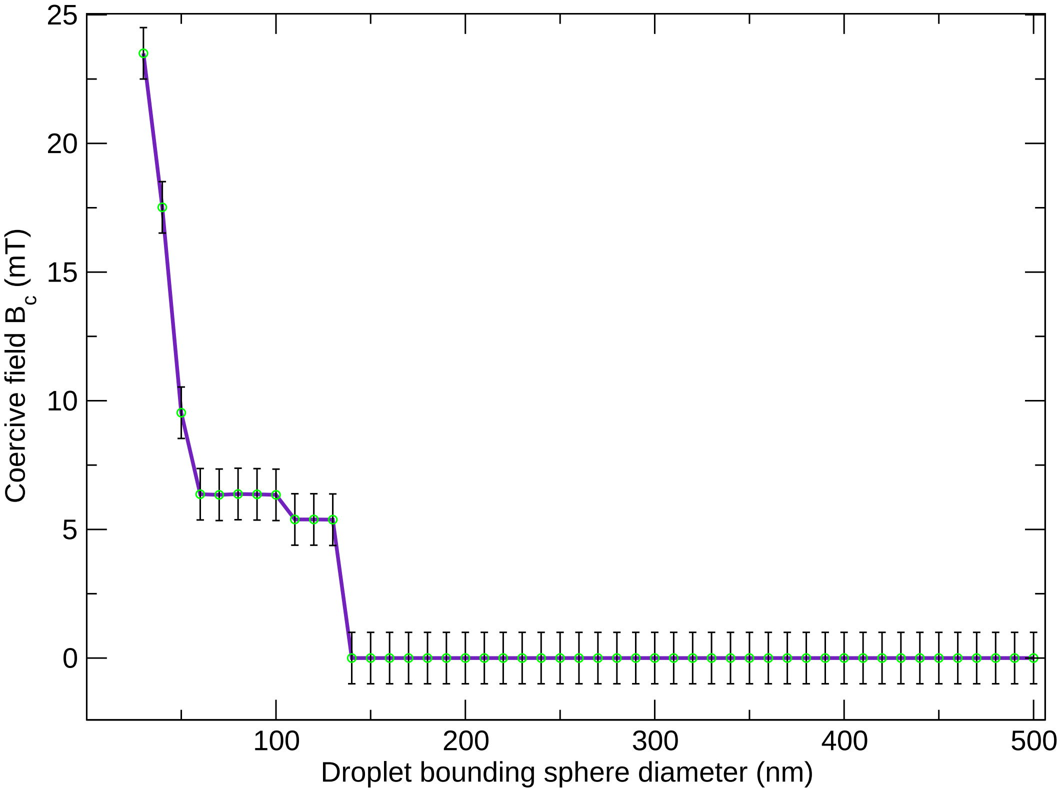

Figure 5.19: Size dependence of coercive field in droplet nanodots. An error of ±1mT is present as this is the applied field step size. Where $B_c > 0$mT, the remanent state is single domain, where $B_c = 0$mT there is a vortex remanent state.

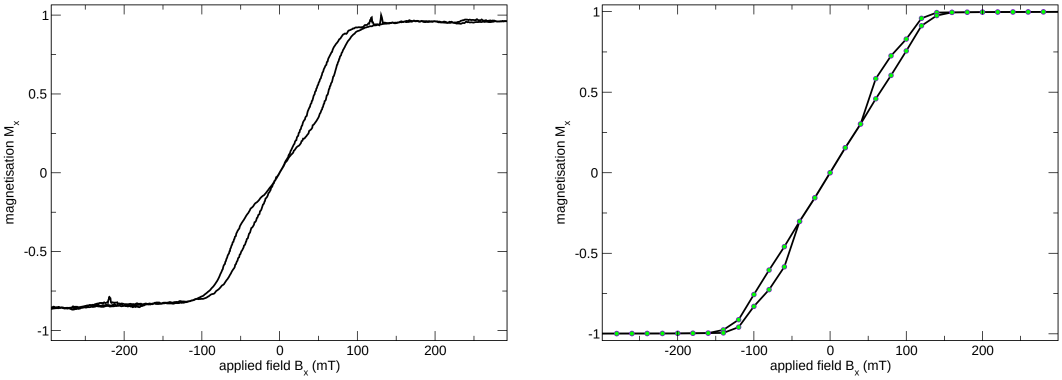

Figure 5.20: Two hysteresis curves for nickel nanodots with bounding sphere diameter of 500nm. The hysteresis loop on the left shows results obtained from experiment. The right-hand loop shows the results of the numerical modelling.

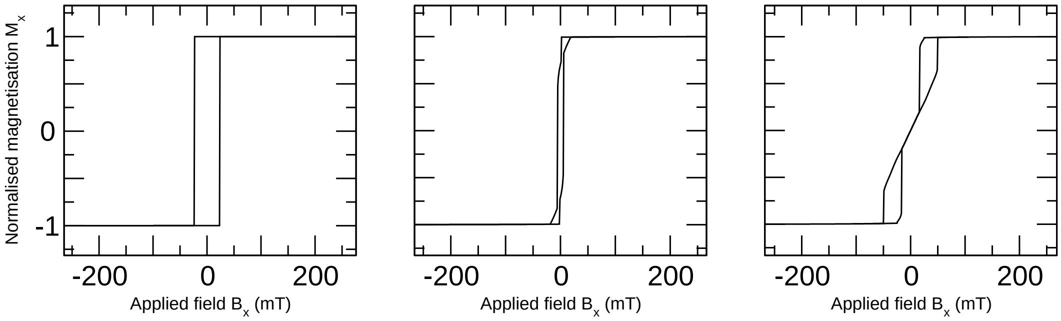

Figure 5.21: Hysteresis loops for droplet nanodots of (from left to right) bounding sphere diameter d of 30nm, 90nm and 140nm

There is a good agreement between the experimental hysteresis curve measured across a nickel nanodot of bounding sphere diameter 500nm (figure 5.20, left) and the results of the numerical simulation for the droplet of the same bounding sphere diameter (figure 5.20, right).

5.6 Applying an out-of-plane external field

By adjusting the direction of the applied field such that it is now along the short axis of the droplet, or *out-of-plane*, rather than across the symmetry plane we can perform further studies on the droplet nanodot.

Figure 5.22 demonstrates a typical hysteresis loop obtained from these simulations and also the associated reversal mechanism. The vignette images along the hysteresis loop show a cut-plane of the magnetisation in the xz plane, z being the short axis and that of the applied field. Initially, a high external magnetic field is applied such that the magnetisation becomes homogeneous in $+z$ (point A), then this field is gradually lowered until it is sufficiently high in the opposite direction ($-z$) to maintain a homogeneous magnetisation in this direction.

As the field is reduced, the system falls into the out-of-plane vortex state with no apparent energy barrier to overcome (point B), with the core pointing in the direction of the initial applied field (point C). Further reduction of the applied field results in the magnetisation surrounding the core pointing more towards the direction of the applied field, so that when the applied field is < 0mT the overall magnetisation is in $-z$ (point D). The core, however, remains pointing in $+z$ until around -50mT, at which point the core flips causing the small jump in magnetisation around this point (point E).

Finally, once the magnetisation is sufficiently large in $-z$, the vortex disappears completely and the magnetisation is homogeneous in $-z$ (point F).

Figure 5.23 shows the size dependence of the droplets when the applied field is out of the plane. The coercive field of the droplets decreases as the bounding

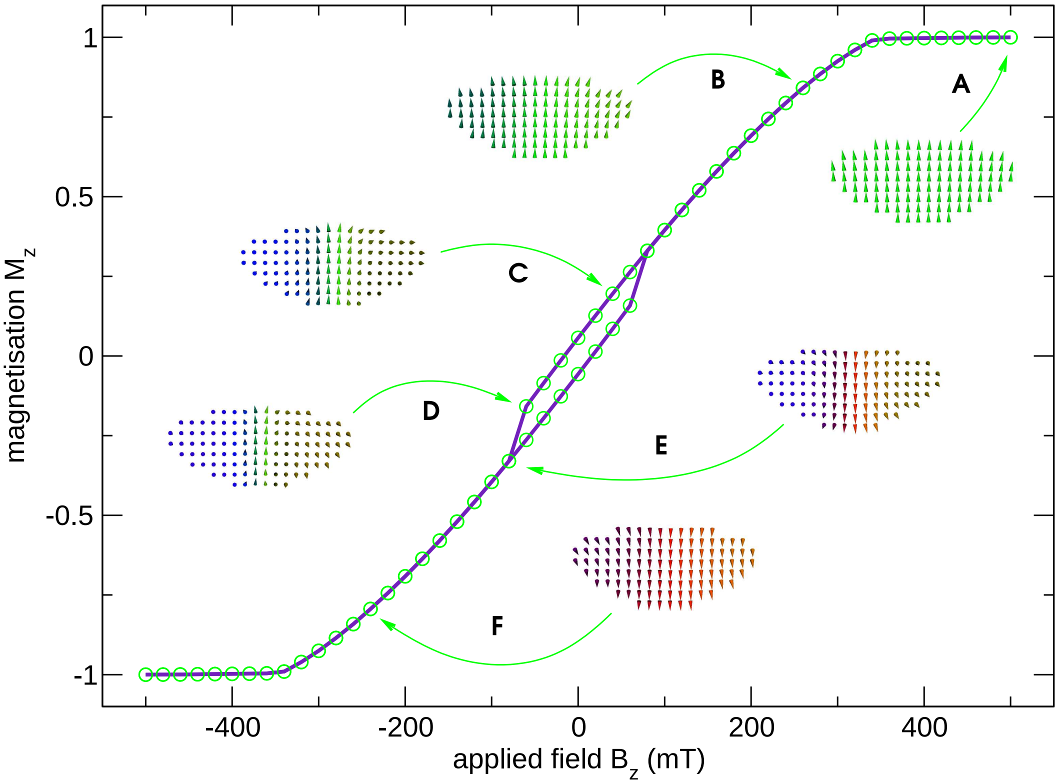

Figure 5.22: Reversal mechanism of a nickel droplet of bounding sphere diameter 200nm in a perpendicular applied field

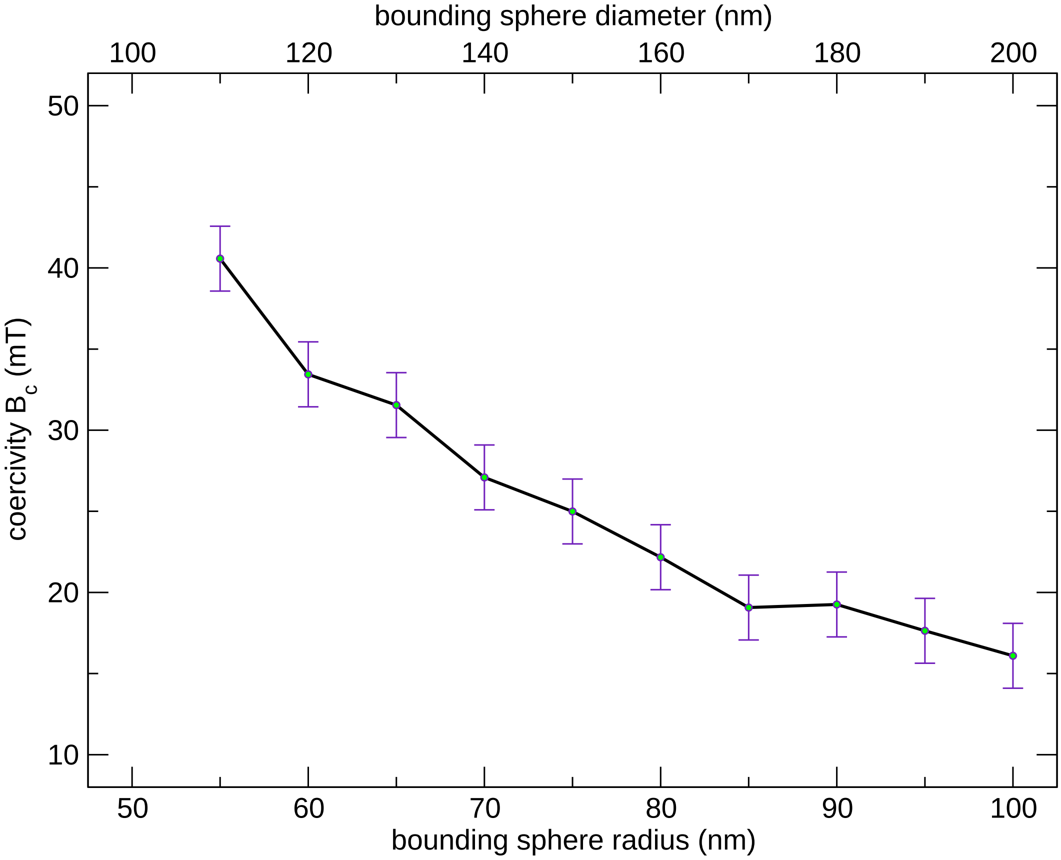

Figure 5.23: Size dependence of the out-of-plane coercive field in droplet nanodots.

sphere radius is increased, with the rate of coercivity reduction decreasing as the radius is further increased.

Figure 5.24 places the coercive field size dependence of the droplets where the initial applied field is out of the plane into context by comparing this to the coercivity of the same droplets when the original applied field is in the plane. It is clear from these results that applying the field across the short out-of-plane axis of the droplets increases the coercivity significantly; for a coercive field of 20mT a droplet of bounding sphere diameter of around 25nm is sufficient with an in-plane applied field, however with an out-of-plane field a bounding sphere diameter of ≈160nm is required.

5.7 Summary

We have simulated the magnetisation reversal in part-spherical and droplet nanodots. In droplet nanodots, we observe two different mechanisms for this reversal — the single-domain state and the vortex state.

If the overall size of the droplet system is increased then we notice a distinct transition from the single domain state to the vortex state, which we identify for

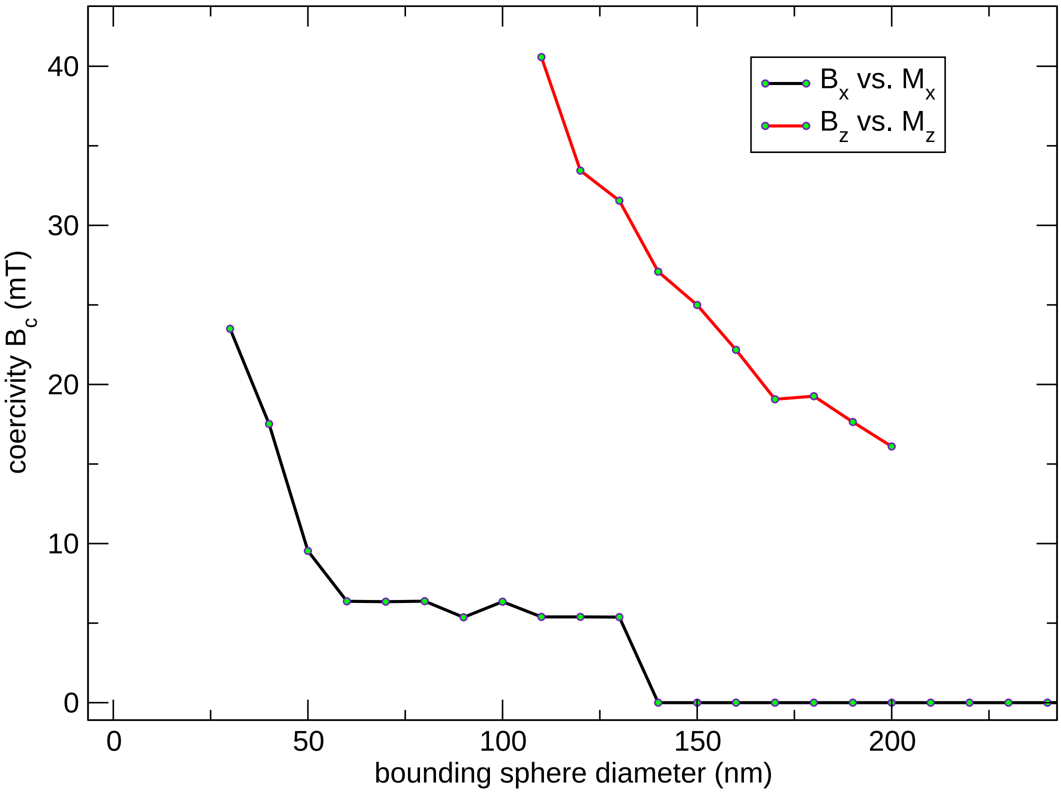

Figure 5.24: Size dependence of the out-of-plane (see figure 5.19) and in-plane coercive field (see figure 5.23 in droplet nanodots. M_x is the in-plane magnetisation, B_x the in-plane applied field, M_z the out-of-plane magnetisation and B_z the out-of-plane applied field

isotropic nickel (see appendix C) as being at a droplet bounding sphere diameter of 140nm (physical droplet diameter in this instance is around 90% of the bounding sphere diameter, approximately 126nm, and $h = 3/7d = 60$nm). This change occurs at a smaller diameter than for thin ($h \leq 30$nm) circular nanodots (see figure 3.10).

The "soft" vortex behaviour — *i.e.* the vortex will readily adjust its position to accommodate a change in applied field — observed in the large droplets is a useful characteristic in sensor applications; smaller droplets have the square hysteresis loops desirable for data storage.

In part-spherical particles, three separate remanent states — single-domain, out-of-plane vortex and in-plane vortex — have been observed.

As the diameter of the part-spherical particle decreases, a larger h/d is necessary for a vortex to form. As h is increased, the magnetisation is more likely to form a vortex. Below a critical radius of 12.4nm for $\mathrm{Ni}_{50}\mathrm{Fe}_{50}$, all h/d values will result in a single-domain remanent state.

The hysteresis loops observed experimentally agree well with the numerical results from the simulation.

We observe good agreement between the finite difference method in *OOMMF* and the hybrid finite element/boundary element model in *magpar*.

Chapter 6

Antidots

Parts of this work have been submitted for publication as *Zhukov et al.* (2004a) and *Zhukov et al.* (2004b). Experimental measurements were obtained by Dr. Alexander Zhukov of the School of Physics and Astronomy (University of Southampton) and the Monte Carlo simulations performed by Dr. Hans Fangohr of the School of Engineering Sciences (University of Southampton).

6.1 Introduction

Lithographic techniques have allowed researchers to create ordered structures on the sub-micron scale (*Cowburn et al.*, 1997, *Fruchart et al.*, 1999, *Hehn et al.*, 1996, *Martín et al.*, 2003, *Van Roy et al.*, 1993), either as well-formed small magnetic elements such as the cylindrical and spherical objects described in chapters 3 and 5 or as regular arrays of holes in magnetic films. *Antidots* are the 'opposite' of the nanodots discussed in the previous chapter. If one creates a hole in a thin sample, the hole can be considered to be an antidot. Lithographic techniques generally yield cylindrical holes, but emerging self-assembly techniques (*Bartlett et al.*, 2002) promise a wider range of shapes.

Figure 6.1 shows the single-template self-assembly technique. Electrochemical deposition can be used to create nanoscale magnetic materials by creating an ordered template from polystyrene latex spheres of size order 50nm $\leq d \leq$ 1000nm (*Bartlett et al.*, 2003b, *Xu et al.*, 2000). Initially, an aqueous solution of monodisperse latex spheres is deposited on a glass substrate. On this substrate sputtered buffer layers of chromium and gold have been deposited, with thicknesses of 10nm and 200nm respectively.

Over a period of between three and five days the evaporation of the water leads to the formation of the template: the combination of the electrostatic repulsion between the latex spheres and the attractive capillary forces provided by the evaporation of the water produces a well-ordered close-packed structure (*Bartlett et al.*, 2002, 2000, 2003b).

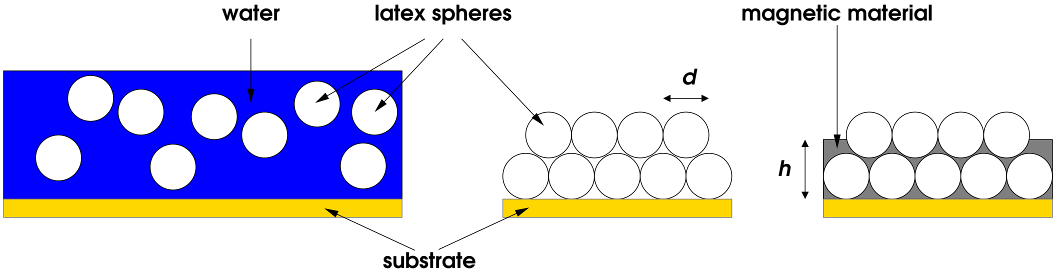

Figure 6.1: The single-template self-assembly technique. Latex spheres of diameter d are poured on to a substrate (left). As the water evaporates, the latex spheres become close-packed, forming a template (centre) which can then be filled with a magnetic material from the substrate upwards to a height h (right).

Using electrodeposition from the gold layer, the electrodeposited material fills the spaces between the latex spheres, using the spheres as a mould. By dissolving the latex spheres in toluene, 3D antidot arrays with spherical holes are formed.

Different thicknesses of antidot arrays can be formed by adjusting the charge during the electrodeposition process, while the period of the antidots is controlled by altering the diameter of the latex spheres.

Figure 6.2 shows a scanning electron microscope image of an antidot array created through the self-assembly template method, and demonstrates the regular structure formed with this process.

Figure 6.3 shows the experimentally-measured coercivity of $\mathrm{Ni}_{50}\mathrm{Fe}_{50}$ antidot arrays with a diameter d of 550nm when the external field is applied in-plane. The coercivity oscillates as a function of height (thickness) h. When the height of the film is close to the sphere centres, the coercivity reaches a local maximum. This oscillatory behaviour is what we wish to understand and explain in this chapter.

6.1.1 The hexagonal lattice

For a hexagonal lattice with base vectors:

$$\mathbf{a}_1 = a\hat{\mathbf{x}} \tag{6.1}$$

$$\mathbf{a}_2 = \frac{1}{2}a\hat{\mathbf{x}} + \frac{\sqrt{3}}{2}a\hat{\mathbf{y}} \tag{6.2}$$

$$\mathbf{a}_3 = \sqrt{\frac{8}{3}}a\hat{\mathbf{z}} \tag{6.3}$$

the lattice points are:

$$\mathbf{P} = n_1\mathbf{a}_1 + n_2\mathbf{a}_2 + n_3\mathbf{a}_3 \tag{6.4}$$

$$(n1, n2, n3) \in \mathbb{N}^3 \tag{6.5}$$

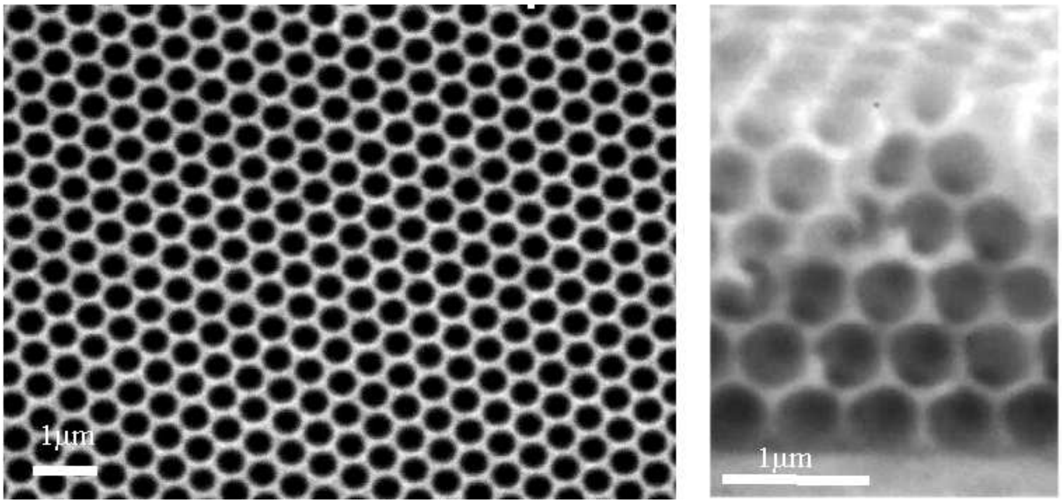

Figure 6.2: Scanning electron microscope image of an antidot array created by the self-assembly template method. The image on the left shows the top of the array; the right-hand image shows the honeycomb-like structure at the edge of the sample

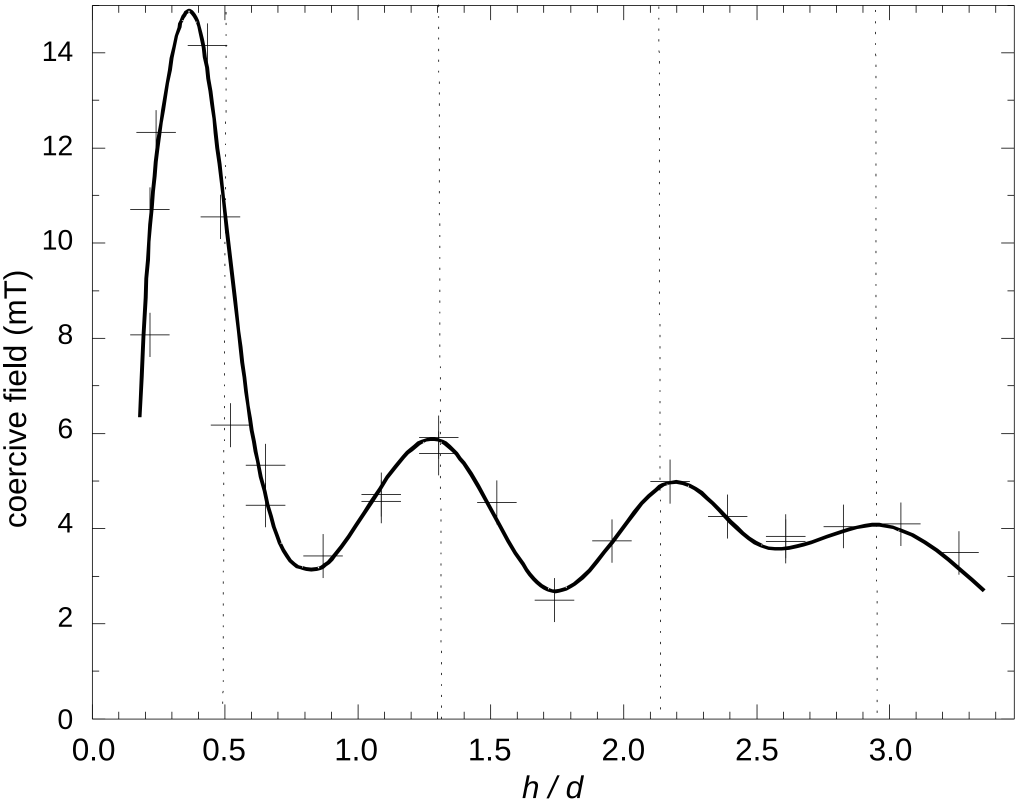

Figure 6.3: Experimentally observed coercivity oscillation in $Ni_{50}Fe_{50}$ antidot arrays of d=550nm against the height (thickness) h of the film. The dashed lines indicate the positions of sphere centres for each layer in the close-packed structure. The coercivity shows maxima close to the sphere centres. The solid line is a guide to the eye

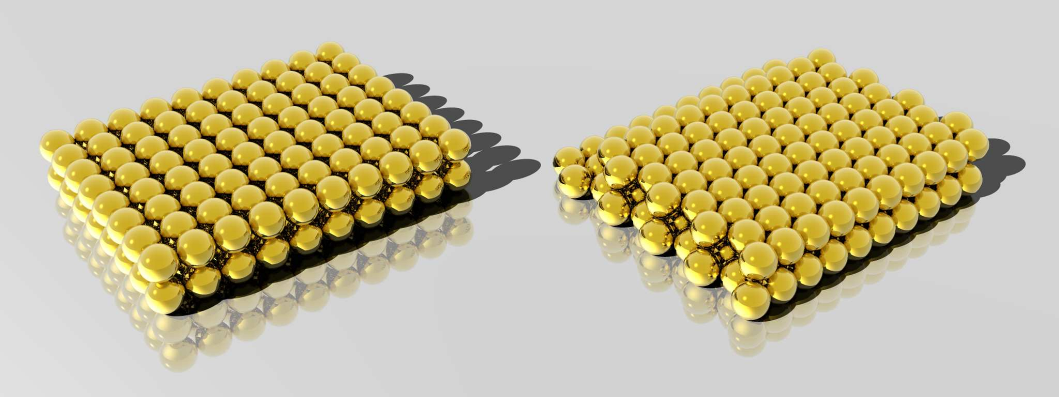

Figure 6.4: Two layers of spheres packed cubically (left) and hexagonally (right)

Shown in figure 6.4 on the right is a hexagonal structure which exhibits this property. However, one should note that there are two ways of packing this layer as there are two positions in which the first sphere can be placed. The two structures are called *hexagonal close-packed* and *face-centred cubic*. The hexagonal close-packed structure, or *hcp*, has the third layer in c having the same x and y coordinates as the first layer, the second layer has the same x and y coordinates as the fourth layer (ABABAB...) and so on (*Kittel*, 1996). The face-centred cubic structure has an alternative arrangement of spheres in the third layer where the spheres share the same x coordinate with the first layer but have different y coordinates (ABCABC...). Although this arrangement appears at the outset to be hexagonal, by rotating its primitive cell the vectors can be shown to be a variant of a cubic lattice.

6.2 Parameters of the antidot system

Since three-dimensional arrays of objects become rapidly impractical to simulate even across modern supercomputing clusters, a feasibility study was conducted to assess the limits of the available hardware when computing the hysteresis loops for these systems.

A set of different self-assembled experimental samples were prepared from nickel, iron, cobalt and $Ni_{50}Fe_{50}$ permalloy from spheres sized 20nm $\leq d \leq$ 1000nm. For the initial micromagnetic study we chose to model the nickel sample. Nickel has a relatively large exchange length ($\lambda_{\mathrm{ex}} \approx$ 7.5nm) when compared to $Ni_{50}Fe_{50}$ permalloy ($\lambda_{\mathrm{ex}} \approx$ 2.75nm), allowing for physically larger systems to be computed within a simulation domain of a comparable discrete cell count.

For the simulations, the parameters for amorphous nickel were selected ($M_s =$ 4.93$\times 10^5$ A/m, $A = 8.5\times 10^{-12}$ J/m, $K_1 = 0$ J/m^3) and to improve convergence a damping constant α of 0.25 was chosen.

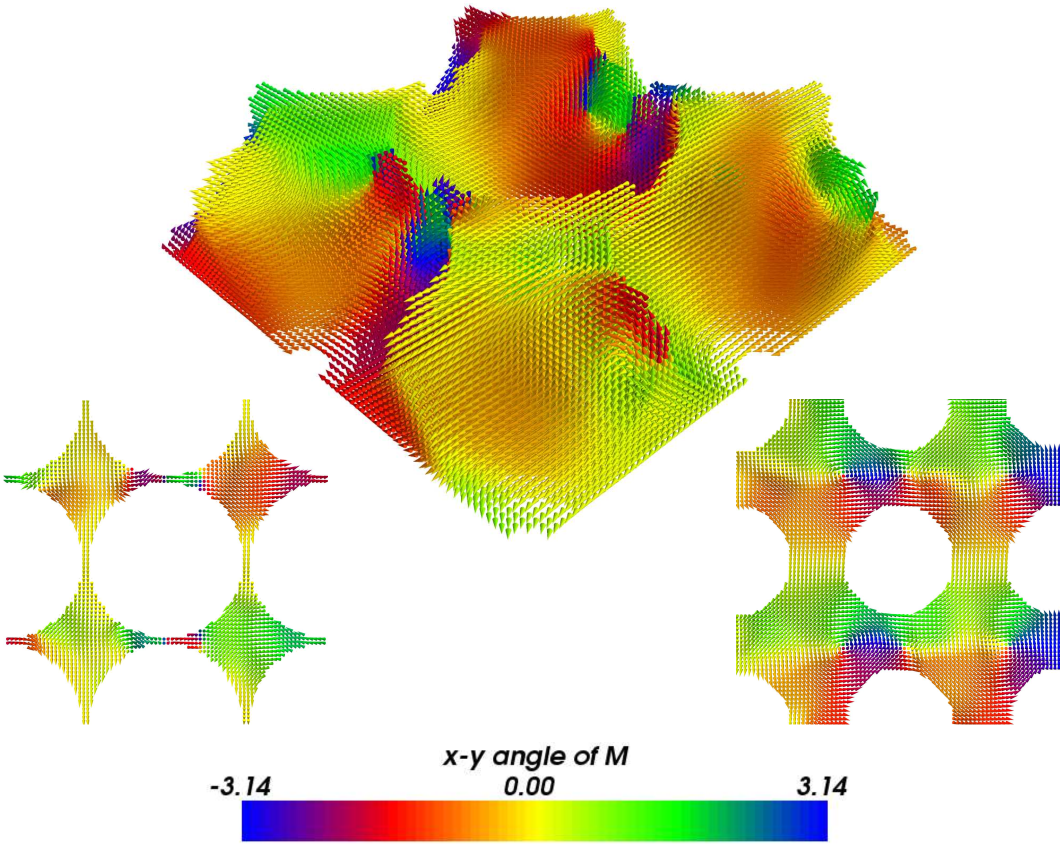

Figure 6.5: 600x600x150nm cut of simple cubic nickel antispheres in zero applied field. The colouring represents the angle between x and y in radians; the lower left inset shows an x-y cut-plane through the centre of the sample, the lower right shows a cut-plane through a lower part of the same sample

6.3 Three-dimensional model

A cubic arrangement of antispheres of radius 150nm cut from a sample of nickel of dimensions 600nm × 600nm × 150nm was prepared and the remanent magnetisation computed for this system with a finite difference cell edge length of 5nm. These particular dimensions were chosen as they represent the largest system which can be simulated in a timely fashion.

The magnetic microstructures which this system creates in zero applied field after being relaxed from an initially homogeneous state in the x direction can be seen in figure 6.5. Unfortunately it would appear that the effect of the edges in this system overwhelmingly influences the microstructure, so such a small sample does not provide a particularly useful insight into an effectively infinite array of antispheres. In particular, the relatively thin physical walls in the z direction which exist in this arrangement apparently act as pinning centres of sorts; since it is difficult for the system to influence the middle of these walls, the system must have a significantly large external magnetic field applied to it for these spins to reverse

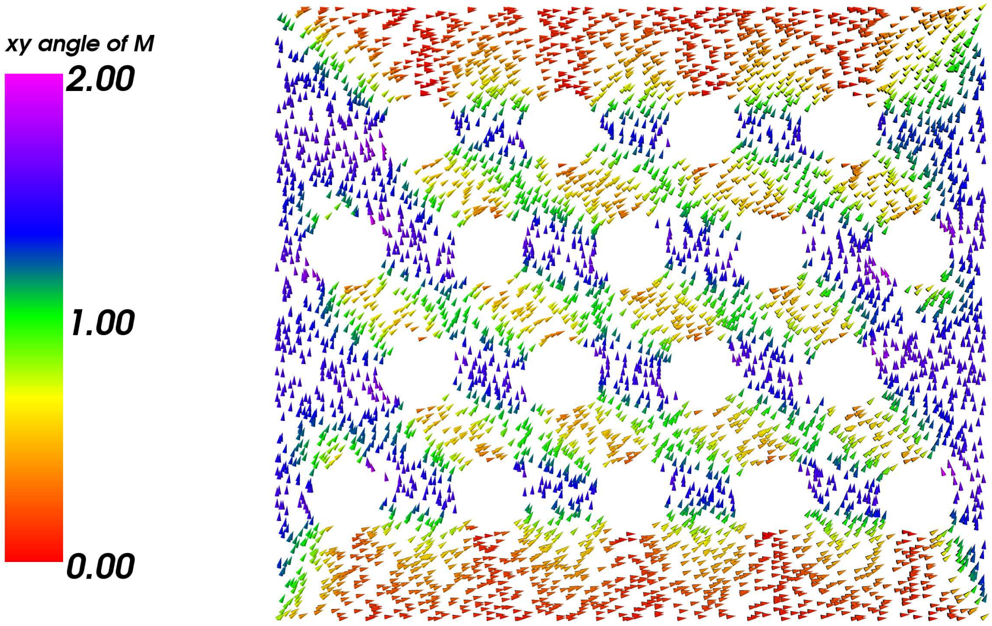

Figure 6.6: Magnetisation of a cobalt hexagonal antidot array in zero field; direction of initial applied field $\theta = 30^o$, $d = 300\text{nm}$, $\frac{r}{R} = 0.4$, $h = 0.05d$

their direction of magnetisation.

For more useful results to be obtained, a much larger system is required. Instead of 3×3 antisphere centres being present in the system, we estimate 5×5 or more centres would be necessary to reduce the effects of the sample edges enough to accurately reflect the microstructures which form within the experimental sample.

Zhukov et al. (2003) perform experimental measurements on large hexagonal arrays of isotropic $Ni_{50}Fe_{50}$ permalloy antispheres ($M_s = 1.1 \times 10^6$ A/m, $A = 5.85 \times 10^{-12}$ J/m, $K_1 = 0$ J/m^3); this permalloy variant has a particularly small exchange length ($\lambda_{\text{ex}} = 2.76$ nm) and as such requires a finer mesh. When this fine mesh is combined with the need for a large number of antisphere centres, it becomes unrealistic to perform even one simulation of the resulting structure.

6.4 Two-dimensional model

By considering only two-dimensional cut-planes of the hexagonal antispheres — assuming that the individual layers behave independently — it is possible to simulate significantly larger systems in the x and y directions than if attempting to perform a simulation across a three-dimensional sample of similar proportions. We can then measure the coercive field for different layers.

The hexagonal antisphere systems in *Zhukov et al.* (2003) can be mapped to two-dimensional samples by considering hexagonally-spaced circular holes — flat

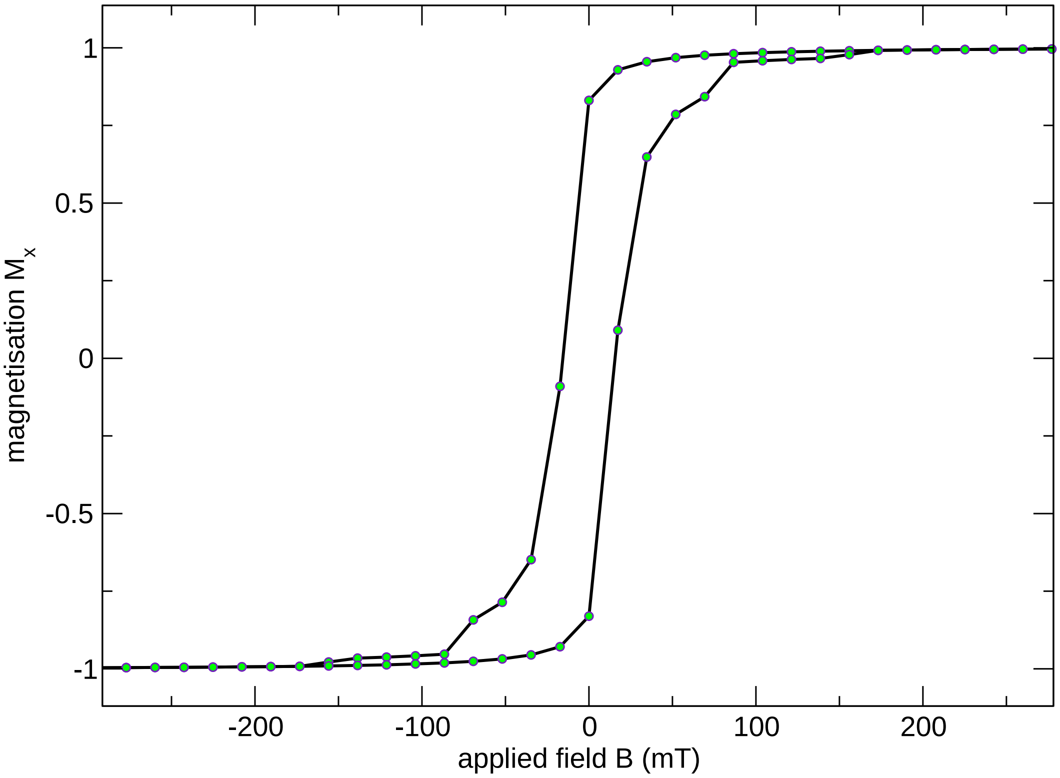

Figure 6.7: Hysteresis loop for a 2d array of hexagonally arranged permalloy antidots ($d = 100$nm, hole radius to spacing period radius ratio $r/R = 0.4$) in an in-plane applied field offset 30 degrees from the x direction

antidots — in a thin film. By varying the ratio of hole radius r to spacing radius R the surface of the antisphere geometry at different heights can be modelled reasonably accurately. Since larger systems can be simulated, the influence of the sample edges detailed in section 6.3 is substantially reduced (figure 6.6).

6.5 Stray field measurement

The development of the scanning tunnelling microscope (STM) allowed scientists to determine the electronic topography of a sample with a resolution down to a few ångstroms (*Binnig and Rohrer*, 1985, *Binnig et al.*, 1982, 1983). The atomic force microscope (AFM) is a further development of the STM which exploits the deformation of a spring attached to a cantilever to allow the measurement of the force exerted on the sharp AFM tip (*Binnig et al.*, 1986).

To characterise the magnetic properties of a sample, the standard diamond tip of the AFM is replaced by a ferromagnetic tip (*Rugar et al.*, 1990, *Sáenz et al.*, 1987) allowing the observation of magnetic domain structures by measuring the force gradient exerted on the tip by the stray field as a function of the position — a technique known as magnetic force microscopy (MFM) . Rather than the tip following the surface contours of the sample as in STM, the MFM operates with the tip at a fixed z point in space.

To assess the appropriateness of the two-dimensional approximation above, we compute the stray field and compare this to the experimental images provided through magnetic force microscopy.

The tip of an MFM is magnetic and we assume that it is a dipole $\mathbf{d}$. In the absence of knowledge of the precise magnetisation of the tip, this is the simplest approach possible (*Barthelmeß et al.*, 2003). The signal which the MFM records is proportional to the gradient of the demagnetising field $\mathbf{H}_{\mathrm{de}}$.

6.5.1 Numerical calculation of the stray field

We compute the stray field from our simulation data as it would be read from a magnetic force microscope by simulating several layers of “empty space” above the sample and measuring the demagnetising field. This has the advantage that the efficient *OOMMF* algorithm for the computation of the demagnetising field can be used. However, we need to compute the second derivative numerically (using central differences):

$$\frac{\partial^2 f}{\partial x^2} = \frac{f(x+h) - 2f(x) + f(x-h)}{h^2} + \mathcal{O}(h^2) \tag{6.6}$$

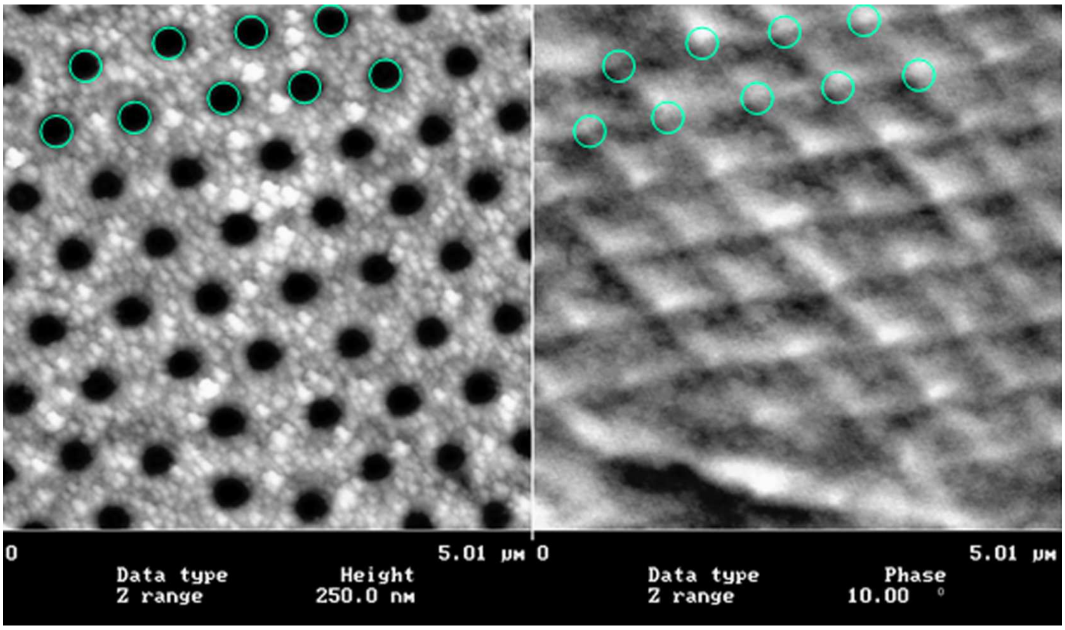

Figure 6.8: Microscopic images of an antidot array. The tunnelling image on the left shows the location of the antidots; the magnetic force microscopy image on the right highlights the demagnetisation field

where h is the distance between the upper and lower layers of the demagnetising field.

6.5.2 Stray field calculation through analytical techniques

Alternatively, we can interpret the discrete magnetisation vector $\mathbf{M}(\mathbf{r})$ at the surface of the sample as a layer of dipoles and compute the stray field at the MFM tip and consequently the second derivative analytically.

This approach is more accurate in determining the second derivative because h in equation 6.6 cannot be made arbitrarily small. Additionally, an analytical approach is more flexible with respect to the fly height of the MFM tip.

It should be noted that this approach ignores the higher order magnetic moments associated with each simulation cell in *OOMMF* by replacing them with the leading dipole term. This is justified if the height of the MFM tip above the sample surface is much greater than the *OOMMF* cell spacing.

The second derivative of the demagnetising energy should be proportional to the signal at the tip of a magnetic force microscope and can be shown (see appendix A) to be:

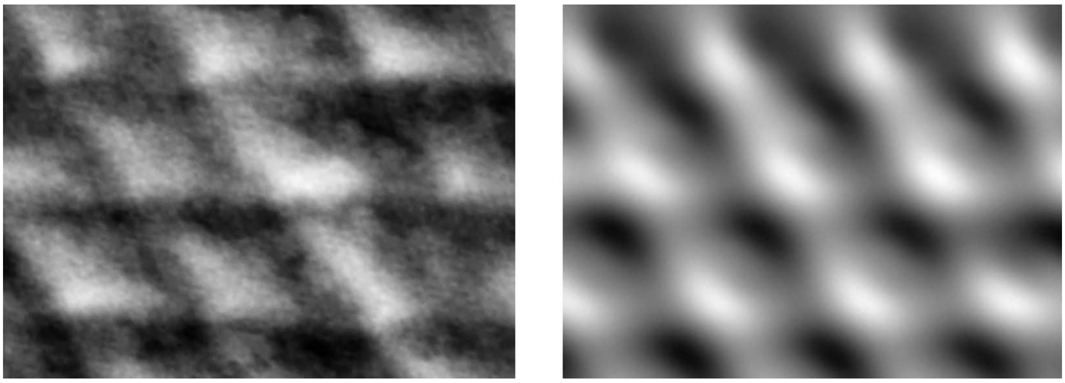

Figure 6.9: Demagnetising field of an antidot sample in zero applied field as measured by the tip of the magnetic force microscope (left) and the second derivative as computed through the analytical techniques from equation 6.7 (right)

$$\begin{aligned}
\frac{\partial^2 E_d}{\partial z'^2} &= \mu_0 \Biggl(\frac{-3\cdot \mathbf{m}\cdot\mathbf{m}'}{|\mathbf{r}-\mathbf{r}'|^5} \\
&\quad + \frac{15\cdot \mathbf{m}\cdot\mathbf{m}'(z-z')^2}{|\mathbf{r}-\mathbf{r}'|^7} \\
&\quad - \frac{6\cdot m'_z m_z}{|\mathbf{r}-\mathbf{r}'|^7} \\
&\quad + \frac{30(\mathbf{m}\cdot(\mathbf{r}-\mathbf{r}'))m'_z(z-z')}{|\mathbf{r}-\mathbf{r}'|^7} \\
&\quad + \frac{30(\mathbf{m}'\cdot(\mathbf{r}-\mathbf{r}'))m_z(z-z')}{|\mathbf{r}-\mathbf{r}'|^7} \\
&\quad + \frac{15(\mathbf{m}\cdot(\mathbf{r}-\mathbf{r}'))(\mathbf{m}'\cdot(\mathbf{r}-\mathbf{r}'))}{|\mathbf{r}-\mathbf{r}'|^7} \\
&\quad - \frac{105(\mathbf{m}\cdot(\mathbf{r}-\mathbf{r}'))(\mathbf{m}'\cdot(\mathbf{r}-\mathbf{r}'))(z'-z')^2}{|\mathbf{r}-\mathbf{r}'|^9} \Biggr)
\end{aligned} \tag{6.7}$$

This assumes that the tip of the MFM is a dipole:

$$\mathbf{m}' = \begin{pmatrix} 0 \\ 0 \\ C \end{pmatrix} \tag{6.8}$$

The full derivation of this can be found in appendix A.

Figure 6.9 shows the comparison between the experimental data measured with a magnetic force microscope in zero applied field and the second derivative of the demagnetising field as calculated by the above equation. There is a significant similarity between the images; both show a characteristic periodic parallelogram pattern. The tip distance, both experimental and computed, was half of the distance between the antidot centres.

Figure 6.10 shows a clear agreement between the measurements from the MFM

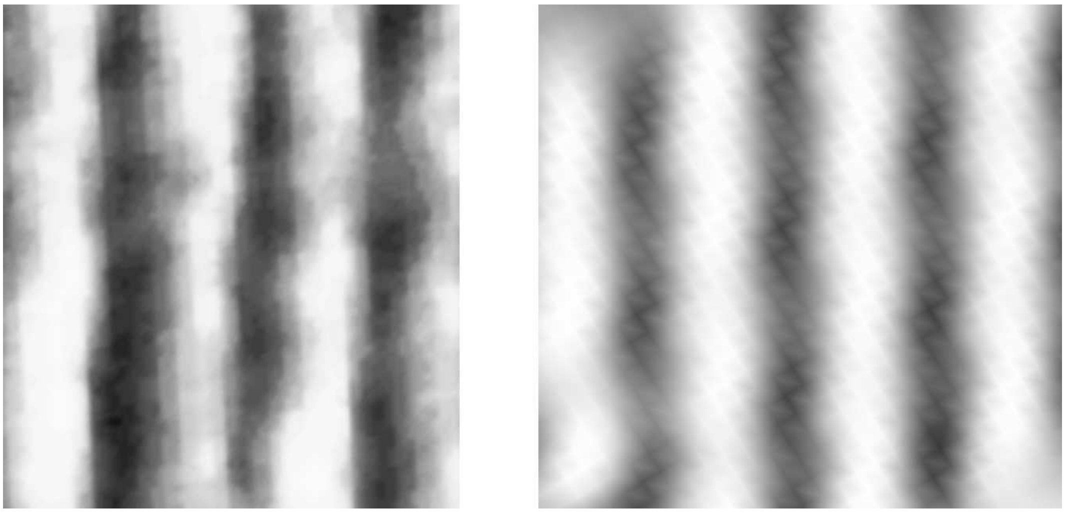

Figure 6.10: Measured MFM signal of a three-dimensional antidot sample in a small (≈10mT) applied field (left) and simulated MFM signal of a simulated two-dimensional layer using equation 6.7 (right)

in a small applied field (approximately 10mT) and the computed stray field from the simulation results.

Figures 6.9 and 6.10 suggest that the simulation of a two-dimensional layer with cylindrical holes produces a magnetisation which is at least qualitatively in agreement with the measured magnetisation in the top layer of a three-dimensional sample with spherical holes.

6.6 Monte Carlo simulation

In section 6.4 we described a method for extracting the coercive field of the two-dimensional antidot layers. The assumption with this approach is that the layers are independent, however different layers interact via the exchange coupling. A Monte Carlo simulation is used to simulate the reversal behaviour of a stack of exchange-coupled two-dimensional layers. It is assumed that all magnetic moments in one two-dimensional layer point in the same direction, *i.e.* each layer is treated as a single Stoner-Wohlfarth particle (see figure 6.11).

By taking the computed coercive field B_c from the two-dimensional model as a function of r/R, we can determine an effective anisotropy energy K (arising from the adapted Stoner-Wohlfarth model described in appendix B considering anisotropy and Zeeman components) for each Stoner-Wohlfarth layer with holes of the size r:

$$K_{(r)} = \frac{m_{(r)} B_{c_{(r)}}}{18} \tag{6.9}$$

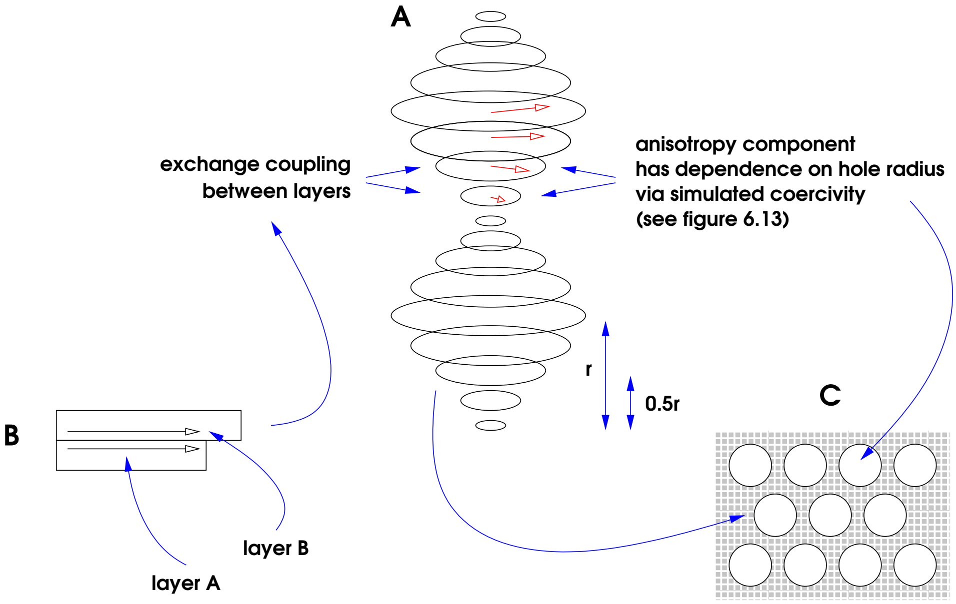

Figure 6.11: Overview of Monte Carlo simulation. A 'stack-of-spins' model (A) is used as a basis for simulation. The 'spins' are coupled by an exchange energy component computed through neighbouring interface atoms (B) between layers. An anisotropy component is computed from the coercivity of the 2D layer (C) and the magnetisation contribution is calculated from the volume of material in each layer. See appendix B for the derivation of the anisotropy component.

where $m_{(r)}$ is the magnetic moment of a two-dimensional layer of 5nm thickness with holes of radius r. Thus, each Stoner-Wohlfarth layer will — if it is decoupled from the other layers — switch at the coercive field as measured in the two-dimensional simulations (see appendix B for the full derivation of equation 6.9).

The layers are coupled by the exchange interaction and the exchange energy can be computed between two neighbouring layers $\mathcal{A}$ and $\mathcal{B}$:

$$\mathcal{E}_{\mathrm{ex}\mathcal{A},\mathcal{B}} = -2\mathcal{N}\mathcal{J}\mathbf{S}_{\mathcal{A}} \cdot \mathbf{S}_{\mathcal{B}} \tag{6.10}$$

$$= -2\mathcal{N}\mathcal{J}S^2 \cos(\phi_{\mathcal{A}\mathcal{B}}) \tag{6.11}$$

where $\mathcal{N}$ is the number of neighbouring atoms, $\mathcal{J}$ is the exchange integral, S is the atomic magnetic moment and $\phi_{\mathcal{A}\mathcal{B}}$ is the angle between the magnetisation in the neighbouring layers. The exchange energy component yielded by this equation represents the energy between the interface of layers $\mathcal{A}$ and $\mathcal{B}$ (point B in figure 6.11).

By performing a Monte Carlo simulation of the system of coupled

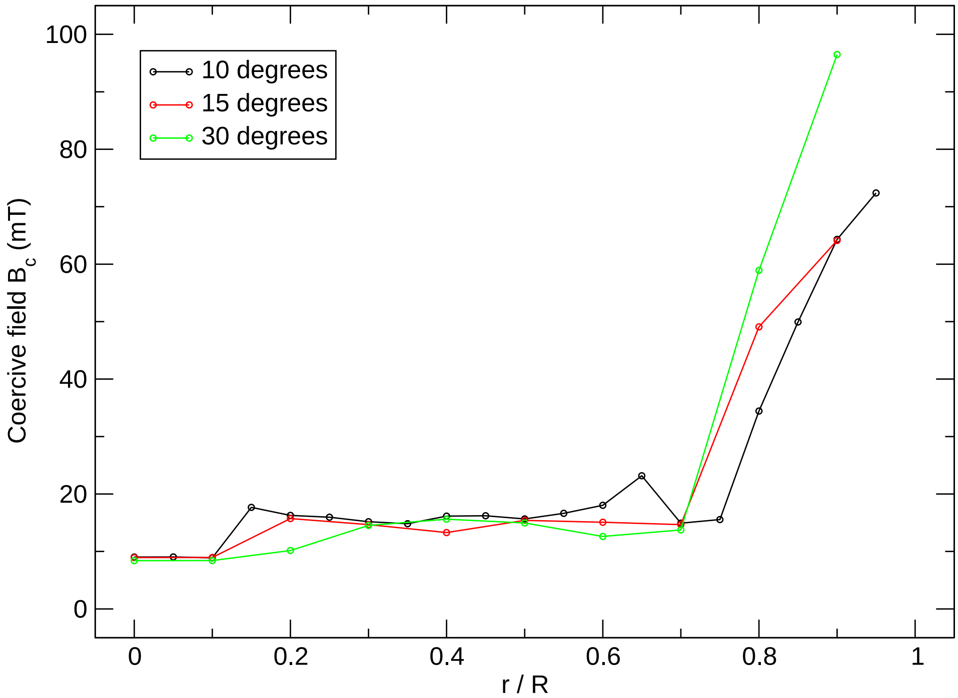

Figure 6.12: Coercivity of a 6x6 permalloy hexagonal antidot array with applied fields 10, 15, and 30 degrees from the x direction (d = 100nm).

Stoner-Wohlfarth layers using the equations above and input parameters for $B_{c_{(r/R)}}$ from the two-dimensional simulations shown in figure 6.12, we are able to more accurately compute the coercive field with respect to the height of the film, and therefore use the results of the two-dimensional simulations to understand a simplified model of the three-dimensional system.

6.7 Results

The calculated hysteresis loop for a two-dimensional permalloy hexagonal antidot sample is shown in figure 6.7, showing a relatively large coercive field of around 25mT. The dot spacing in this sample is 100nm between centres, with the dot diameter being 40% of the dot spacing.

Figure 6.12 shows the effect the radius ratio r/R of the hole to spacing has on the coercivity of the sample. Simulations were performed on permalloy antidots d = 100nm with applied fields offset by 10, 15 and 30 degrees from the x direction. When r/R is below 0.1, the antidots have little effect on the overall coercive field of the sample in all three cases. However, when r/R increases above 0.1, the coercivity doubles sharply for offsets of 10 and 15 degrees; the 30 degree coercivity measurement also increases, but more gradually.

A more drastic change in behaviour is observed when r/R increases to 0.8 and above; the coercivity rapidly increases as a result of the reduction in material be-

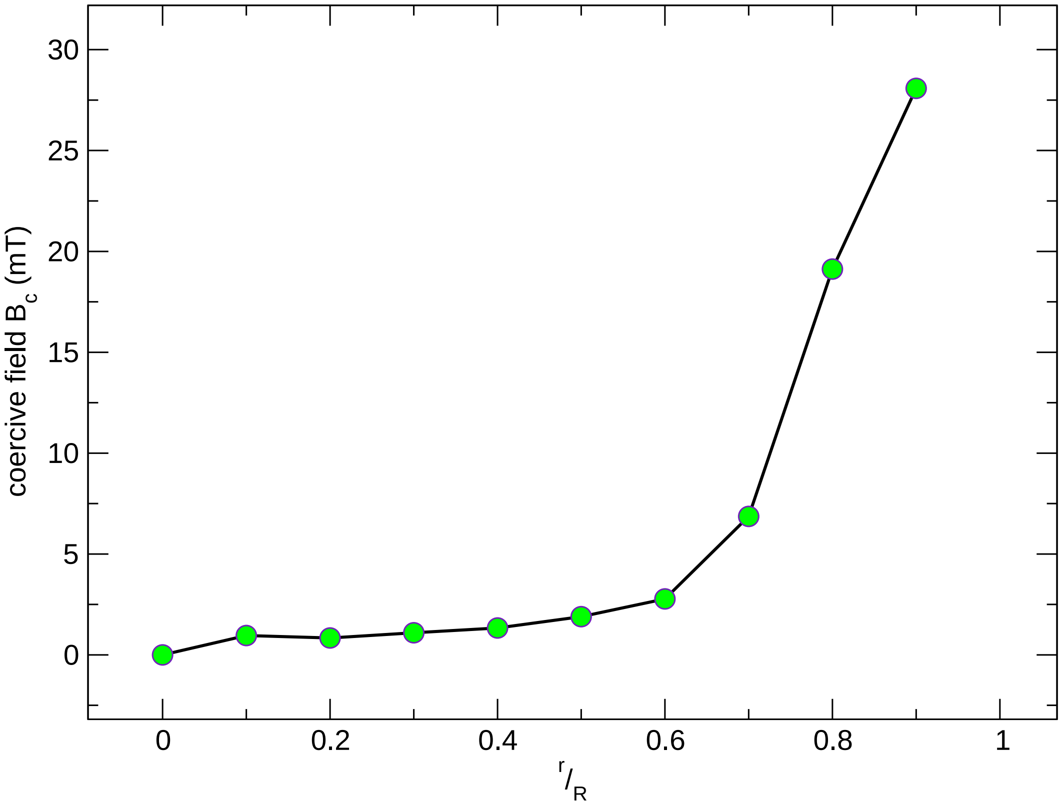

Figure 6.13: Coercivity of a larger 6x6 permalloy hexagonal antidot array with the applied field offset 30 degrees from the x axis (d = 200nm).

tween the antidots; this makes it more difficult for the system to reverse the magnetisation between these thin 'walls' of material. In the most extreme case, the coercivity of the 30 degree sample when r/R is 0.9 is approximately ten times greater than that when r/R is 0.1 and below.

Any simulation performed in the situation where r/R is 1.0 is likely to be inaccurate as the finite resolution of the simulation will not allow the extremely fine walls around the point where the antidots touch to be precisely resolved.

Figure 6.13 shows a coercive field graph of a 30^o offset permalloy antidot system, similar to that shown in figure 6.12 only with d = 200nm. In this larger system, the jump in the system at $r/R = 0.1$ is less pronounced and the coercivity increases in a less abrupt fashion.

Figure 6.14 shows the results of the Monte Carlo simulation using values of $B_{c_{(r)}}$ from the d = 200nm permalloy dataset demonstrated in figure 6.13, comparable to the experimental results shown in figure 6.3.

Figure 6.15 shows on the left an experimental magnetic force microscope image of a cobalt antidot film (d = 700nm, h = 100nm) in zero applied field. The holes at the surface of the antidot film are indicated by the blue circles. The image on the right-hand side shows the remanent magnetisation pattern from the two-

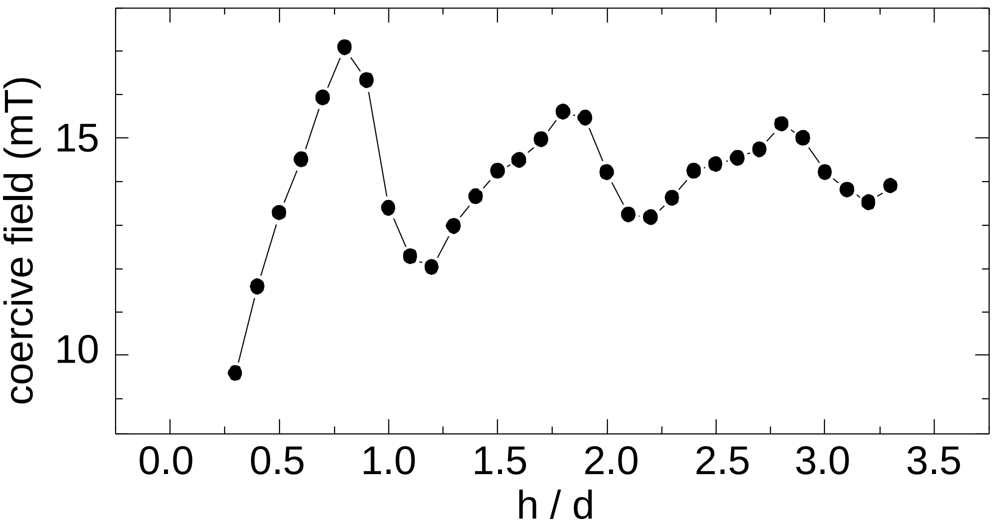

Figure 6.14: Monte Carlo simulation results with $B_{c_{(r/R)}}$ values from figure 6.13

dimensional micromagnetic modelling case when $r/R = 0.5$. In both cases the applied field was 30 degrees from the indicated x axis.

The numerical results show that the magnetisation follows around the holes, forming a consistent periodic microstructure. The magnetisation between neighbours in $\mathbf{a}_1$ (see equation 6.1) is 90 degrees from x (60 degrees from the applied field), but between neighbours in $\mathbf{a}_2$ the magnetisation is 60 degrees from x (30 degrees from the applied field). The magnetisation between neighbours in $(-\mathbf{a}_{2(x)}, \mathbf{a}_{2(y)})$ is 30 degrees from x (aligned with the applied field).

6.8 Summary

We have calculated hysteresis loops, magnetisation patterns and stray fields over antidot samples, and whilst three-dimensional micromagnetic simulations will always be the most accurate way of simulating these shapes, it is not always practical.

In certain situations, particularly where a large simulation domain is desirable, a two-dimensional simulation which accurately reflects the three-dimensional physical sample can offer insight into the magnetisation patterns and in particular the stray field patterns in these physical samples.

In addition, the strong similarity between the experimental MFM results and the computed stray field from the simulation allows us to conclude that the two-dimensional model is a reasonably accurate reflection of the three-dimensional experimental system.

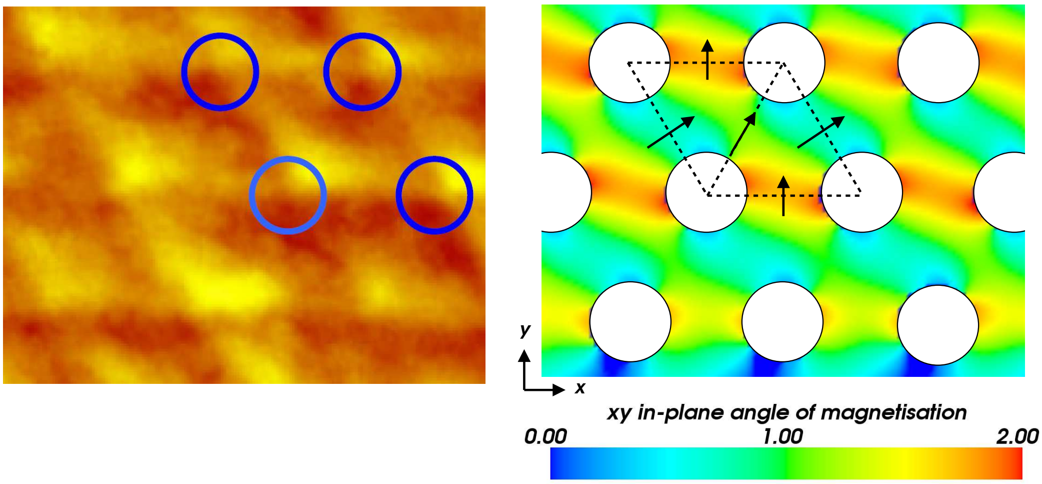

Figure 6.15: Experimental and numerical images for a cobalt antidot film (left) MFM image of film prepared with spheres of diameter 700nm with thickness 100nm; blue circles indicate the position of the holes in the film and (right) magnetisation direction from numerical modelling with $r/R = 0.5$; the colour scale represents the magnetisation angle in the xy plane in radians

6.8.1 Outlook

By using periodic boundary conditions, unfortunately not available in the simulation software, it would be possible to compute a system in three dimensions by making the sample periodic in the x and y directions. Parallel execution of the simulation code coupled with a shared memory model would also make the three-dimensional simulation case feasible.

The next steps in following up the presented results would be to further understand the three régimes in $B_{c(r/R)}$ for two-dimensional systems shown in figure 6.12, in addition to modelling the full three-dimensional system.

Chapter 7

Summary and outlook

7.1 Summary

We have investigated the properties of micromagnetic samples through simulation paying particular attention to shape anisotropy — the influence the shape has on the hysteresis loop and magnetic microstructure.

Most magnetic samples at a nanometre scale possess characteristics desirable for magnetic data storage applications, either as data read/write heads or sensors, where the magnetisation is sensitive to small changes in $\mathbf{B}$, or as storage media with a high coercivity.

We note that cylinders are particularly suitable candidates for storage media when considering their comparatively large coercivity, and our phase diagram identifies the behavioural dependence on diameter and height. Spherical geometries exhibit properties useful for magnetic sensors. Our studies reveal how coercivity decreases when overall diameter is increased.

More complex shapes, such as the cone, half-sphere and the droplet are more flexible, and by subtle alterations in their sizes can be manipulated for use in any data storage application. Size dependence studies in the droplet geometry show that the transition between the single-domain and the vortex state occurs at a bounding sphere diameter of 140nm in nickel. Larger droplets which have reversible characteristics and zero coercivity are ideal for magnetic sensor applications.

Antidots show interesting characteristics when considered in arrays of their peers, and given the flexibility of the coercive field through altering the size of the dots as a fraction of the spacing distance, make good candidates for storage media.

Comparisons between our simulations and experimental results demonstrate a high degree of similarity. We can use micromagnetic simulation to observe hysteretic behaviour and coercivity trends with high confidence, and the study of samples with other geometries and sizes which are not yet feasible for experimentalists to physically produce can yield possible directions for future experimental work.

Overall, we conclude the coercivity of magnetic samples can be controlled by their physical shape and size.

Possible candidates for further simulation include the remainder of the primitive set — torii and pyramids — as well as constructive solid geometries based upon these primitives, for example a tear-drop shape built from a conical upper and a half-ellipsoid lower section. Shapes such as these could be created by combining the self-assembly double-template method outlined in chapter 5 with electron beam lithographic techniques. Using this method it is also possible to create films manufactured from different materials — for example, it might be possible to create a cobalt half-sphere which has a permalloy "hat".

The simulations presented in this thesis were computed as zero temperature. Thermal effects, even at low temperatures, can introduce subtle changes in behaviour. As such, the contribution to the results through finite temperature would be studied in a continuation of this work. Initial studies indicate that the size of secondary hysteresis loop energy barriers in the case of the sphere is reduced at finite temperature.

The work discussed in section 5.5.2 revealed some interesting properties of vortex behaviour in the droplets. Initial studies have shown that the droplets, especially larger ones, demonstrate similar vortex orientations to those found in spheres, although they quickly fall into a more disc-like out-of-plane vortex state as the applied field is further reduced.

A more detailed study will be performed into how the variation of $l_{z(s)}$ and $l_{z(e)}$ from equations 5.1 and 5.1 affects the vortex formation, movement and subsequent disappearance. The effect of magnetostatic energy between adjacent nanodots will also be investigated.

Finally, in chapter 6 we compared experimental data with simulation results produced through two-dimensional simulations, Monte Carlo methods and found a strong similarity between experimental MFM and computed stray field results, corroborating the two-dimensional model presented in that chapter.

Appendix A

Analytical calculation of the stray field

Since the phase shift of the cantilever attached to the sharp tip in a magnetic force microscope (*Sáenz et al.*, 1987) when measured corresponds to the measured signal (*McVitie et al.*, 2001), the second derivative of the stray field (*Hug et al.*, 1998, *Rugar et al.*, 1990) is proportional to the rate of change of the force on the tip (*Barthelmeß et al.*, 2004).

If the second derivative is evaluated at a fixed height above a demagnetising energy dataset of micromagnetic simulation results then this is comparable to a magnetic force microscope. This derivative is presented in this appendix.

The dipolar energy between two points in a magnetic system, assuming each discrete cell is a dipole, can be considered to be

$$E_{\mathrm{pot}} = \mu_0 \frac{\mathbf{m}\cdot\mathbf{m}' - 3(\mathbf{m}\cdot\mathbf{e})(\mathbf{m}'\cdot\mathbf{e})}{|\mathbf{r}-\mathbf{r}'|^3} \forall \mathbf{r} \neq \mathbf{r}' \tag{A.1}$$

where $\mathbf{e}$ is the unit vector of $\mathbf{r}$.

For fixed $\mathbf{m}'$ (such as that in the magnetic tip in magnetic force microscopy), the effective field is

$$\mathbf{H}_d = \frac{\mathbf{m} - 3(\mathbf{m}\cdot\mathbf{e})\mathbf{e}}{|\mathbf{r}-\mathbf{r}'|^3} \tag{A.2}$$

because $E = -\mu_0 \mathbf{m}\cdot\mathbf{H}_d$, noting that $\mathbf{m}$ is located at $\mathbf{r}$ and $\mathbf{m}'$ — the tip — is located at $\mathbf{r}'$. We define:

$$\mathbf{e} = \frac{\mathbf{r}-\mathbf{r}'}{|\mathbf{r}-\mathbf{r}'|} \tag{A.3}$$

For the MFM data:

$$\frac{\partial^2 E_{\mathrm{pot}}}{\partial z'^2} \propto \frac{\partial^2 \mathbf{H}_d^z}{\partial z'^2} \tag{A.4}$$

Expand A.1 by substituting A.3:

$$E_{\mathrm{pot}} = \mu_0 \frac{\mathbf{m}\cdot\mathbf{m}'}{|\mathbf{r}-\mathbf{r}'|^3} - \frac{3(\mathbf{m}\cdot(\mathbf{r}-\mathbf{r}'))\cdot(\mathbf{m}'\cdot(\mathbf{r}-\mathbf{r}'))}{|\mathbf{r}-\mathbf{r}'|^5} \tag{A.5}$$

We precompute some expressions:

$$\begin{aligned} g(\mathbf{r},\mathbf{r}') &\equiv |\mathbf{r}-\mathbf{r}'| && \text{(A.6)}\\ &= \sqrt{(x-x')^2+(y-y')^2+(z-z')^2} && \text{(A.7)}\\ \big(&= \sqrt{(\mathbf{r}-\mathbf{r}')^2}\big) && \text{(A.8)} \end{aligned}$$

$$\begin{aligned} \frac{\partial g(\mathbf{r},\mathbf{r}')}{\partial z'} &= \frac{1}{2\sqrt{(\mathbf{r}-\mathbf{r}')^2}}\cdot 2(-1)(z-z') && \text{(A.9)}\\ &= \frac{1}{\sqrt{(\mathbf{r}-\mathbf{r}')^2}}\cdot -1(z-z') && \text{(A.10)}\\ &= \frac{-(z-z')}{|\mathbf{r}-\mathbf{r}'|} && \text{(A.11)}\\ &= \frac{z'-z}{|\mathbf{r}-\mathbf{r}'|} && \text{(A.12)} \end{aligned}$$

$$\begin{aligned} f &\equiv g^3 && \text{(A.13)}\\ &= |\mathbf{r}-\mathbf{r}'|^3 && \text{(A.14)} \end{aligned}$$

$$\begin{aligned} \frac{\partial f}{\partial z'} &= \frac{\partial f}{\partial g}\cdot\frac{\partial g}{\partial z'} && \text{(A.15)}\\ &= 3\cdot g(\mathbf{r},\mathbf{r}')^2\cdot\frac{\partial g}{\partial z'}(\mathbf{r},\mathbf{r}') && \text{(A.16)}\\ &= 3|\mathbf{r}-\mathbf{r}'|^2\cdot\frac{z'-z}{|\mathbf{r}-\mathbf{r}'|} && \text{(A.17)}\\ &= 3|\mathbf{r}-\mathbf{r}'|(z'-z) && \text{(A.18)} \end{aligned}$$

$$\begin{aligned} \tilde{f} &\equiv \frac{1}{f} && \text{(A.19)}\\ &= \frac{1}{g^3} && \text{(A.20)}\\ &= \frac{1}{|\mathbf{r}-\mathbf{r}'|^3} && \text{(A.21)}\\ &= g^{-3} && \text{(A.22)} \end{aligned}$$

$$\begin{aligned}\frac{\partial \tilde{f}}{\partial z'} &= \frac{\partial \tilde{f}}{\partial g}\frac{\partial g}{\partial z'} && \text{(A.23)}\\ &= -3g^{-4}\cdot\frac{\partial g}{\partial z'} && \text{(A.24)}\\ &= -3\frac{1}{|\mathbf{r}-\mathbf{r}'|^4}\cdot\frac{z'-z}{|\mathbf{r}-\mathbf{r}'|} && \text{(A.25)}\\ &= -3\frac{z'-z}{|\mathbf{r}-\mathbf{r}'|^5} && \text{(A.26)}\end{aligned}$$

$$h \equiv g^5 \qquad \text{(A.27)}$$

so

$$\begin{aligned}\frac{\partial h}{\partial z'} &= \frac{\partial h}{\partial g}\frac{\partial g}{\partial z'} && \text{(A.28)}\\ &= 5g^4\cdot\frac{z'-z}{|\mathbf{r}-\mathbf{r}'|} && \text{(A.29)}\\ &= 5|\mathbf{r}-\mathbf{r}'|^3\cdot(z'-z) && \text{(A.30)}\end{aligned}$$

$$\tilde{h} \equiv g^{-5} \qquad \text{(A.31)}$$

so

$$\begin{aligned}\frac{\partial \tilde{h}}{\partial z'} &= \frac{\partial \tilde{h}}{\partial g}\frac{\partial g}{\partial z'} && \text{(A.32)}\\ &= -5g^{-6}\frac{z'-z}{|\mathbf{r}-\mathbf{r}'|} && \text{(A.33)}\\ &= -5\frac{z'-z}{|\mathbf{r}-\mathbf{r}'|^7} && \text{(A.34)}\end{aligned}$$

Looking at the mixed terms in A.5:

$$\begin{aligned}\Psi(\mathbf{r},\mathbf{r}') &\equiv \big[\mathbf{m}\cdot(\mathbf{r}-\mathbf{r}')\big]\big[\mathbf{m}'\cdot(\mathbf{r}-\mathbf{r}')\big] && \text{(A.35)}\\ &= \big[m_x(x-x')+m_y(y-y')+m_z(z-z')\big]\\ &\quad\cdot\big[m'_x(x-x')+m'_y(y-y')+m'_z(z-z')\big] && \text{(A.36)}\end{aligned}$$

$$\begin{aligned}\frac{\partial \Psi}{\partial z'} &= \big[\mathbf{m}(\mathbf{r}-\mathbf{r}')\big]\cdot\frac{\partial}{\partial z'}\big(m'_x(x-x')+m'_y(y-y')+m'_z(z-z')\big)\\ &\quad+\big[\mathbf{m}'(\mathbf{r}-\mathbf{r}')\big]\cdot\frac{\partial}{\partial z'}\big(m_x(x-x')+m_y(y-y')+m_z(z-z')\big)\\ &= \mathbf{m}(\mathbf{r}-\mathbf{r}')\cdot(-m'_z)+\mathbf{m}'(\mathbf{r}-\mathbf{r}')\cdot(-m_z) && \text{(A.37)}\end{aligned}$$

$$\phi \equiv \frac{\Psi}{|\mathbf{r}-\mathbf{r}'|^5} \tag{A.38}$$

$$= \frac{\Psi}{h} \tag{A.39}$$

$$\frac{\partial \phi}{\partial z'} = \frac{h \cdot \frac{\partial \Psi}{\partial z'} - \Psi \cdot \frac{\partial h}{\partial z'}}{h^2} \tag{A.40}$$

$$= \frac{g^5 \cdot \frac{\partial \Psi}{\partial z'} - \Psi \cdot 5g^3(z'-z)}{g^{10}} \tag{A.41}$$

$$= \frac{\frac{\partial \Psi}{\partial z'}}{g^5} - \frac{5\Psi(z'-z)}{g^7} \tag{A.42}$$

$$= \frac{-\mathbf{m}\cdot(\mathbf{r}-\mathbf{r}')\cdot m'_z - \mathbf{m}'\cdot(\mathbf{r}-\mathbf{r}')m_z}{|\mathbf{r}-\mathbf{r}'|^5} - \frac{5(\mathbf{m}\cdot(\mathbf{r}-\mathbf{r}'))(\mathbf{m}'(\mathbf{r}-\mathbf{r}'))(z'-z)}{|\mathbf{r}-\mathbf{r}'|^7} \tag{A.43}$$

Combining the above to give the first derivative of the dipolar interaction energy as A.5:

$$E_{\text{pot}} = \mu_0 \Big(\frac{\mathbf{m}\cdot\mathbf{m}'}{|\mathbf{r}-\mathbf{r}'|^3} - \frac{3(\mathbf{m}\cdot(\mathbf{r}-\mathbf{r}'))(\mathbf{m}'\cdot(\mathbf{r}-\mathbf{r}'))}{|\mathbf{r}-\mathbf{r}'|^5} \Big) \tag{A.44}$$

With respect to z':

$$\begin{aligned} \frac{\partial E_{\text{pot}}}{\partial z'} &= \mu_0 \Bigg(\frac{\mathbf{m}\cdot\mathbf{m}'\cdot 3(z-z')}{|\mathbf{r}-\mathbf{r}'|^5} \\ &\quad + \frac{3\mathbf{m}\cdot(\mathbf{r}-\mathbf{r}')\cdot m'_z + 3\mathbf{m}'(\mathbf{r}-\mathbf{r}')m_z}{|\mathbf{r}-\mathbf{r}'|^5} \\ &\quad + 3\frac{5(\mathbf{m}\cdot(\mathbf{r}-\mathbf{r}'))(\mathbf{m}'\cdot(\mathbf{r}-\mathbf{r}'))(z'-z)}{|\mathbf{r}-\mathbf{r}'|^7} \Bigg) && \text{(A.45)} \\ &= \mu_0(\mathcal{A}+\mathcal{D}+\mathcal{E}+\mathcal{F}) && \text{(A.46)} \end{aligned}$$

$$\mathcal{A} \equiv \frac{3\mathbf{m}\cdot\mathbf{m}'(z-z')}{|\mathbf{r}-\mathbf{r}'|^5} \tag{A.47}$$

$$\mathcal{D} \equiv \frac{3\mathbf{m}(\mathbf{r}-\mathbf{r}')\cdot m'_z}{|\mathbf{r}-\mathbf{r}'|^5} \tag{A.48}$$

$$\mathcal{E} \equiv \frac{3\mathbf{m}'(\mathbf{r}-\mathbf{r}')\cdot m_z}{|\mathbf{r}-\mathbf{r}'|^5} \tag{A.49}$$

$$\mathcal{F} \equiv \frac{15(\mathbf{m}\cdot(\mathbf{r}-\mathbf{r}'))(\mathbf{m}'\cdot(\mathbf{r}-\mathbf{r}'))(z'-z)}{|\mathbf{r}-\mathbf{r}'|^7} \tag{A.50}$$

$$\mathcal{A} = \frac{\mathcal{B}}{\mathcal{C}} \tag{A.51}$$

To find $\frac{\partial^2 E_{\text{pot}}}{\partial z'^2}$, we need the derivatives of $\mathcal{A}$, $\mathcal{D}$, $\mathcal{E}$ and $\mathcal{F}$:

$$\frac{\partial \mathcal{A}}{\partial z'} = \frac{\mathcal{C} \cdot \frac{\partial \mathcal{B}}{\partial z'} - \mathcal{B} \cdot \frac{\partial \mathcal{C}}{\partial z'}}{\mathcal{C}^2} \tag{A.52}$$

$$= \frac{|\mathbf{r} - \mathbf{r}'|^5 \cdot 3\mathbf{m} \cdot \mathbf{m}'(-1) - 3\mathbf{m} \cdot \mathbf{m}'(z - z') \cdot 5|\mathbf{r} - \mathbf{r}'|^3(z' - z)}{|\mathbf{r} - \mathbf{r}'|^{10}} \tag{A.53}$$

$$= \frac{-3\mathbf{m} \cdot \mathbf{m}'}{|\mathbf{r} - \mathbf{r}'|^5} + \frac{15\mathbf{m} \cdot \mathbf{m}'(z - z')^2}{|\mathbf{r} - \mathbf{r}'|^7} \tag{A.54}$$

$$\frac{\partial \mathcal{D}}{\partial z'} = \frac{\mathcal{C} \cdot \frac{\partial}{\partial z'}(3\mathbf{m} \cdot (\mathbf{r} - \mathbf{r}') \cdot m'_z) - 3\mathbf{m}(\mathbf{r} - \mathbf{r}') \cdot m'_z \cdot 5|\mathbf{r} - \mathbf{r}'|^3(z' - z)}{|\mathbf{r} - \mathbf{r}'|^{10}} \tag{A.55}$$

$$= \frac{3m'_z \frac{\partial}{\partial z'}(m_x(x - x') + m_y(y - y') + m_z(z - z'))}{|\mathbf{r} - \mathbf{r}'|^5}$$

$$+ \frac{15\mathbf{m}(\mathbf{r} - \mathbf{r}')m'_z(z - z')}{|\mathbf{r} - \mathbf{r}'|^7} \tag{A.56}$$

$$= \frac{3m'_z(-m_z)}{|\mathbf{r} - \mathbf{r}'|^5} + \frac{15m'_z(z - z')(\mathbf{r} - \mathbf{r}') \cdot \mathbf{m}}{|\mathbf{r} - \mathbf{r}'|^7} \tag{A.57}$$

$$\frac{\partial \mathcal{E}}{\partial z'} = \frac{3|\mathbf{r} - \mathbf{r}'|^5 \frac{\partial}{\partial z'}(m'_x(x - x') + m'_y(y - y') + m'_z(z - z')) \cdot m_z}{|\mathbf{r} - \mathbf{r}'|^{10}}$$

$$- \frac{3\mathbf{m}'(\mathbf{r} - \mathbf{r}') \cdot m_z \cdot 5|\mathbf{r} - \mathbf{r}'|^3(z' - z)}{|\mathbf{r} - \mathbf{r}'|^{10}} \tag{A.58}$$

$$= \frac{3(-m'_z m_z)}{|\mathbf{r} - \mathbf{r}'|^5} + \frac{15\mathbf{m}'(\mathbf{r} - \mathbf{r}')m_z(z - z')}{|\mathbf{r} - \mathbf{r}'|^7} \tag{A.59}$$

$$r_0 = 15(\mathbf{m} \cdot (\mathbf{r} - \mathbf{r}')) \cdot (\mathbf{m}' \cdot (\mathbf{r} - \mathbf{r}')) \tag{A.60}$$

$$= 15(m_x(x - x') + m_y(y - y') + m_z(z - z'))$$

$$\cdot(m'_x(x - x') + m'_y(y - y') + m_z(z - z')) \tag{A.61}$$

$$\mathcal{F}_1 = r_0(z' - z) \tag{A.62}$$

In the derivative, only the terms with z' matter:

$$\mathcal{F}_0 = \frac{\mathcal{F}_1}{z' - z} \tag{A.63}$$

$$\begin{aligned}\frac{\partial \mathcal{F}_0}{\partial z'} &= \frac{\partial}{\partial z'}\big(15\,\big(m_x(x-x')m'_z(z-z') \\ &\quad +m_y(y-y')m'_z(z-z') \\ &\quad +m_z(z-z')m'_z(z-z')\big)\big)\end{aligned}\tag{A.64}$$

$$\frac{\partial}{\partial z'} = m_z m'_z \cdot 2(z-z')(-1) \tag{A.65}$$

$$\begin{aligned}\frac{\partial \mathcal{F}_0}{\partial z'} &= 15(m_x(x-x')m'_z(-1) \\ &\quad +m_y(y-y')m'_z(-1) \\ &\quad +m_z m'_z \cdot 2(z-z')(-1) \\ &\quad +m_z m'_x(x-x')(-1) \\ &\quad +m_z m'_y(y-y')(-1)) \\ &= -15(\mathbf{m}\cdot(\mathbf{r}-\mathbf{r}')\cdot m'_z + \mathbf{m}'\cdot(\mathbf{r}-\mathbf{r}')\cdot m_z)\end{aligned}\tag{A.66}$$

$$\frac{\partial \mathcal{F}_1}{\partial z'} = \mathcal{F}_0\frac{\partial}{\partial z'}(z'-z) + (z'-z)\frac{\partial \mathcal{F}_0}{\partial z'} \tag{A.67}$$

$$\begin{aligned}&= 15(\mathbf{m}\cdot(\mathbf{r}-\mathbf{r}'))(\mathbf{m}'\cdot(\mathbf{r}-\mathbf{r}'))\cdot 1 \\ &\quad +(z'-z)(-15)(\mathbf{m}\cdot(\mathbf{r}-\mathbf{r}')m'_z + \mathbf{m}'(\mathbf{r}-\mathbf{r}')m_z)\end{aligned}\tag{A.68}$$

$$\begin{aligned}&= 15((\mathbf{m}\cdot(\mathbf{r}-\mathbf{r}')) \\ &\quad +\mathbf{m}\cdot(\mathbf{r}-\mathbf{r}')m'_z(z-z') \\ &\quad +\mathbf{m}'\cdot(\mathbf{r}-\mathbf{r}')m_z(z-z'))\end{aligned}\tag{A.69}$$

$$q \equiv g^7 \tag{A.70}$$

$$= |\mathbf{r}-\mathbf{r}'|^7 \tag{A.71}$$

$$\frac{\partial q}{\partial z'} = \frac{\partial q}{\partial g}\frac{\partial g}{\partial z'} \tag{A.72}$$

$$= 7g^6\frac{\partial g}{\partial z'} \tag{A.73}$$

$$= \frac{7g^6(z'-z)}{g} \tag{A.74}$$

$$= 7|\mathbf{r}-\mathbf{r}'|^5(z'-z) \tag{A.75}$$

$$
\begin{aligned}
\frac{\partial \mathcal{F}}{\partial z'} &= \frac{g^7 \cdot \frac{\partial \mathcal{F}_1}{\partial z'} - \mathcal{F}_1 \cdot \frac{\partial g^7}{\partial z'}}{(g^7)^2} && \text{(A.76)} \\
&= \frac{\frac{\partial \mathcal{F}_1}{\partial z'}}{g^7} - \frac{\mathcal{F}_1 \cdot \frac{\partial g^7}{\partial z'}}{g^{14}} && \text{(A.77)} \\
&= \frac{15}{|\mathbf{r}-\mathbf{r}'|^7} \cdot ((\mathbf{m}(\mathbf{r}-\mathbf{r}'))(\mathbf{m}'(\mathbf{r}-\mathbf{r}')) \\
&\quad +\mathbf{m}(\mathbf{r}-\mathbf{r}')m'_z(z-z') + \mathbf{m}'(\mathbf{r}-\mathbf{r}')m_z(z-z')) \\
&\quad - \frac{15(\mathbf{m}\cdot(\mathbf{r}-\mathbf{r}')\mathbf{m}'(\mathbf{r}-\mathbf{r}')(z'-z)\cdot 7|\mathbf{r}-\mathbf{r}'|^5(z'-z))}{|\mathbf{r}-\mathbf{r}'|^{14}} && \text{(A.78)} \\
&= \frac{15}{|\mathbf{r}-\mathbf{r}'|^7} \cdot ((\mathbf{m}(\mathbf{r}-\mathbf{r}'))(\mathbf{m}'(\mathbf{r}-\mathbf{r}')) \\
&\quad +\mathbf{m}(\mathbf{r}-\mathbf{r}')m'_z(z-z') + \mathbf{m}'(\mathbf{r}-\mathbf{r}')m_z(z-z')) \\
&\quad + \frac{105(\mathbf{m}\cdot(\mathbf{r}-\mathbf{r}')\mathbf{m}'(\mathbf{r}-\mathbf{r}')(z-z')(z'-z))}{|\mathbf{r}-\mathbf{r}'|^{9}} && \text{(A.79)}
\end{aligned}
$$

The second derivative is:

$$
\frac{\partial^2 E_{\text{pot}}}{\partial z'^2} = \mu_0(\mathcal{A}' + \mathcal{D}' + \mathcal{E}' + \mathcal{F}') \tag{A.80}
$$

Where possible, collecting terms and expanding gives:

$$
\begin{aligned}
\frac{\partial^2 E_{\text{pot}}}{\partial z'^2} = \mu_0 \Bigg(& \frac{-3 \cdot \mathbf{m} \cdot \mathbf{m}'}{|\mathbf{r}-\mathbf{r}'|^5} \\
& + \frac{15 \cdot \mathbf{m} \cdot \mathbf{m}'(z-z')^2}{|\mathbf{r}-\mathbf{r}'|^7} \\
& - \frac{6 \cdot m'_z m_z}{|\mathbf{r}-\mathbf{r}'|^5} \\
& + \frac{30(\mathbf{m}\cdot(\mathbf{r}-\mathbf{r}'))m'_z(z-z')}{|\mathbf{r}-\mathbf{r}'|^7} \\
& + \frac{30(\mathbf{m}'\cdot(\mathbf{r}-\mathbf{r}'))m_z(z-z')}{|\mathbf{r}-\mathbf{r}'|^7} \\
& + \frac{15(\mathbf{m}\cdot(\mathbf{r}-\mathbf{r}'))(\mathbf{m}'\cdot(\mathbf{r}-\mathbf{r}'))}{|\mathbf{r}-\mathbf{r}'|^7} \\
& - \frac{105(\mathbf{m}\cdot(\mathbf{r}-\mathbf{r}'))(\mathbf{m}'\cdot(\mathbf{r}-\mathbf{r}'))(z-z')^2}{|\mathbf{r}-\mathbf{r}'|^9} \Bigg)
\end{aligned} \tag{A.81}
$$

This is the final second derivative, which should be proportional to the signal at the tip of the MFM — assuming the MFM tip is a dipole:

$$
\mathbf{m}' = \begin{pmatrix} 0 \\ 0 \\ C \end{pmatrix} \tag{A.82}
$$

Appendix B

Supporting equations for the 3D/1D Monte Carlo method

Since the three-dimensional OOMMF model is not computationally feasible for the antidot system, by assuming two-dimensional layers (see section 6.4) we can extract the coercive field as a function of the radius of the antidots.

By blending these figures for coercivity with a Stoner-Wohlfarth-like (see section 2.6.1) approach and Monte Carlo stochastic mathematical simulation methods we can approximate the three-dimensional system.

The coercive field of the 2D layers B_c is a function of the radius of the holes r with a periodicity of $2R$ defined as r/R. An induced anisotropy can be derived from two points — first, the magnetisation within the sample will prefer to shift between the holes rather than across the empty space inside the holes and second, the holes are arranged hexagonally. By assuming that the magnetisation in the sample is a single-domain, we can describe the induced anisotropy with the following equation:

$$\mathcal{U}_{\text{an}} = K \sin^2(3\phi) \tag{B.1}$$

where ϕ is the angle in the plane between the magnetisation and a symmetry axis.

The left-hand side of figure B.1 shows a polar plot of this antidot-induced anisotropy, with the solid black line emerging from the centre representative of $\phi = 0$. Adding the Zeeman term:

$$\begin{aligned} \mathcal{U}_{\text{tot}} &= \mathcal{U}_{\text{an}} + \mathcal{U}_{\text{Ze}} && \text{(B.2)} \\ &= K \sin^2(3\phi) + mB\cos(\phi) && \text{(B.3)} \end{aligned}$$

If we assume some overall magnetisation direction in the plane such that it is a single domain, we can use the anisotropy term from equation B.1 in the Stoner-

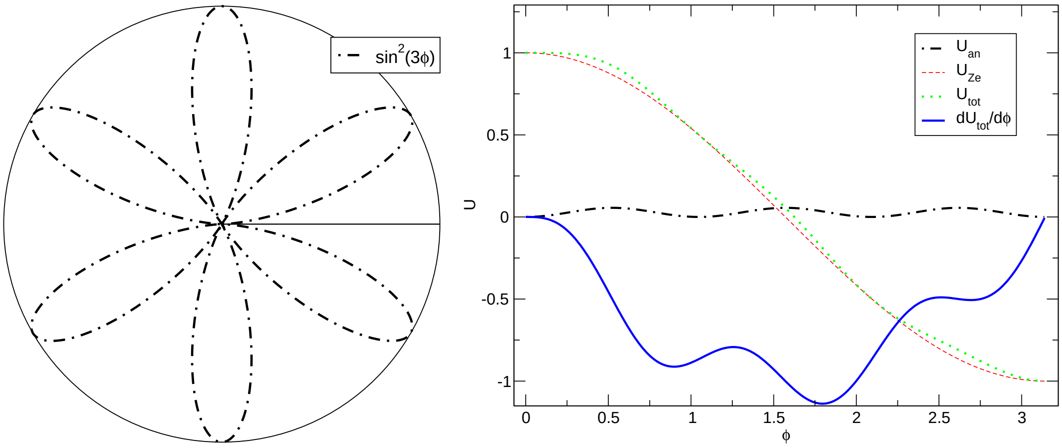

Figure B.1: Polar plot of the anisotropy energy $\mathcal{U}_{\mathrm{an}} = K\sin^2(3\phi)$ when $K = 1$ (left) and reversal condition determination with competing anisotropy energy ($\mathcal{U}_{\mathrm{an}}$) and Zeeman energy ($\mathcal{U}_{\mathrm{Ze}}$) with $B = m = 1$, $K = Bm/18$.

Wohlfarth model described in section 2.6.1. To determine the reversal conditions, we can compute the first derivative of $\mathcal{U}_{\mathrm{tot}}$:

$$\frac{\mathrm{d}\mathcal{U}_{\mathrm{tot}}}{\mathrm{d}\phi} = K2\sin(3\phi)3\cos(3\phi) - mB\sin(\phi) \tag{B.4}$$

The energy barriers dominating the system are shown to be around $\phi = 0$ (figure B.1, right). Expanding sin and cos around zero:

$$\sin(\phi) \approx \phi \tag{B.5}$$

$$\cos(\phi) \approx 1 \tag{B.6}$$

when $\phi \approx 0$.

Inserting this into equation B.4 yields:

$$\frac{\mathrm{d}\mathcal{U}_{\mathrm{tot}}}{\mathrm{d}\phi} \approx 6K3\phi - mB\phi \tag{B.7}$$

If we assume $\phi \neq 0$:

$$K = \frac{mB}{18} \tag{B.8}$$

The right-hand side of figure B.1 shows graphically the resulting energies with $B = 1$, $m = 1$ and $K = Bm/18$.

The value B in equation B.8 is the coercivity B_c obtained from the two-dimensional antidot simulation layer dependent on r/R. Since K and m are the anisotropy constant and the saturation magnetisation respectively for the whole simulated layer rather than per unit volume:

$$K_{(r/R)} = \frac{m_{(r/R)} B_{c_{(r/R)}}}{18} \tag{B.9}$$

These equations, coupled with an exchange energy approximation outlined in equation 6.10, can be used to perform a Monte Carlo simulation on the computed two-dimensional coercivity values. This simulation results in a coercivity oscillation as a function of the thickness of the film which more accurately reflects the experimental results shown in figure 6.3.

Appendix C

Material parameters

material[†]	magnetisation M_s (T (A/m))	exchange parameter A (J/m)	K_1 (J/m^3)	K_2 (J/m^3)
barium iron oxide (1/12/19)[1]	0.48 (3.82×10^{5})	6.3×10^{-12}	4.50×10^{5}	3.00×10^{5}
barium iron oxide (1/12/19) room temperature[2]	0.48 (3.82×10^{5})	6.3×10^{-12}	3.20×10^{5}	1.00×10^{5}
cobalt[1]	1.79 (1.42×10^{6})	3.02×10^{-11}	7.00×10^{5}	1.80×10^{5}
cobalt(3) platinum[3]	1.38 (1.10×10^{6})	9.93×10^{-12}	2.00×10^{6}	0
cobalt iron nickel silicon boron (58/5/10/16/11) amorphous alloy[4]	0.53 (4.22×10^{5})	2.7×10^{-12}	0	0
cobalt platinum[3]	1.01 (8.04×10^{5})	1.01×10^{-11}	4.90×10^{6}	0
cobalt platinum chromium[3]	0.37 (2.94×10^{5})	9.99×10^{-12}	2.00×10^{5}	0
cobalt (room temperature)[2]	1.79 (1.42×10^{6})	3.02×10^{-11}	4.53×10^{5}	1.45×10^{5}
cobalt[1]	1.79 (1.42×10^{6})	3.14×10^{-11}	7.00×10^{5}	1.80×10^{5}
cobalt type 2 (room temperature)[2]	1.79 (1.42×10^{6})	3.14×10^{-11}	4.53×10^{5}	1.45×10^{5}
cobalt[3]	1.76 (1.40×10^{6})	9.99×10^{-12}	4.50×10^{5}	0
iron nickel boron (20/60/20) sputtered[5]	0.56 (4.46×10^{5})	2.1×10^{-12}	0	0
iron(40) nickel(40) boron(20) - amorphous alloy[4]	1.05 (8.36×10^{5})	8.07×10^{-12}	0	0
iron nickel boron (40/40/20) sputtered[5]	1.05 (8.36×10^{5})	5.5×10^{-12}	0	0
iron nickel phosphorous boron (40/40/14/6) amorphous alloy[4]	0.8 (6.37×10^{5})	3.1×10^{-12}	0	0
iron nickel boron (60/20/20) sputtered[5]	1.46 (1.16×10^{6})	7.9×10^{-12}	0	0
iron silicon niobium copper boron (73.5/13.5/3/1/9) nanocrystalline alloy[6]	1.2 (9.55×10^{5})	1×10^{-11}	0	0
iron boron (80/20) - amorphous alloy[4]	1.6 (1.27×10^{6})	5×10^{-12}	0	0
iron boron (80/20) sputtered[5]	1.56 (1.24×10^{6})	5.4×10^{-12}	0	0
iron palladium[3]	1.38 (1.10×10^{6})	1.03×10^{-11}	1.80×10^{6}	0
iron platinum (maximum)[3]	1.43 (1.14×10^{6})	1.54×10^{-11}	1.00×10^{7}	0
iron platinum (minimum)[3]	1.43 (1.14×10^{6})	1.02×10^{-11}	6.60×10^{6}	0
iron - amorphous alloy[4]	2.185 (1.74×10^{6})	2.07×10^{-11}	0	0
manganese aluminium[3]	0.7 (5.57×10^{5})	1.02×10^{-11}	1.70×10^{6}	0
neodymium iron boron (2/14/1)[1]	1.61 (1.28×10^{6})	7.3×10^{-12}	-1.80×10^{7}	4.80×10^{7}
neodymium iron boron (2/14/1) room temperature[2]	1.61 (1.28×10^{6})	7.3×10^{-12}	4.30×10^{6}	6.50×10^{5}
neodymium iron boron(2/14/1) type 2[1]	1.61 (1.28×10^{6})	8.4×10^{-12}	-1.80×10^{7}	4.80×10^{7}
neodymium iron boron (2/14/1) type 2 (room temperature)[2]	1.61 (1.28×10^{6})	8.4×10^{-12}	4.30×10^{6}	6.50×10^{5}
nickel[1]	0.62 (4.93×10^{5})	7.2×10^{-12}	-1.20×10^{5}	3.00×10^{4}

---

[1] *Micromagnetism and the microstructure of ferromagnetic solids*, pp. 17-22, first edition, Kronmüller and Fähnle

[2] as [1]; figures are for materials at room temperature

material[†]	magnetisation M_s (T (A/m))	exchange parameter A (J/m)	K_1 (J/m^3)	K_2 (J/m^3)
nickel (3) iron[1]	1.1 (8.75×10^{5})	7.1×10^{-12}	0	0
permalloy (50/50)[7]	1.39 (1.11×10^{6})	5.85×10^{-12}	0	0
permalloy (80/20)[8]	1.0 (7.96×10^{5})	1.3×10^{-11}	0	0
nickel (room temperature)[2]	0.62 (4.93×10^{5})	7.2×10^{-12}	-4.50×10^{3}	-2.50×10^{3}
nickel - amorphous alloy[4]	0.62 (4.93×10^{5})	8.5×10^{-12}	0	0
nickel (type 2)[1]	0.62 (4.93×10^{5})	8.5×10^{-12}	-1.20×10^{5}	3.00×10^{4}
nickel (type 2) room temperature[2]	0.62 (4.93×10^{5})	8.5×10^{-12}	-4.50×10^{3}	-2.50×10^{3}
praseodymium iron boron (2/14/1)[1]	1.56 (1.24×10^{6})	1.2×10^{-11}	2.40×10^{7}	-7.00×10^{6}
praseodymium iron boron (2/14/1) room temperature[2]	1.56 (1.24×10^{6})	1.2×10^{-11}	5.60×10^{6}	0
samarium (2) cobalt (17)[1]	1.29 (1.03×10^{6})	1.4×10^{-11}	6.50×10^{6}	0
samarium(2) cobalt(17) at room temperature[2]	1.29 (1.03×10^{6})	1.4×10^{-11}	4.20×10^{6}	0
samarium iron nitrogen (2/17/3)[1]	1.56 (1.24×10^{6})	1.2×10^{-11}	1.20×10^{7}	3.00×10^{6}
samarium iron nitrogen (2/17/3) room temperature[2]	1.56 (1.24×10^{6})	1.2×10^{-11}	8.60×10^{6}	1.90×10^{6}
samarium cobalt(5)[1]	1.05 (8.36×10^{5})	1.2×10^{-11}	2.60×10^{7}	0
samarium cobalt(5) room temperature[2]	1.05 (8.36×10^{5})	1.2×10^{-11}	1.70×10^{7}	0
alpha iron[2]	2.185 (1.74×10^{6})	2.07×10^{-11}	5.20×10^{4}	-1.80×10^{4}
alpha iron at room temperature[2]	2.185 (1.74×10^{6})	2.07×10^{-11}	4.80×10^{4}	-1.00×10^{4}
alpha iron (type 2) room temperature[2]	2.185 (1.74×10^{6})	2.28×10^{-11}	5.20×10^{4}	-1.80×10^{4}
alpha iron room temperature[2]	2.185 (1.74×10^{6})	2.2×10^{-11}	4.80×10^{4}	-1.80×10^{4}
gamma magnetite[9]	0.61 (4.85×10^{5})	1.32×10^{-11}	-1.36×10^{4}	0

Table C.1: Properties of ferromagnetic materials

[3] Klemmer and Weller, (*Scholz*, 2003)

[4] as [1]; figures are for an amorphous alloy

[5] as [1]; figures are for sputtered material

[6] as [1]; figures are for nanocrystalline alloy

[7] Alexander Zhukov, School of Physics and Astronomy, University of Southampton

[8] *Smith, Markham and LaTourette* (1989)

[9] *Afremov and Panov* (1998)

[†] Note that where the temperature is not specified, measurements have been taken at low temperature. Neodymium iron boron (2/14/1) was measured at 20K, all others at 4.2K.

Appendix D

CGS and SI (MKS) unit systems

description	cgs	unit	SI (mks)	unit	factor
acceleration	galileo	Gal	metre per second squared	$\mathrm{m \cdot s^{-2}}$	0.01
dynamic viscosity	poise	P	pascal second	$\mathrm{Pa \cdot s}$	0.1
electric charge	franklin	Fr	coulomb	C	3.34×10^{-10}
electric current	biot	Bi	ampere	A	10
electric dipole moment	debye	D	coulomb metre	$\mathrm{C \cdot m}$	3.34×10^{-30}
energy (work)	erg		joule	J	10^{-7}
force	dyne	dyn	newton	N	10^{-5}
heat energy	calorie	cal	joule	J	4.187
heat transmission	langley		kilojoule per square metre	$\mathrm{kJ \cdot m^{-2}}$	41.84
illumination	phot	ph	lux	lx	10^{4}
kinematic viscosity	stokes	St	square metres per second	$\mathrm{m^{2} \cdot s^{-1}}$	10^{-4}
luminance	lambert	Lb	candela per square metre	$\mathrm{cd \cdot m^{-2}}$	3183.1
	stilb	sb			10^{4}
magnetic dipole moment	emu		ampere square metre	$\mathrm{A \cdot m^{2}}$	10^{-3}
magnetic field strength	oersted	Oe	ampere per metre	$\mathrm{A \cdot m^{-1}}$	79.577
magnetic flux	line	li	weber	Wb	10^{-8}
	maxwell	Mx			10^{-8}
	unit pole				1.257×10^{-7}
magnetic flux density	gauss	G	tesla	T	10^{-4}
magnetomotive force	gilbert	Gi	ampere	A	0.796
permeability	darcy		square metre	$\mathrm{m^{2}}$	0.987×10^{-12}
pressure	barye	ba	pascal	Pa	0.1
wave number	kayser	K	per metre	$\mathrm{m^{-1}}$	100

Table D.1: The centimetre-gram-seconds (CGS) and the metre-kilogram-seconds (SI) unit systems. To convert from one system to the other, cgs unit × factor = mks unit. Data from *Purcell* (1985) and *Jackson* (1999)

Appendix E

Complete simulation process

This section discusses the complete simulation process, centred around the diagram in figure E.1. This diagram shows the major supporting libraries, compilers, interpreters, scripts, data stores and outputs of the method.

E.1 Notation

- *Hexagonal* boxes with green text indicate one of the two simulation packages involved: *OOMMF* for the finite difference method, or *magpar* for the hybrid finite element/boundary element method.
- *Diamonds* containing red text show a source compiler or a script interpreter, such as *gcc* or *Python*.
- *Parallelograms* show a fundamental library necessary for the compilation of one of the simulation packages.
- *Ellipses* with purple text show an intermediate data set necessary for "gluing" components together.
- *Boxes* with blue text indicate a complex custom application designed to convert or otherwise handle the input and output of one application or library.
- *Trapezoids* with grey text demonstrate a presentation output file; numerical data
  would be a hysteresis loop, for example, whereas graphical data would be a magnetisation visualisation.
- *Ellipsoids* with red text show a supporting external application necessary for visualisation, pre- or post-processing or runtime.

Conversion between data sets or to interpret a data set as the input of another program is performed by a custom application not necessarily indicated on the diagram in figure E.1 for clarity.

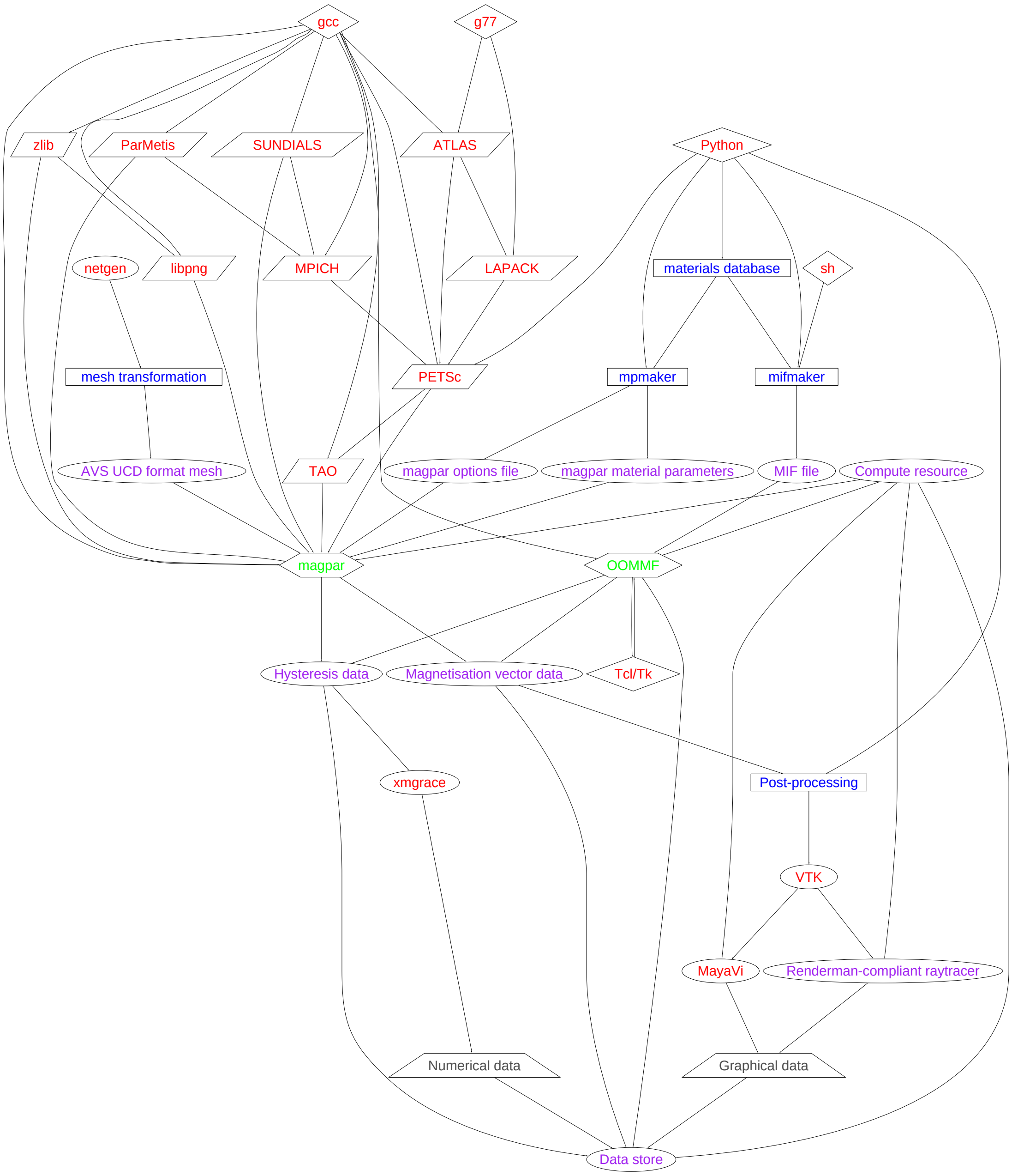

Figure E.1: The complete simulation process, from supporting libraries and compilers to visualisation and post-processing

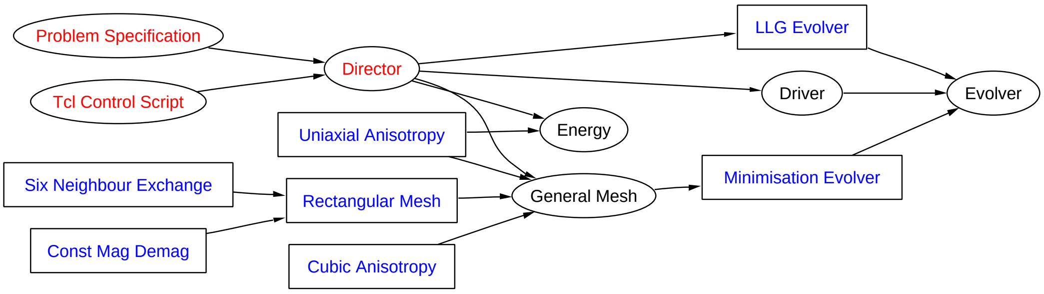

Figure E.2: The *OOMMF* extensible solver framework. Blue items in boxes indicate extensible areas

The build of the hybrid finite element/boundary element package *magpar* is much more complicated than that of its finite difference peer, *OOMMF*. *OOMMF* is available from the NIST website as either a source code package with a straightforward build process or as a precompiled binary application for many architectures and operating systems, such as GNU/Linux or Microsoft Windows. The framework of the three-dimensional micromagnetic problem solver, *Oxs* (the *O*OMMF *E*xtensible *S*olver), is shown in figure E.2. The blue items in boxes here show areas which can be straightforwardly extended to include, for example, a twenty-six neighbour exchange energy contribution rather than the standard six neighbour exchange provided as standard with *OOMMF*. *Oxs* provides a powerful mechanism for extending this micromagnetics package.

Conversely, *magpar* is dependent on many highly optimised mathematics libraries which have been developed by different organisations and individuals for many years. While the result of each of these is a library which is extremely powerful with respect to its individual application (linear algebra, matrix transformation, differential equation solvers), compatibility and ease-of-use suffer. Although these issues will be addressed in due course, it alienates many members of the physics community as one must be familiar with software development in a UNIX-like environment to successfully use the software when provided in this form.

In theory, of course, binaries of *magpar* could be provided just as for *OOMMF*, however given the automatic calibration and tuning of the mathematical libraries involved, performance would be adversely affected, and there is no guarantee that the results would be accurate. Taking advantage of the features provided by one particular architecture can introduce dangerous imprecision when run on another similar architecture, especially when considering floating point computation cancellation and round-off errors (*Schulte and Swartzlander*, 2000).

Appendix F

Constructive solid geometries

In order to create micromagnetic problem input sources, such as MIF files for *OOMMF* or to describe boundaries for *magpar*'s finite element meshes, we need to define the basic geometry of the problem.

A basic geometry is one described by a simple mathematical equation, and these are generally accepted by three-dimensional graphics modellers to be *primitives* — constructive solid geometries (CSGs) (see figure F.1). The primitives can be considered to be the set of spheres, torii, cylinders, cuboids, pyramids and cones, as well as the associated two-dimensional shapes. By adding or removing conditions for satisfying the equations, the shape can be modified. For example, if one considers a sphere where the volume conditions are defined by:

$$x^2 + y^2 + z^2 \quad \leq \quad 1 \tag{F.1}$$

where x, y and z are between -1 and 1 then it is straightforward to modify this such that the conditions in equation F.1 are met and $z \leq 0$, then a half-sphere is produced. This could be called a *Boolean* shape because the resultant geometry shows a "negative" cuboid has been cut away from the sphere. A section of a sphere could be created as though two cuboids have been subtracted from it by, in addition to satisfying the above equations, satisfying $z \geq -0.5$. If this is satisfied, and the conditions for a cone:

$$x^2 + y^2 \quad \leq \quad \left(\frac{z+1}{2}\right)^2 \tag{F.2}$$

are also met, then a section of a cone results and so forth. By continuing in this fashion, it is possible to use a handful of primitives to build more complex objects and subsequently arrays of these objects (see figure F.1).

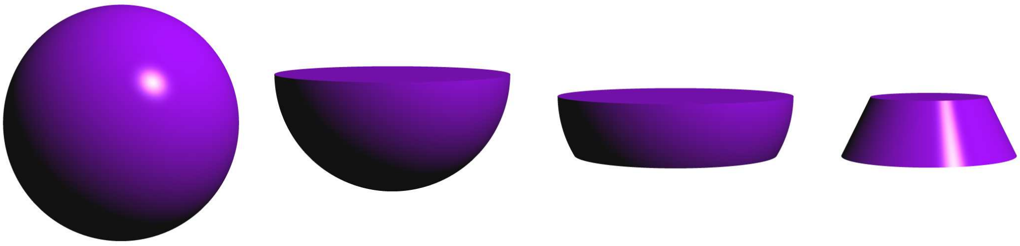

Figure F.1: Simple constructive solid geometries as described by the equations in 3.3. From left to right: sphere, half-sphere, quarter-sphere and quarter-cone

Bibliography

Afremov LL and Panov AV. Magnetic states and hysteresis properties of small magnetite particles. *Physics of Metals and Metallography*, **86**(3), 269–275 (1998).

Aharoni A. Magnetostatic energy of a ferromagnetic sphere. *Journal of Applied Physics*, **51**(11), 5906–5908 (1980).

Aharoni A. Magnetisation distribution in an ideally soft sphere. *Journal of Applied Physics*, **55**(4), 1049–1051 (1983).

Aharoni A. *Introduction to the theory of Ferromagnetism*. Oxford Science Publications, 2nd edition (2000).

Albrecht M, Ganesan S, Rettner CT, Moser A, Best ME, White RL and Terris BD. Patterned perpendicular and longitudinal media: a magnetic recording study. *IEEE Transactions on Magnetics*, **39**(5), 2323–2325 (2003).

Argyres PN. Theory of the Faraday and Kerr effects in ferromagnetics. *Physical Review*, **97**(2), 334–345 (1955).

Baibich MN, Broto JM, Fert A, van Dau FN, Petroff F, Etienne P, Creuzet G, Friederich A and Chazelas J. Giant magnetoresistance of (001)Fe/(001)Cr magnetic superlattices. *Physical Review Letters*, **61**, 2472–2475 (1988).

Balay S, Buschelman K, Gropp WD, Kaushik D, Knepley M, McInnes LC, Smith BF and Zhang H. PETSc users manual. Technical Report ANL-95/11 - Revision 2.1.5, Argonne National Laboratory (2002).

Balay S, Gropp WD, McInnes LC and Smith BF. Efficient management of parallelism in object oriented numerical software libraries. In E Arge, AM Bruaset and HP Langtangen, editors, *Modern Software Tools in Scientific Computing*, pages 163–202. Birkhauser Press (1997).

Ball S. *Web Tcl Complete*. McGraw-Hill (1999).

Barclay T, Chong W and Gray J. A quick look at serial ATA disk performance. Technical Report MSR-TR-2003-70, Microsoft Research, Microsoft Corporation, One Microsoft Way, Redmond, WA 98052 (2003).

Barthelmeß M, Pels C, Thieme A and Meier G. Stray fields of domains in permalloy microstructures — measurements and simulations. *Journal of Applied Physics*, **95**(10), 5641–5645 (2004).

Barthelmeß M, Thieme A, Eiselt R and Meier G. Stray fields of iron electrodes for spin-polarized transport. *Journal of Applied Physics*, **93**, 8400 (2003).

Bartlett PN, Baumberg JJ, Birkin PR, Ghanem MA and Netti MC. Highly ordered macroporous gold and platinum films formed by electrochemical deposition through templates assembled from submicron diameter monodisperse polystyrene spheres. *Chemistry of Materials*, **14**, 2199–2208 (2002).

Bartlett PN, Birkin PR and Ghanem MA. Electrochemical deposition of macroporous platinum, palladium and cobalt films using polystyrene latex sphere templates. *Chemical Communications*, **17**, 1671–1672 (2000).

Bartlett PN, Ghanem MA, de Groot PAJ and Zhukov AA. Method of producing ordered arrays (2003a). UK Patent Application GB 0310498.1.

Bartlett PN, Ghanem MA, El Hallag IS, de Groot PAJ and Zhukov AA. Electrochemical deposition of macroporous magnetic networks using colloidal templates. *Journal of Materials Chemistry*, **13**(10), 2596–2602 (2003b).

BBC. William Gilbert. `http://www.bbc.co.uk/history/historic_figures/gilbert_william.shtml` (2004).

Bennett Goldberg I. 27 bits are not enough for 8-digit accuracy. *Communications of the ACM*, **10**(2), 105–106 (1967).

Bertram HN. *Theory of Magnetic Recording*. Cambridge University Press (1994).

Binnig G, Quate CF and Gerber C. Atomic force microscope. *Physical Review Letters*, **56**(9), 930–933 (1986).

Binnig G and Rohrer H. The scanning tunneling microscope. *Scientific American*, **253**, 40–46 (1985).

Binnig G, Rohrer H, Gerber C and Weibel E. Surface studies by scanning tunnelling microscopy. *Physical Review Letters*, **49**(1), 57–61 (1982).

Binnig G, Rohrer H, Gerber C and Weibel E. 7 x 7 reconstruction on Si(111) resolved in real space. *Physical Review Letters*, **50**(2), 120–123 (1983).

Blundell S. *Magnetism in Condensed Matter*. Oxford University Press, 1st edition (2001).

Boardman RP, Fangohr H, Fairman MJ, Zimmermann J, Zhukov AA, Cox SJ and de Groot PAJ. Micromagnetic modelling of ferromagnetic cones. *Physical Review B* (2005a). Submitted.

Boardman RP, Fangohr H, Goncharov AV, Zhukov AA, de Groot PAJ and Cox SJ. Micromagnetic simulation of ferromagnetic part-spherical particles. *Journal of Applied Physics*, **95**(11), 7037–7039 (2004).

Boardman RP, Zimmermann J, Fangohr H, Zhukov AA and de Groot PAJ. Micromagnetic simulation studies of ferromagnetic part-spheres. *Journal of Applied Physics*, **97**(10), 10E305 (2005b).

Bogomolov VN, Gaponenko SV, Germanenko IN, Kapitonov AM, Petrov EP, Gaponenko NV, Prokofiev AV, Ponyavina AN, Silvanovich NI and Samoilovich SM. Photonic band gap phenomenon and optical properties of artificial opals. *Physical Review E*, **55**(6), 7619–7625 (1997).

Brown Jr. WF. *Micromagnetics*. Wiley Interscience, New York (1963).

C. H. Stapper J. Micromagnetic solutions for ferromagnetic spheres. *Journal of Applied Physics*, **40**(2), 798–802 (1969).

Chou SY. Patterned magnetic nanostructures and quantized magnetic disks. *Proceedings of the IEEE*, **85**(4), 652–671 (1997).

Chou SY, Krauss PR and Kong L. Nanolithographically defined magnetic structures and quantum magnetic disk. *Journal of Applied Physics*, **79**(8), 6101–6106 (1996).

Cowburn RP. Property variation with shape in magnetic nanoelements. *Journal of Physics D: Applied Physics*, **33**, R1–R16 (2000).

Cowburn RP, Adeyeye AO and Bland JAC. Magnetic domain formation in lithographically defined antidot permalloy arrays. *Applied Physics Letters*, **70**(17), 2309–2311 (1997).

Cowburn RP, Adeyeye AO and Welland ME. Controlling magnetic ordering in coupled nanomagnet arrays. *New Journal of Physics*, **1**, 16 (1999a).

Cowburn RP, Koltsov DK, Adeyeye AO, Welland ME and Tricker DM. Single-domain circular nanomagnets. *Physical Review Letters*, **83**(5), 1042–1045 (1999b).

Curie P. *Annales de Chimie et Physique*, **5**(289) (1895).

Dahlberg ED and Proksch R. Magnetic microscopies: the new additions. *Journal of Magnetism and Magnetic Materials*, **200**, 720–728 (1999).

Dao N, Whittenburg SL and Cowburn RP. Micromagnetics simulation of deep-submicron supermalloy disks. *Journal of Applied Physics*, **90**(10), 5235–5237 (2001).

de Groot PAJ. Private communication (2005).

Demmel J. Underflow and the reliability of numerical software. *SIAM Journal of Scientific and Statistical Computing*, **5**(4), 887–919 (1984).

Denkov ND, Velev OD, Kralchevsky PA, Ivanov IB, Yoshimura H and Nagayama K. Two-dimensional crystallisation. *Nature*, **361**(6407), 26 (1993).

Donahue MJ and McMichael RD. Exchange energy representational in computational micromagnetics. *Physica B*, **233**, 272–278 (1997).

Donahue MJ and McMichael RD. Exchange energy representations in computational micromagnetics. Technical report, National Institute of Standards and Technology, Gaithersburg, MD, USA (2002).

Donahue MJ and Porter DG. *OOMMF User's Guide*. National Institute of Standards and Technology, Gaithersburg, MD (1999). Interagency Report NISTIR 6376.

Eisenstein I and Aharoni A. Magnetisation curling in a sphere. *Journal of Applied Physics*, **47**(1), 321–328 (1975).

Flynt C. *Tcl/Tk for Real Programmers*. Academic Press International (1999).

Fruchart O, Nozières JP, Wernsdorfer W, Givord D, Rousseaux F and Decanini D. Enhanced coercivity in submicrometre-sized ultrathin epitaxial dots with inplane magnetisation. *Physical Review Letters*, **82**, 1305–1308 (1999).

Gau H, Herminghaus S, Lenz P and Lipowsky R. Liquid morphologies on structured surfaces: from microchannels to microchips. *Science*, **283**, 46–49 (1999).

Ghanem MA, Bartlett PN, de Groot PAJ and Zhukov A. A double templated electrodeposition method for the fabrication of arrays of metal nanodots. *Electrochemistry Communications*, **6**(5), 447–453 (2004).

Gilbert TL. A Lagrangian formulation of gyromagnetic equation of the magnetization field. *Physical Review*, **100**, 1243 (1955).

Gilbert W and Mottelay PF. *De Magnete*. Dover Publications (1600, 1991).

Goldberg D. What every computer scientist should know about floating-point arithmetic. *Computing Surveys* (1991).

Gubbiotti G, Carlotti G, Nizzoli F, Zivieri R, Okuno T and Shinjo T. Magnetic properties of submicron circular permalloy dots. *IEEE Transactions on Magnetics*, **38**(5), 2532–2534 (2002).

Ha JK, Hertel R and Kirschner J. Configurational stability and magnetization processes in submicron permalloy disks. *Physical Review B*, **67**, 064418 (2003).

Hehn M, Ounadjela K, Bucher JP, Rousseaux F, Decanini D, Bartenlian B and Chappert C. Nanoscale magnetic domains in mesoscopic magnets. *Science*, **272**, 1782–1785 (1996).

Hetland ML. *Practical Python*. Apress, 1st edition (2002).

Hoinville J, Bewick A, Gleeson D, Jones R, Kasyutich O, Mayes E, Nartowski A, Warne B, Wiggins J and Wong K. High density magnetic recording on protein-derived nanoparticles. *Journal of Applied Physics*, **93**, 7187–7189 (2003).

Huang Z. High accuracy numerical method of thin-film problems in micromagnetics. Technical report, Department of Mathematical Sciences, Tsinghua University, Beijing, 100084, P. R. China (2003).

Hubert A and Schäfer R. *Magnetic Domains*. Springer - Verlag Berlin Heidelberg (1998, 2000).

Hug HJ, Stiefel B, van Schendel PJA, Moser A, Hofer R, Martin S, Güntherodt HJ, Porthun S, Abelmann L, Lodder JC, Bochi G and O'Handley RC. Quantitative magnetic force microscopy of perpendicularly magnetized samples. *Journal of Applied Physics*, **83**(11), 5609–5619 (1998).

IBM. Alternative Storage. `http://www.almaden.ibm.com/sst/storage/alternative_storage/pm.shtml` (2002). IBM Almaden Research Centre.

IEEE. 754-1985 IEEE standard for binary floating-point arithmetic. Technical report, Institute of Electrical and Electronics Engineers (1985).

Jackson JD. *Classical Electrodynamics*. Wiley, 3rd edition (1999).

Kittel C. *Introduction to Solid State Physics*. John Wiley and Sons, Inc., 7th edition (1996).

Knuth DE. *The Art of Computer Programming: Seminumerical Algorithms*, volume 2. Addison-Wesley, 3rd edition (1998).

Koltsov DK, Cowburn RP and Welland ME. Micromagnetics of ferromagnetic equilateral triangular prisms. *Journal of Applied Physics*, **88**(9), 5315–5317 (2000).

Kronmüller H and Fähnle M. *Micromagnetism and the Microstructure of Ferromagnetic Solids*. Cambridge University Press, 1st edition (2003).

Lam J. Magnetic hysteresis of a rectangular lattice of interacting single-domain ferromagnetic spheres. *Journal of Applied Physics*, **72**(12), 5792–5798 (1992).

Landau LD and Lifshitz EM. On the theory of the dispersion of magnetic permeability in ferromagnetic bodies. *Physikalische Zeitschrift der Sowjetunion*, **8**(2), 153–169 (1935).

Li SP, Natali M, Lebib A, Péin A, Chen Y and Xu YB. Magnetic nanostructure fabriction by soft lithography and vortex-single domain transition in co dots. *Journal of Magnetism and Magnetic Materials*, **241**, 447–452 (2002).

Litzkow M. Remote UNIX - turning idle workstations into cycle servers. In *Usenix Summer Conference*, pages 381–384 (1987).

Litzkow M, Livny M and Mutka M. Condor - a hunter of idle workstations. In *8th International Conference of Distributed Computing Systems*, pages 104–111 (1988).

Lutz M and Ascher D. *Learning Python*. O'Reilly, 2nd edition (2003).

Martín JL, Nogués J, Liu K, Vicent JL and Schuller IK. Ordered magnetic nanostructures: fabrication and properties. *Journal of Magnetism and Magnetic Materials*, **256**(1-3), 449–501 (2003).

Mayes E, Bewick A, Gleeson D, Hoinville J, Jones R, Kasyutich O, Nartowski A, Warne B, Wiggins J and Wong KKW. Biologically derived nanomagnets in self-organized patterned media. *IEEE Transactions on Magnetics*, **39**, 624–627 (2003).

McVitie S, White GS, Scott J, Warin P and Chapman JN. Quantitative imaging of magnetic domain walls in thin films using Lorentz and magnetic force microscopies. *Journal of Applied Physics*, **90**(10), 5220–5226 (2001).

O'Handley RC. *Modern Magnetic Materials: Principles and Applications*. John Wiley and Sons, Inc. (1999).

Paine TO, Mendelsohn LI and Luborsky FE. Effect of shape anisotropy on the coercive force of elongated single-magnetic-domain iron particles. *Physical Review*, **100**, 1055–1059 (1955).

Pixar. *The RenderMan Interface Specification v3.1* (1989).

Pixar. *The RenderMan Interface Specification v3.2* (2000).

Purcell EM. *Electricity and Magnetism*, volume 2. Berkeley Physics, 2nd edition (1985).

Raines P and Tranter J. *Tcl/Tk in a nutshell*. O'Reilly and Associates, Inc. (1999).

Ramachandran P. MayaVi: a free tool for CFD data visualisation. In *4th Annual CFD Symposium, Aeronautical Society of India* (2001).

Ramey C. Bash website (2003). `www.gnu.org/software/bash/bash.html`.

Ridge D, Becker D, Merkey P and Sterling T. Beowulf: Harnessing the power of parallelism in a pile-of-PCs. *Proceedings, IEEE Aerospace* (1997).

Ross CA. Patterned magnetic recording media. *Annual Review of Materials Research*, **31**, 203–235 (2001).

Ross CA, Farhoud M, Hwang M, Smith HI, Redjdal M and Humphrey FB. Micromagnetic behaviour of conical ferromagnetic particles. *Journal of Applied Physics*, **89**(2), 1310–1319 (2001).

Rugar D, Marmin HJ, Guethner P, Lambert SE, Stern JE, McFadyen I and Yogi T. Magnetic force microscopy: general principles and application to longitudinal recording media. *Journal of Applied Physics*, **68**(3), 1169–1183 (1990).

Sáenz JJ, Garcia N, Grütter P, Meyer E, Heinzelmann H, Wiesendanger R, Rosenthaler L, Hidber HR and Güntherodt HJ. Observation of magnetic forces by the atomic force microscope. *Journal of Applied Physics*, **62**(10), 4293–4295 (1987).

Sanders IL, Kane SM and Cohen MS. 1μm bubble permalloy contiguous disk devices. *Journal of Applied Physics*, **52**(3), 2374–2376 (1981).

Schöberl J. *Netgen 4.3 User's Guide*. `http://www.hpfem.jku.at/netgen/ng4.pdf` (2003).

Scholz W. *Scalable parallel micromagnetic solvers for magnetic nanostructures*. Ph.D. thesis, Fakultät für Naturwissenschaften und Informatik, Technische Universität Wien (2003).

Scholz W, Fidler J, Schrefl T, Süß D, Dittrich R, Forster H and Tsiantos V. Scalable parallel micromagnetic solvers for magnetic nanostructures. *Computational Materials Science*, **28**, 366–383 (2003a).

Scholz W, Guslienko KY, Novosad V, Süß D, Schrefl T, Chantrell RW and Fidler J. Transition from single-domain to vortex state in soft magnetic cylindrical nanodots. *Journal of Magnetism and Magnetic Materials*, **266**, 155–163 (2003b).

Schroeder WJ, Martin KM and Lorensen WE. The design and implementation of an object-oriented toolkit for 3D graphics and visualization. In R Yagel and GM Nielson, editors, *IEEE Visualization '96*, pages 93–100 (1996).

Schroeder WJ, Martin KM and Lorensen WE. *The Visualisation Toolkit (VTK): An object-oriented approach to 3D graphics*. Pearson Education (1997).

Schulte MJ and Swartzlander Jr. EE. A family of variable-precision interval arithmetic processors. *IEEE Transactions on Computers*, **49**(5), 1–11 (2000).

Seberino C and Bertram HN. Concise, efficient three-dimensional fast multipole method for micromagnetics. *IEEE Transactions on Magnetics*, **37**, 1078–1086 (2001).

Skomski R and Coey JMD. *Permanent Magnetism*. Series in Condensed Matter Physics. Institute of Physics (1999).

Smith C. *[incr Tcl/Tk] from the ground up*. Osborne (2000).

Smith N, Markham D and LaTourette D. Magnetoresistive measurement of the exchange constant in varied-thickness permalloy films. *Journal of Applied Physics*, **65**(11), 4362–4365 (1989).

Snir M, Otto SW, Huss-Lederman S, Walker DW and Dongarra J. *MPI: the complete reference*. MIT Press (1995).

Stoner EC and Wohlfarth EP. A mechanism of magnetic hysteresis in heterogeneous alloys. *Philosophical Transactions of the Royal Society London*, **A240**, 599–642 (1948).

Süß D. *Micromagnetic simulations of antiferro- and ferromagnetic structures for magnetic recording*. Ph.D. thesis, Fakultät für Naturwissenschaften und Informatik, Technischen Universität Wien (2002).

Tarnopolsky GJ. Hard disk drive capacity at high magnetic areal density. *IEEE Transactions on Magnetics*, **40**(1), 301–306 (2004).

Teherani S, Chen E, Durlam M, de Herrera M, Slaughter JM, Shi J and Kerszykowski E. High density submicron magnetoresistive random access memory. *Journal of Applied Physics*, **85**(8), 5822–5827 (1999).

Tsang C, Chen MM and Yogi T. Gigabit-density magnetic recording. *Proceedings of the IEEE*, **81**(9), 1344–1359 (1993).

Tsang C, Chen MM, Yogi T and Ju K. Gigabit density recording using dual-element mr/inductive heads on thin-film disks. *IEEE Transactions on Magnetics*, **26**(5), 1689–1693 (1990).

Turner PJ. Grace home. http://plasma-gate.weizmann.ac.il/Grace/ (1995).

van Rossum G. Python website (2003). `http://www.python.org`.

van Rossum G and Drake FL. *Python Reference Manual*. PythonLabs, Virginia, USA (2001).

Van Roy W, Carpi EL, Van Hove M, Van Esch A, Bogaerts R, De Boeck J and Borghs G. Study of the demagnetisation and optimisation of the magnetic field of perpendicular ferromagnetic thin films using sub-μm lithography. *Journal of Magnetism and Magnetic Materials*, **121**(1-3), 197–200 (1993).

Velev OD and Kaler EW. In situ assembly of colloidal particles into miniaturised biosensors. *Langmuir*, **15**(11), 3696–3698 (1999).

Vlasov YA, Bo XZ, Sturm JC and Norris DJ. On-chip natural assembly of silicon photonic bandgap crystals. *Nature*, **414**, 289–293 (2001).

Wachowiak A, Wiebe J, Bode M, Pietzsch O, Morgenstern M and Wiesendanger R. Direct observation of internal spin structure of magnetic vortex cores. *Science*, **298**, 577–580 (2002).

Walker D. Standards for message passing in a distributed memory environment. Technical report, Oak Ridge National Laboratory (1992).

Welch BB. *Practical programming in Tcl and Tk*. Prentice Hall PTR, 3rd edition (1999).

Wood RW. The feasibility of magnetic recording at 1 terabit per square inch. *IEEE Transactions on Magnetics*, **36**(1), 36–42 (2000).

Wood RW, Miles J and Olson T. Recording technologies for terabit per square inch systems. *IEEE Transactions on Magnetics*, **38**(4), 1711–1718 (2002).

Xu L, Zhou WL, Frommen C, Baughman RH, Zakhidov AA, Malkinski L, Wang JQ and Wiley JB. Electrodeposited nickel and gold nanoscale metal meshes with potentially interesting photonic properties. *Chemical Communications*, **12**, 997–998 (2000).

Zhukov AA. Private communication (2004).

Zhukov AA, Ghanem MA, Goncharov AV, Boardman RP, Novosad V, Karapetrov G, Fangohr H, Bartlett PN and de Groot PAJ. Oscillatory thickness dependence of the coercive field in magnetic 3d anti-dot arrays. *Physical Review Letters* (2004a). Submitted; preprint at `cond-mat/0406091`.

Zhukov AA, Goncharov AV, de Groot PAJ, Ghanem MA, El-Hallag IS, Bartlett PN, Boardman RP, Fangohr H, Novosad V and Karapetrov G. Oscillatory thickness dependence of the coercive field in 3d anti-dot arrays from self-assembly. *Journal of Applied Physics* (2004b). Submitted.

Zhukov AA, Goncharov AV, de Groot PAJ, P.N.Bartlett and M.A.Ghanem. Magnetic anti-dot arrays from self-assembly template methods. *Journal of Applied Physics*, **93**, 7322–7324 (2003).